The Dissertation Committee for John Michael Fonner Certifies that this is the approved version of the following dissertation:

MOLECULAR INVESTIGATION OF POLYPYRROLE AND SURFACE RECOGNITION BY AFFINITY PEPTIDES

Committee:

Christine E. Schmidt, Co-Supervisor

Pengyu Ren, Co-Supervisor

Ron Elber

George Georgiou

Krishnendu Roy

MOLECULAR INVESTIGATION OF POLYPYRROLE AND SURFACE RECOGNITION BY AFFINITY PEPTIDES

by

John Michael Fonner, B.S.

Dissertation

Presented to the Faculty of the Graduate School of

The University of Texas at Austin

in Partial Fulfillment

of the Requirements

for the Degree of

Doctor of Philosophy

The University of Texas at Austin

December 2011

Acknowledgements

I could not have done the research in this thesis without the support of many people. I am profoundly grateful for my wife. Thank you, Erin, for sharing my vision for this work and for consistently supporting me. Thank you for celebrating with me my successes and comforting me on the difficult days. To Christine and Pengyu, thank you for your mentorship and your investment in this research. I could not have wished for better advisors. I am also indebted to my parents, who always encouraged me to pursue my dreams. Thank you, Mom and Dad for the way you love each other and the way you poured into me. Finally, I give all credit to the One who created me and who lives in me. So often He has carried me on a personal level, and it is awe inspiring to see Him through scientific research as well.

Molecular Investigation of Polypyrrole and Surface Recognition by Affinity Peptides

John Michael Fonner, Ph.D.

The University of Texas at Austin, 2011

Supervisors: Christine Schmidt and Pengyu Ren

Successful tissue engineering strategies in the nervous system must be carefully crafted to interact favorably with the complex biochemical signals of the native environment. To date, all chronic implants incorporating electrical conductivity degrade in performance over time as the foreign body reaction and subsequent fibrous encapsulation isolate them from the host tissue. Our goal is to develop a peptide-based interfacial biomaterial that will non-covalently coat the surface of the conducting polymer polypyrrole, allowing the implant to interact with the nervous system through both electrical and chemical cues. Starting with a candidate peptide sequence discovered through phage display, we used computational simulations of the peptide on polypyrrole to describe the bound peptide structure, explore the mechanism of binding, and suggest new, better binding peptide sequences. After experimentally characterizing the polymer, we created a molecular mechanics model of polypyrrole using quantum mechanics calculations and compared its *in silico* properties to experimental observables such as density and chain packing. Using replica exchange molecular dynamics, we then modeled the behavior of affinity binding peptides on the surface of polypyrrole in explicit water and saline environments. Relative measurements of the contributions of each amino acid were made using distance measurements and computational alanine scanning.

Table of Contents

List of Tables

List of Figures

CHAPTER ONE

Introduction

1.1 INTRODUCTION

The complexity of the peripheral and central nervous systems has limited advances in therapies for injuries or disease of the nervous system, including neural probes and nerve guidance conduits. More specifically, the aggressive response of glial cells to the presence of implant materials causes the implant to be functionally isolated from the native tissue and encapsulated within a fibrous capsule. To be effective, long term implants in the nervous system must send tightly controlled physical, chemical, and electrical cues that inhibit glial cell activation and promote regeneration, which requires advanced, well-characterized, bioactive materials. In the peripheral nervous system, synthetic nerve guidance conduits have not performed as well as autologous nerve grafts in promoting functional recovery and cannot reliably prevent the formation of traumatic neuromas. Similarly, recording electrodes in the brain cannot currently achieve long-term sensitivity because of glial scar formation and the subsequent degeneration of neurons in the immediate vicinity of the probe. The long-term goal of this research is to develop electrically-conductive implant materials that promote nerve regeneration and reduce glial cell activation by incorporating a tightly bound layer of biomolecules on the surface. Specifically, this work describes efforts to characterize polypyrrole (PPy), a promising conductive polymer for biomedical applications, and to use computational simulations to assess affinity-binding peptides that can functionalize the surface of PPy. Surface functionalization for biomaterial implants allows the material to send specific and tailored chemical cues to surrounding tissue to direct cellular responses. This functionalization technique has strong potential for creating bioactive implants without

altering the bulk properties of the underlying material, but it also requires atomic level insight into the surface chemistry. This research has focused on making three contributions: 1) to better characterize PPy for biomedical applications, 2) to computationally model PPy, and 3) to simulate the binding interaction between PPy and affinity binding peptides. I have sought to leverage experimental and computational methods to characterize this surface chemistry for PPy, while at the same time develop transferrable computational methods for characterizing a broad set of biomaterials.

Computational Simulations in Context

It is difficult to predict the role that computation will play in material science and biomaterial design in the future. Historically, experimental observations have been the cornerstone of material design and biomedical research, and that is unlikely to change. Much remains unknown about the complex cellular pathways and the intricate extracellular environment that determine the host response to biomaterial implants and chemical signals, so no theory or simulation can replace the empirical evidence gathered from *in vitro* studies, animal models, and ultimately clinical trials. As our theoretical and analytical understanding has increased, however, mathematical modeling and "systems biology" approaches are used more and more to guide experimental methods. Considering examples such as virtual drug screening, we can see clues that some aspects of biomaterial design currently entrusted to empirical, experimental testing may be shifted toward predictive, computational testing.

Computational simulation as a scientific approach has a lot to prove before being widely adopted. Experimental evidence and the scientific method can be traced back several thousand years to ancient Egyptian and Greek cultures and has withstood the test

of time. Analytical, mathematical approaches, now fundamental components in the majority of scientific publications, owe their maturity to the brilliant minds of the last few centuries. In contrast, the capacity to conduct computational simulations has only existed for a few decades, and its progress has been throttled more by software development, hardware limitations, and computing resources than by the underlying algorithms and models. As these practical barriers to advancement are slowly overcome, I believe we will see simulation grow into an indispensible component of biomedical engineering.

1.2 Organization of the Dissertation

Chapter 1 is intended as a brief introduction to the purpose and context of this research, whereas Chapter 2 will go into more detail on the background and significance of polypyrrole as a biomaterial and the current state of molecular simulations.

Chapter 3 covers the experimental characterization and *in vitro* studies we conducted with polypyrrole. When first examining polypyrrole as a biomaterial, it was readily apparent that we needed to further explore the unique properties of the black and sometimes brittle film. What we found, just as several scientists before us had, is that seemingly insignificant details in the electrochemical synthesis process had drastic affects on the resulting material. In our case, we synthesized polypyrrole using three different dopants (chloride, tosylate, and polystyrene-sulfonate) on two substrates (gold and indium tin oxide) with a range of film thicknesses and measured the biologically important parameters of surface roughness, hydrophilicity, thickness, and the response of Schwann cells and PC12 cells. The results showed that different dopants and synthesis conditions served different implant applications, with trade-offs between conductivity, stability, and cell adhesion.

In Chapter 4, we discuss the molecular mechanics model that we created for polypyrrole. Starting from *ab initio* quantum mechanics calculations, we generated parameters for bond distances, angles, partial charges, and dihedral angles. Because of PPy's aromatic structure, "randomly" oxidized backbone, and strong electrostatic interactions with dopant ions, developing parameters required a well planned methodology, both to accurately describe the molecule and to integrate our parameters into existing software structures. Using the parameterized model, we used a thermal annealing approach and a potential scaling approach to form bulk polypyrrole matrices. With our own experimental density measurements and X-ray diffraction measurements, we compared the properties of our simulated PPy to the materials we produced at the lab bench. Though future improvements and additions to the model are possible, this work represents the most accurate and most rigorously tested model of PPy to date.

We utilize the model we developed and reported in Chapter 4 to study peptide interactions with PPy, as discussed in Chapter 5. The two impediments to performing this type of calculation are the accuracy of the underlying model and the ability to sample conformational space to obtain statistically useful binding affinity estimates. The models and techniques that currently exist are largely tailored to the needs of the drug design industry, which use small drug molecules that are much simpler than peptides in terms of their conformational flexibility and number of rotatable bonds. Additionally, the binding pocket is generally well defined in drug design applications, which contrasts sharply to the amorphous surface of a polymer surface. We found that the model parameters we used produced useful results, especially given the electrostatic approximations inherent to the model. The ability to directly visualize the trajectory of molecular dynamics simulations and to observe trends in the data provides excellent feedback and guidance for designing binding affinity peptides. For quantitative free energy of binding

calculations, however, this type of problem requires further growth in efficient sampling methods and computational power. Modeling peptide interactions with complex materials surfaces is a mostly unexplored application of molecular modeling. This work is an early investment in what we hope becomes a more comprehensive research topic. Improving biomaterial surfaces is crucial in the tissue engineering field, and computational modeling should help provide quantitative analysis, mechanistic insight, and even predictive capabilities to researchers in this area.

Chapter 6 contains a summary of the conclusions we have drawn from this study and a discussion of potential future directions. Computational chemistry is a rapidly developing field, and the limits on what is possible and what is practical are being constantly being rolled back. We are already able to relate experimental and computational studies to improve our insight into biomaterial/peptide interactions, but the heavy investment in developing computational models and navigating the fragmented and rapidly changing software tools will make it impractical for most labs to incorporate simulation into their benchtop work. Over the next ten years, we will very likely see a drastically increased presence of computational chemistry in material science and biomaterial surfaces, both out of the need to design implant surfaces at atomic level detail and because of the maturity and usability of the fledgling algorithms and tools being developed today.

CHAPTER TWO

Background and Significance

2.1 Introduction

In biomedical engineering, new innovations are frequently emerging from the interface between traditionally delineated specializations. The work presented in this thesis is no exception, as we utilize both experimental and computational methods to literally explore the interface between synthetic polymers and the biomolecules that exhibit binding specificity with them. To lay the groundwork for how the research we conducted contributes to the field, this chapter first discusses material biocompatibility and the foreign body reaction, especially in the nervous system. Next it discusses the clinical need for the type of bioactive material surfaces that we hope to develop. Although not directly used in this work, the phage display technique is explained briefly because of its central role in identifying affinity binding candidates. Afterwards we discuss polypyrrole, the biomaterial we have chosen to focus on, and the previous studies of the polymer. Finally, we give background on the computational models and techniques employed in this thesis, including quantum mechanics and molecular mechanics.

2.2 Chronic Implants and the Immune Response

The definition of what constitutes an "implant" or a "biomaterial" has become blurred as engineers develop everything from chronic synthetic sensors to degradable scaffolds loaded with stem cells and from locally injectable hydrogels to circulating drug delivery particles. The challenges associated with biocompatibility are drastically different depending on the lifetime of the implant, the composition and morphology of

the implant, the host tissue surrounding the implant, and the purpose of the implant. For non-degradable implant materials that remain in the body chronically, such as hip replacements, pacemakers, and cosmetic implants, the material is usually considered "biocompatible" if it is stably isolated within a fibrous capsule and does not chronically stimulate the immune system. The fibrous capsule distances the implant from the host tissue, usually by 50-200 μm (Ratner and Bryant 2004), which inhibits the detection of endogenous chemical and electrical signals by the implant. This type of isolation is usually acceptable, or even desirable, for implants whose function is to deliver structural support electrical signals without detecting endogenous signals. The capsule is a stable environment within which the implant may function. Unfortunately, settling for "bioinert" implant materials is usually not sufficient for electrical and chemical sensors and implants supporting regeneration. In these cases, isolation results in loss of function. Sensors tend to lack good, local blood perfusion and regenerative implants are prevented from effectively interacting with the tissue they wish to influence.

In the case of a device like a neural probe, there are many competing design constraints. The probe must be relatively small, electrically conductive, and in close contact with the surrounding tissue to detect nerve firing (Rousche and Normann 1998; Wadhwa, Lagenaur et al. 2006). A few researchers are exploring biomolecules like melanin as a natural conductive alternative to the traditional metals and synthetic polymers used to make the electrodes in the hopes that they can be both electrically conductive and, but the relatively low conductivity of such natural molecules limits their utility (Bettinger, Bruggeman et al. 2009). So if we are restricted to metals and conducting polymers to meet conductivity requirements, the question is, 'How can we create a bioactive surface without changing bulk conductivity?' For better tissue integration, an "interfacial biomaterial," as Meyers, *et al*. call it, is required to present

positive chemical cues to the host tissue without altering the favorable mechanical and electrical properties of the underlying material (Meyers, Khoo et al. 2009).

The idea of an interfacial biomaterial is to engineer a biomolecule, in our case a peptide, with one domain that selectively binds to the underlying implant material and another domain that interacts with the host tissue. Usually, these two domains may be designed fairly independently by connecting them with a linker molecule such as a polyglycine sequence or polyethylene glycol (PEG) chain that helps prevent the two domains from folding into each other. Barring the unwanted interaction between the two domains, the material-binding domain can tether various biomolecules with different functions to the implant surface, such as RGD peptides to encourage cell adhesion or nerve growth factor to promote regeneration. There is ample precedent for this approach with affinity binding peptides already developed for polystyrene (Meyers, Khoo et al. 2009), titanium (Meyers, Hamilton et al. 2007), and polyglycolic acid (Huang, Zauscher et al. 2010).

The foreign body reaction that ultimately encapsulates most implants, depicted in **Figure 2.1**, is initiated by the non-specific adsorption of a layer of host proteins (Anderson, Rodriguez et al. 2008). Thought the exact composition of proteins changes depending on the material properties and the time progression of the host response, monocytes and macrophages respond to this layer of un-oriented and possibly denatured proteins and mediate the encapsulation of the material (Kim, Scott et al. 2005). By engineering a layer of specifically adsorbed, oriented affinity peptides on a biomaterial prior to implantation, implants may be able to proactively diminish or prevent the foreign body reaction.

Peptide interfacial biomaterials have the potential to breathe new life into many bioinert biomaterials already approved by the Food and Drug Administration (FDA),

creating opportunities for them to be used in novel implant designs that require better tissue integration. Many investigators theorize that nonspecific protein adsorption to implant surfaces is complicit with, if not responsible for, triggering a hostile immune response, and thus controlling the protein layer at the surface of biomaterials may be critical in preventing fibrous encapsulation. The main tool that currently enables the discovery of these binding peptide sequences is the phage display technique, which will be discussed in the next section. Phage display is a reliable, brute force method for finding candidate binding peptide sequences, but it gives no information on why a specific sequence successfully binds (Lowman, Bass et al. 1991; Schmitz, Versmold et al. 2000). In the drug design industry, after a drug candidate is identified, there is a well-defined process for refining the drug to improve the binding affinity. The analogous process for binding peptides is generally prohibitively expensive to accomplish experimentally due to the high cost of synthesizing peptides. Computational simulation has the opportunity to better explain the binding mechanism for binding peptides and to suggest worthwhile variants that may improve the binding strength.

2.3 Affinity Binding Peptides

Many of the binding peptides reported in the literature were discovered through bacteriophage display screening (Kehoe and Kay 2005). A bacteriophage, often shortened to phage, is a class of viruses that infect bacteria. They can be modified to express defined sequences of amino acids in their coat proteins by inserting the matching genetic codons into known locations of the virus' genome. Large combinatorial libraries have been developed containing phage that express billions of different peptide sequences and are available for purchase, making the phage display technique accessible to a large number of groups. It is possible to pan these libraries over a biomaterial, rinse

the unbound phage, and capture the bound phage (Kehoe and Kay 2005; Meyers, Khoo et al. 2009; Huang, Zauscher et al. 2010). The phage that adsorbed to the biomaterial can be eluted and amplified, and then the process may be repeated. The different peptide sequences will compete to bind with the material, and after several cycles, only the best binders will remain. By sequencing the modified genes of the best binders, the associated affinity binding peptide sequences may be learned.

For very short peptide sequences, almost every possible sequence may be represented in the phage library. Seven amino acid sequences, for example, have 20^7 = 1.28 billion possibilities given the twenty traditional amino acids. In this case, the phage display technique is fairly deterministic, but for longer peptides such as twelve amino acid sequences, there are 20^{12} = 4.10 quadrillion possibilities. A library of several billion 12 amino acid sequences only represents one one-millionth of the possible combinations. Thus, although phage display consistently yields good binding candidates even for longer peptides, it almost certainly does not yield the best possible binder. In this case, we need a better way to intelligently explore sequences not in the library to refine peptide.

Central to the challenge of refining binding peptide candidates is the fact that phage display gives very little information beyond the sequence of the peptides. The bound structure is not known, the binding affinity data is not quantitative, and the contribution of different amino acids is difficult to determine. Gaining this additional information experimentally is possible, but very time consuming and expensive. Synthetically creating a specific peptide sequence is costly, especially when high purity is required. The cost is not prohibitive when only a few sequences are needed, but experimentally exploring new peptide sequences is not possible for most researchers.

Measuring the binding affinity of a single peptide sequence has become somewhat standard by using surface plasma resonance (SPR) as long as the material is

amenable to the requirements of that technique, namely solubility or the ability to form thin films of the material. For materials that are not compatible with SPR, such as polypyrrole, researchers may use atomic force microscopy (AFM) and enzyme-linked immunosorbent assays (ELISA) to derive the binding constant, though the task can be very time consuming and contain significant error. SPR and AFM make sense for measuring the binding affinity of one peptide sequence, but comparative studies to explore peptide variants and determine more mechanistic information about the peptide binding add a level of complexity that make those techniques impractical, both from the perspective of the time investment and the financial cost. It is in comparative analysis that computational methods have the greatest potential to advance the field of engineering binding peptides.

2.4 Clinical Relevance

Peripheral nerve injuries resulting in nerve gaps greater than a few centimeters do not heal naturally, and current clinical techniques have had minimal success in restoring function to damaged nerves (Mackinnon and Dellon 1988). Two main challenges limit functional recovery: 1) the slow rate of nerve regeneration (or neurite extension) relative to the formation of scar tissue, and 2) failure of the extending neurite to find its target.

A few years ago, decellularized, allogenic nerve graft technology developed by the Schmidt lab (Hudson, Liu et al. 2004; Hudson, Zawko et al. 2004) was licensed by Axogen, approved for clinical use, and has provided another tool for surgeons (Karabekmez, Duymaz et al. 2009). The gold standard for repairing nerve gaps is to harvest some nerve tissue from a different site in the patient and graft the fresh, autologous nerve into the site of injury (Mackinnon and Dellon 1988). Decellularized

allogenic nerve grafts have very attractive advantages in that they do not evoke a negative immune response, provide an excellent scaffold for regenerating nerves with all the native extracellular matrix components, and do not require a second surgery to harvest nerve tissue from the patient. The disadvantages to nerve grafts are that the supply is limited by the donor cycle, which is a common problem for all organ donations, they do not incorporate electrical stimulation, and incorporating additional growth factors back into the graft has proven very difficult. Clinically, decellularized grafts perform almost as well as fresh, autologous nerve grafts in promoting functional recovery, so they are a significant contribution to the field (Karabekmez, Duymaz et al. 2009). While they are a very "natural" implant that mimics the native tissue, nerve regeneration is unfortunately very limited in the natural environment, and research has shown that implants able to incorporate chemical and electrical cues in addition to proper structural cues may be much more effective in promoting regeneration (Al-Majed, Neumann et al. 2000; Lykissas, Batistatou et al. 2007).

Materials integrating electrical stimulation have performed well in *in vitro* studies. Previous, published studies both within our lab and in other labs have shown that neuronal cells are responsive to surface chemical cues and externally applied electrical stimulation (Schmidt, Shastri et al. 1997; Garner, Georgevich et al. 1999). Polypyrrole (PPy), when electrically stimulated, results in nearly a two-fold enhancement of neurite outgrowth from PC-12 cells (i.e., a neuron-like cell line) compared to unstimulated controls. *In vivo* studies have also demonstrated that PPy is not cytotoxic and that this material, when formed into conduits, can support the regeneration of damaged peripheral nerves in rats (Schmidt, Shastri et al. 1997). Researchers have observed increased neurite extension, increased neurite branching, and alignment of the direction of neurite extension depending on the type, intensity, and timing of the electrical stimulation as well

as the neuronal cell type. Research is ongoing of how cellular mechanisms are affected by electrical stimulation and what stimulation parameters are ideal. Moving toward *in vivo* applications, the challenge in creating synthetic nerve guidance channels will be mitigating the aggressive immune response toward synthetic materials, as discussed in Section 2.2. A significant amount of work remains on better understanding how electrical stimulation should be used, what types of growth factors and gradients promote faster Schwann cell migration and neurite extension, and how the implant should be shaped and structured to physically support new nerve bundles. One of the key technologies required, however, will be how to immobilize biomolecules to the surface of the scaffold to promote regeneration. This research into binding affinity peptides seeks to improve our ability to functionalize polypyrrole so that we can more readily leverage our fundamental understanding of chemical gradients and electrical stimulation to develop better nerve guidance channels.

Beyond nerve guidance channels, better material design and surface functionalization is critical for neural probes. In the central nervous system, glial scars surround traditional implants, causing neural probes to lose sensitivity and become ineffective over time (Polikov, Tresco et al. 2005; Seymour and Kipke 2007). Electrodes intended to externally stimulate can maintain functionality over time by increasing the strength of the stimulation to pass through the fibrous capsule, but probes intended to detect endogenous signals lose their sensitivity within a few months of implantation. Research performed by the Bellamkonda lab shows that neurons near an implanted electrode tend to become inactive and withdraw from the electrode even after the wound healing response has stabilized (McConnell, Rees et al. 2009). The authors conclude that, even without stimulation, the mere presence of an electrode in the brain that is identified by the body as foreign triggers the formation of a functional “dead zone”

around the implant that attenuate the detected endogenous signals long term. Bioactive materials that can interact with nervous tissue without inducing scarring will open the door to therapeutic and diagnostic tools that are currently impossible.

2.5 CONDUCTING POLYMERS

Conducting polymers are a class of semiconducting materials with a broad set of applications in electronics, sensors, and coatings. There are over a dozen types of conducting polymers, but the most widely used and most intensely studied polymers are polyanalines (PANI), polyacetylenes (PAC), polythiophenes, polyethylenedioxythiophenes (PEDOT), and polypyrroles (PPy). Each type of polymer has different properties such as solubility, chain length, stability, and toxicity.

The high electrical conductivity of conducting polymers hinges on the incorporation of dopant ions into the material. For PPy, the backbone of the polymer may be oxidized during polymerization, giving it a positive charge. Anions are incorporated to neutralize the positive charge of PPy and to decrease the band gap. Commonly used dopants include chloride ions, para-toluene sulfonate, and poly(styrene sulfonate). PPy has also been doped with a wide variety of other materials, including small anions (Vork, Schuermans et al. 1990), polymeric anions (Prezyna, Qiu et al. 1991), buffer salts (Genies, Marchesiello et al. 1992), and biologically active anions such as ATP (Boyle, Genies et al. 1990), collagen (Li and Khor 1995), hyaluronic acid (Collier, Camp et al. 2000), heparin (Garner, Georgevich et al. 1999), and enzymes (Shin and Kim 1996). Although large dopant ions can be used to modify the surface characteristics of PPy, this approach has several drawbacks, including being limited to negatively charged molecules and difficulty with incorporation of large molecules

(Collier, Camp et al. 2000). To obtain good conductivity, it is best to use more traditional dopant ions in the bulk of the polymer and only modify the surface. The chemical structure of doped PPy is shown in **Figure 2.2**, and more in-depth background on PPy is contained in Chapter 3.

Affinity binding peptides for PPy provide an excellent vehicle for modifying the surface chemistry without decreasing bulk conductivity. Toward this end, the Schmidt lab previously utilized the phage display technique to select the T59 peptide sequence, which selectively binds to PPy (Sanghvi, Miller et al. 2005). Unpublished work within the lab has shown that the electrical conductivity of PPy does not decrease when the surface is modified by T59 and that the presence of the surface peptide does not reduce biocompatibility in rat models. The T59 peptide is discussed in more detail in Chapter 5.

2.6 COMPUTATIONAL CHEMISTRY

The bulk of the mathematics and physics used to describe atomic interactions and movement have been well defined and understood for almost a century. Our ability to apply these equations to simulate larger and more complex systems, however, is a recent evolution. The rapid expansion of computer power over the last couple of decades has allowed us to suddenly model biomolecules with accuracy that in some cases matches experimental results. As the software and tools for examining biological systems mature, both in the techniques available and in the ease of use, life scientists will find themselves with new approaches for solving difficult problems.

Coinciding with the increase in computer power, the trending research foci of biomedical engineering have evolved from bulk implants and instrumentation to micro-scale devices and sensors to nano-scale imaging and molecular design. Biological

processes natively occur at a molecular level, and modern biomedical laboratories must operate at that level. Traditionally, we leverage equipment and protocols to scale up molecular interactions into macroscopic observables. Techniques such as nuclear magnetic resonance (NMR) spectroscopy, fluorescence microscopy, X-ray photoelectron spectroscopy (XPS), and countless others are all designed to help us understand and control experiments at a molecular level, which is a goal shared by computational chemistry.

In contrast to experimental approaches, which infer atomic behavior from macroscopic observables, computational chemistry directly observes atomic behavior and must infer macroscopic properties. This "bottom up" approach to chemistry lends itself to simulating interactions that happen at very short time scales and very small length scales, which are sometimes inaccessible to experiments; however, comparing femtosecond simulation steps with hour-long experiments is not trivial and requires the careful application of statistical mechanics. Simulations by themselves can only theorize about what occurs on the lab bench, and there is no guarantee that what we calculate *in silico* translates to experimental observations. Just as any scientific hypothesis requires validation, so too the relevance of computational biology relies on comparison with experiments for support. In this work, for example, we compare atomic spacing from X-ray diffractograms to radial distribution functions calculated from simulations. Computational chemistry, therefore, should be seen by biomedical researchers as another valuable tool in solving real world problems and not as an approach to be used in isolation. Conversely, computation is one of few investigation techniques that is becoming more cost efficient, more accurate, faster, and easier to use over time, so many competitive research labs will wisely find ways to integrate it into their experimental work.

Computational models may be classified into several categories based on their accuracy and the size of systems they can simulate. These models are represented graphically in **Figure 2.3**. Quantum mechanics (QM) based models are in general the most accurate, with small errors that rival bench top measurements. Electrons are modeled explicitly, and interactions and movement are calculated using Schrödinger's equations. Bonds in this model are the result of overlapping orbitals, and chemical reactions are possible. There are multiple approaches to represent electrons in QM; density functional theory (DFT) is currently the most widely used. Ground state electron densities are represented by a spatial function, which is usually a set of Gaussian functions. The set of functions used to describe the electrons and atom nuclei is called the basis set. To help correct for the averaged electron interactions in DFT, electron correlation methods such as Møller-Plesset perturbation are employed when possible to improve accuracy. As computer power grows, basis sets of higher complexity and higher accuracy are becoming more common, constantly pushing the limits in system size and accuracy. Many good resources exploring QM methods in detail are available on the subject (Hiberty and Shaik 2007; Zhao and Truhlar 2008; Lewars 2011). Even for low basis sets, however, Schrödinger's equations are computationally expensive to solve when compared to molecular mechanics, and generally scale poorly with system size, so researchers are limited in the systems they are able to study. Most biomolecules, which are huge by QM standards, are out of reach for these models unless massive approximations are made that generally undermine the purpose of using such a high accuracy model in the first place.

To model larger systems, molecular mechanics (MM) models are generally employed. MM describes the structure of molecules in essentially a classical, ball and spring representation that requires empirical parameters for each atom type and often

each molecule in the system (Jorgensen, Maxwell et al. 1996). These empirical parameters are obtained from QM calculations and sometimes tuned to match experimental observables (Mahoney and Jorgensen 2000). Bond distances, bond angles, and dihedral angles are defined by equilibrium bond distances and coefficients or sets of coefficients that describe the energy penalty for moving away from equilibrium. Bond distances and bond angles are generally harmonic equations, whereas dihedral angles, which are periodic in nature, are represented by either Fourier series or the analogous Ryckaert-Bellemans function. There are multiple ways to represent electrostatic and van der Waals forces, which are often called non-bonded interactions. For fixed-charge models, the most widely used, Coulomb's law defines electrostatic interactions and the Lennard Jones equation represents the van der Waals and London dispersion forces between atoms. More details on the specific models and parameters used in this work are in Chapter 4 and 5. The key advantages of using MM models are that they are very well established, both in terms of parameters and software tools, and that they scale well for larger systems. At the time of writing, system sizes of half a million atoms and simulation lengths up to a microsecond are possible.

Although not utilized in this research, it is also important to note that models that use polarizable electrostatics and that represent atoms with multipoles instead of point charges are becoming more accessible and well developed (Ponder, Wu et al. 2010). Electrostatic interactions are generally the largest energy contributor and the largest source of error in MM calculations (Ren and Ponder 2002), and increasing the fidelity of electrostatic representation can have a large affect on the accuracy of the model. Multipoles and polarizability are especially important for simulating metal ions and aromatic molecules, an area where fixed-charge representations have larger errors.

For longer simulations of very large systems, course grain models may be used (Tozzini 2005). They add another layer of abstraction as the smallest unit represented in the model is a functional group of several atoms. The mathematical representations of these groups are not as standardized as MM models, but it provides a way for researchers to explore mesoscale properties, such as glass transition temperatures and polymer organization. For binding interactions, course grain models lack the detail to provide reliable data, and as such, they are not used in this work. Course grained models are mentioned for completeness, but in future chapters the discussion will center around QM and MM models.

2.7 FIGURES

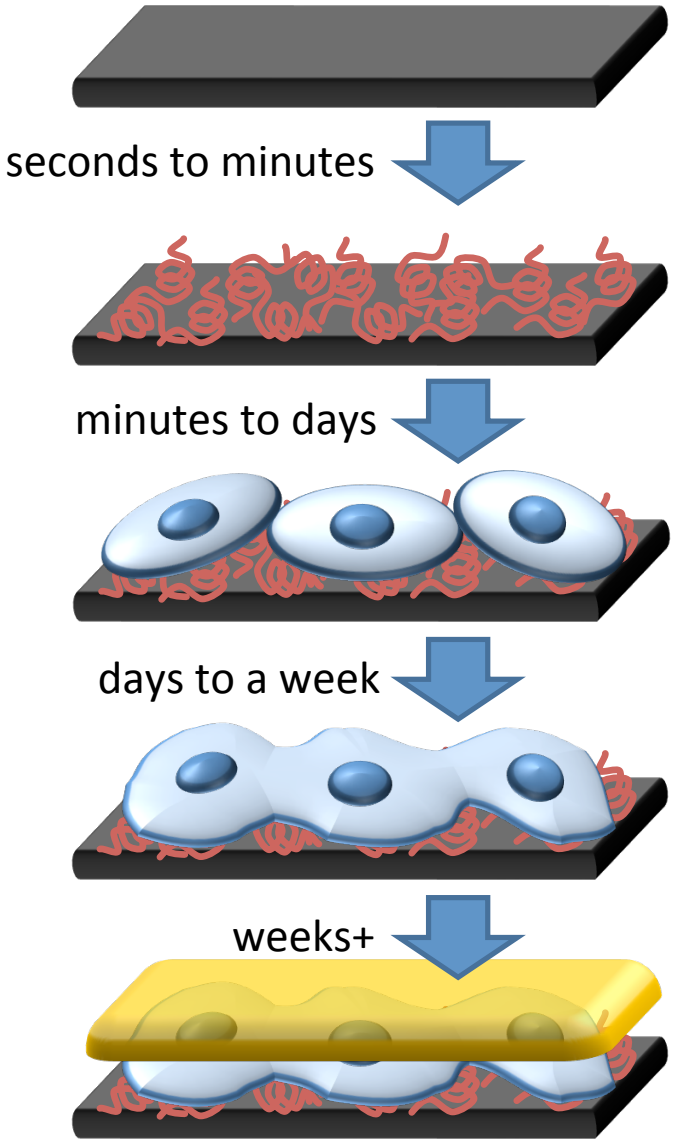

Figure 2.1 – Foreign body reaction.

Adapted from Ratner and Bryant, 2004. For any synthetic material in the body, nonspecific protein adsorption quickly coats the surface of the material. This denatured protein layer signals for monocytes to adhere, and they begin differentiating into macrophages and fusing into giant cells over several days. Since these cells cannot phagocytose or eliminate the implant, a fibrous capsule forms over several weeks to wall off the foreign material from the rest of the body.

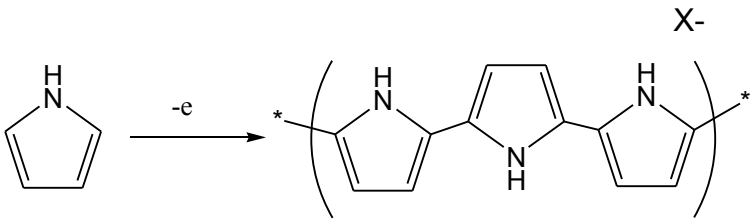

Figure 2.2. Chemical Structure of Polypyrrole.

Doped PPy contains oxidized, positively charged sites along the backbone that affect the bond order along the backbone. These oxidized PPy rings interact with dopant ions to form polarons and bipolarons and lend to the electrical conductivity of the material. More detail on the bond order changes is included in the discussion in Chapter 4. Specifics on charge carriers in PPy and other conducting polymers is widely discussed in the literature, and a good example is a paper by G. Zotti published in 1998 (Zotti 1998).

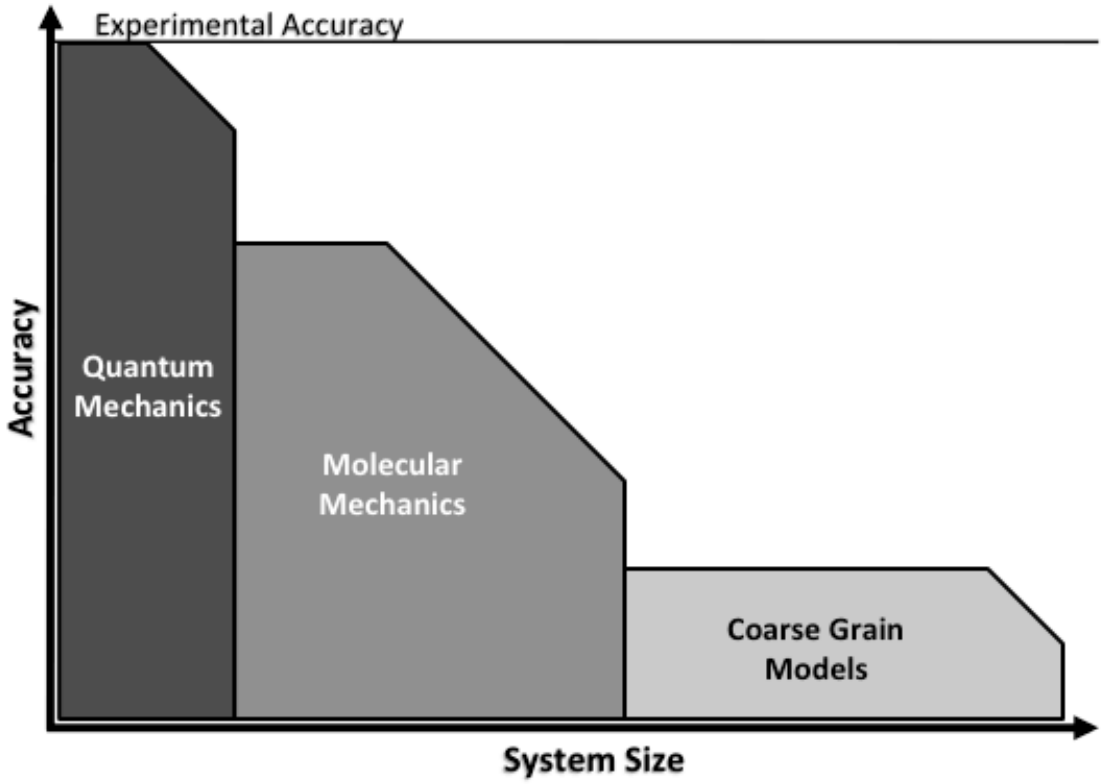

Figure 2.3. Comparison of Common Computational Chemistry Models.

Computational chemists have a range of models that can simulate a wide range of system sizes and time periods. Quantum Mechanics provides very accurate representations of molecules and explicitly takes into account the interactions of electrons, but is most commonly limited to systems of a few hundred atoms at most. For larger systems, an empirically parameterized model must be used. Molecular mechanics neglects electron interactions and instead represents averaged atomic interactions through a ball and spring model.

2.8 REFERENCES

Al-Majed, A. A., C. M. Neumann, et al. (2000). "Brief electrical stimulation promotes the speed and accuracy of motor axonal regeneration." The Journal of Neuroscience **20**(7): 2602.

Anderson, J. M., A. Rodriguez, et al. (2008). Foreign body reaction to biomaterials, Elsevier.

Bettinger, C. J., J. P. Bruggeman, et al. (2009). "Biocompatibility of biodegradable semiconducting melanin films for nerve tissue engineering." Biomaterials **30**(17): 3050-3057.

Boyle, A., E. Genies, et al. (1990). "Electrochemical-Behavior of Polypyrrole Films Doped with Atp Anions." Journal of Electroanalytical Chemistry **279**(1-2): 179-186.

Collier, J. H., J. P. Camp, et al. (2000). "Synthesis and characterization of polypyrrole-hyaluronic acid composite biomaterials for tissue engineering applications." Journal of biomedical materials research **50**(4): 574-584.

Garner, B., A. Georgevich, et al. (1999). "Polypyrrole-heparin composites as stimulus-responsive substrates for endothelial cell growth." Journal of biomedical materials research **44**(2): 121-129.

Genies, E. M., M. Marchesiello, et al. (1992). "Preparation and Properties of Polypyrrole Made in the Presence of Biological Buffers." Electrochimica Acta **37**(6): 1015-1020.

Hiberty, P. C. and S. Shaik (2007). "A survey of recent developments in ab initio valence bond theory." Journal of Computational Chemistry **28**(1): 137-151.

Huang, X., S. Zauscher, et al. (2010). "Peptide interfacial biomaterials improve endothelial cell adhesion and spreading on synthetic polyglycolic acid materials." Annals of biomedical engineering **38**(6): 1965-1976.

Hudson, T. W., S. Y. Liu, et al. (2004). "Engineering an improved acellular nerve graft via optimized chemical processing." Tissue Engineering **10**(9-10): 1346-1358.

Hudson, T. W., S. Zawko, et al. (2004). "Optimized acellular nerve graft is immunologically tolerated and supports regeneration." Tissue Engineering **10**(11-12): 1641-1651.

Jorgensen, W. L., D. S. Maxwell, et al. (1996). "Development and testing of the OPLS all-atom force field on conformational energetics and properties of organic liquids." Journal of the American Chemical Society **118**(45): 11225-11236.

Karabekmez, F. E., A. Duymaz, et al. (2009). "Early clinical outcomes with the use of decellularized nerve allograft for repair of sensory defects within the hand." Hand **4**(3): 245-249.

Kehoe, J. W. and B. K. Kay (2005). "Filamentous Phage Display in the New Millennium." Chemical Reviews **105**(11): 4056-4072.

Kim, J.-K., E. A. Scott, et al. (2005). "Proteomic analysis of protein adsorption: Serum amyloid P adsorbs to materials and promotes leukocyte adhesion." Journal of Biomedical Materials Research Part A **75A**(1): 199-209.

Lewars, E. G. (2011). Computational chemistry: introduction to the theory and applications of molecular and quantum mechanics, Springer Verlag.

Li, H. C. and E. Khor (1995). "A Collagen-Polypyrrole Hybrid - Influence of 3-Butanesulfonate Substitution." Macromolecular Chemistry and Physics **196**(6): 1801-1812.

Lowman, H. B., S. H. Bass, et al. (1991). "Selecting high-affinity binding proteins by monovalent phage display." Biochemistry **30**(45): 10832-10838.

Lykissas, M. G., A. K. Batistatou, et al. (2007). "The role of neurotrophins in axonal growth, guidance, and regeneration." Current neurovascular research **4**(2): 143-151.

Mackinnon, S. E. and A. L. Dellon (1988). "Surgery of the peripheral nerve." New York.

Mahoney, M. W. and W. L. Jorgensen (2000). "A Five-Site Model for Liquid Water and the Reproduction of the Density Anomaly by Rigid, Nonpolarizable Potential Functions." Journal of Chemical Physics **112**(20): 8910-8922.

McConnell, G. C., H. D. Rees, et al. (2009). "Implanted neural electrodes cause chronic, local inflammation that is correlated with local neurodegeneration." Journal of Neural Engineering **6**: 056003.

Meyers, S. R., P. T. Hamilton, et al. (2007). "Endothelialization of titanium surfaces." Advan. Mater **19**: 2492-2498.

Meyers, S. R., X. Khoo, et al. (2009). "The development of peptide-based interfacial biomaterials for generating biological functionality on the surface of bioinert materials." Biomaterials **30**(3): 277-286.

Polikov, V. S., P. A. Tresco, et al. (2005). "Response of brain tissue to chronically implanted neural electrodes." Journal of Neuroscience Methods **148**(1): 1-18.

Ponder, J. W., C. Wu, et al. (2010). "Current Status of the AMOEBA Polarizable Force Field." The Journal of Physical Chemistry B **114**(8): 2549-2564.

Prezyna, L. A., Y. J. Qiu, et al. (1991). "Interaction of Cationic Polypeptides with Electroactive Polypyrrole Poly(Styrenesulfonate) and Poly(N-Methylpyrrole) Poly(Styrenesulfonate) Films." Macromolecules **24**(19): 5283-5287.

Ratner, B. D. and S. J. Bryant (2004). "Biomaterials: where we have been and where we are going." Annu. Rev. Biomed. Eng. **6**: 41-75.

Ren, P. and J. W. Ponder (2002). "Consistent treatment of inter and intramolecular polarization in molecular mechanics calculations." Journal of Computational Chemistry **23**(16): 1497-1506.

Rousche, P. J. and R. A. Normann (1998). "Chronic recording capability of the Utah Intracortical Electrode Array in cat sensory cortex." Journal of Neuroscience Methods **82**(1): 1-15.

Sanghvi, A. B., K. P. H. Miller, et al. (2005). "Biomaterials functionalization using a novel peptide that selectively binds to a conducting polymer." Nature Materials **4**(6): 496-502.

Schmidt, C. E., V. R. Shastri, et al. (1997). "Stimulation of neurite outgrowth using an electrically conducting polymer." Proceedings of the National Academy of Sciences of the United States of America **94**(17): 8948-8953.

Schmitz, U., A. Versmold, et al. (2000). "Phage Display: A Molecular Tool for the Generation of Antibodies-- A Review." Placenta **21**(Supplement 1): S106-S112.

Seymour, J. P. and D. R. Kipke (2007). "Neural probe design for reduced tissue encapsulation in CNS." Biomaterials **28**(25): 3594-3607.

Shin, M. C. and H. S. Kim (1996). "Electrochemical characterization of polypyrrole glucose oxidase biosensor .1. Influence of enzyme concentration on the growth and properties of the film." Biosensors & Bioelectronics **11**(1-2): 161-169.

Tozzini, V. (2005). "Coarse-grained models for proteins." Current Opinion in Structural Biology **15**(2): 144-150.

Vork, F. T. A., B. C. A. M. Schuermans, et al. (1990). "Influence of Inserted Anions on the Properties of Polypyrrole." Electrochimica Acta **35**(2): 567-575.

Wadhwa, R., C. F. Lagenaur, et al. (2006). "Electrochemically controlled release of dexamethasone from conducting polymer polypyrrole coated electrode." Journal of Controlled Release **110**(3): 531-541.

Zhao, Y. and D. G. Truhlar (2008). "Density functionals with broad applicability in chemistry." Accounts of Chemical Research **41**(2): 157-167.

Zotti, G. (1998). "Doping-level dependence of conductivity in polypyrroles and polythiophenes." Synthetic Metals **97**(3): 267-272.

CHAPTER THREE

Experimental Characterization of Polypyrrole

3.1 INTRODUCTION

Biomaterials must be carefully chosen and manufactured to interact favorably with biological systems. This is especially true within the nervous system, where neurons have been shown to respond to physical (Clark, Connolly et al. 1990; Miller, Jeftinija et al. 2002; Dowell-Mesfin, Abdul-Karim et al. 2004), chemical (Bray and Hollenbeck 1988; Bentley and O'Connor 1994; Pini 1994), and electrical (Schmidt, Shastri et al. 1997; Ming, Henley et al. 2001) cues, in addition to cellular signals. Polypyrrole (PPy), a conducting polymer that is easily synthesized both chemically and electrochemically, has been investigated for use in neural probes (Cui, Wiler et al. 2003) and as scaffolds to promote axonal elongation for use in nerve guidance channels (Schmidt, Shastri et al. 1997; Kotwal and Schmidt 2001). Although conducting polymers and PPy in particular are well characterized (Kaynak 1997; Suarez and Compton 1999; Yuan, Adeloju et al. 1999; Sadki, Schottland et al. 2000; Guimard, Gomez et al. 2007; Skotheim and Reynolds 2007), there has been little effort to link biologically relevant polymer properties such as roughness, surface energy, and stability to cellular outcomes. The work in this chapter seeks to begin filling this gap in research by investigating three commonly used negatively charged dopants: chloride (Cl), tosylate (ToS), and polystyrene sulfonate (PSS). Within the larger context of modifying the surface of polypyrrole, this work provides the experimental context around which we developed our model.

To assess biocompatibility, we tested the viability of two cell cultures, rat PC-12 and Schwann cells, on PPy films made with different dopants. PC-12 cells were chosen because of their use in previous studies and their neuron-like behavior, since many

proposed uses of PPy are within the nervous system (Schmidt, Shastri et al. 1997; Cui, Wiler et al. 2003). Schwann cells were used because their migration into a wound site precedes axon repair, making them an important consideration when designing implants for the peripheral nervous system (Frostick, Yin et al. 1998; Al-Majed, Neumann et al. 2000). Because the phenotypic responses of PC-12 cells and Schwann cells are sensitive to adhesion and surface topography, these two cell types are also good indicators of the effects of subtle differences in the surface energy and roughness of the underlying substrate.

Despite the volume of theoretical studies and characterizations performed for PPy, few studies provide comparative information of biomedically-relevant parameters. By electrochemically synthesizing films with controlled characteristics and examining the resulting cellular response, our goal was to create better, more refined biomaterials for specific applications. We will also provide practical guidelines and observations from our experience in working with PPy films.

History of Polypyrrole

PPy is an inherently conducting polymer with interesting electrical properties first discovered and reported in the early 1960s (Bolto, McNeill et al. 1963). By incorporating anions into the polymer during synthesis, also called doping, the resistivity of PPy is greatly reduced, giving it conductivity within the semiconductor range (Diaz 1981; Diaz and Kanazawa 1983; Diaz and Hall 1983). In general, PPy is an opaque, brittle, amorphous material, although its specific properties are influenced by the dopant (Wynne and Street 1985) and polymerization technique used, as well as a host of other variables. Investigators have explored various dopants, including common ions such as iodine,

chloride (Cl), polystyrene sulfonate (PSS), tosylate (ToS), and perchlorate, as well as more complex biomolecules such as biotin (George, LaVan et al. 2006), chondroitin sulphate (Serra Moreno, Panero et al. 2008), and nerve growth factor (NGF) (Hodgson, John et al. 1996) with various degrees of success. In this study we chose Cl, ToS, and PSS as dopants, because they are water soluble, biocompatible, commonly used for biomedical applications, and provide a range of molecular weights (Schmidt, Shastri et al. 1997; Wang, Gu et al. 2004; George, Lyckman et al. 2005), Guimard, et al. 2007). The large variety of methods to synthesize and modify the characteristics of PPy make this material attractive for a wide range of applications, but this flexibility also makes it difficult to select the best synthesis parameters for a specific application. Because of the large number of variables associated with polypyrrole synthesis, we chose to measure severable biologically relevant parameters after using different synthesis conditions.

Polypyrrole Synthesis Parameters

Besides chemical synthesis methods, electrochemical polymerization may be performed by using constant current (galvanostat), constant voltage (potentiostat), or by changing voltage (cyclic voltammetry). Electrochemical synthesis results in a film of doped PPy being deposited on the working electrode (e.g., indium tin oxide (ITO) coated glass slide or gold-coated substrate) of a three electrode setup. The deposition process nucleates around initial points and quickly spreads over the surface of the electrode; the electrode material has a large effect on this adhesion and spreading (Sadki, Schottland et al. 2000). Previous studies have reported that PPy oligomers adsorb to the electrode once their length makes them insoluble, with subsequent oligomers preferentially adsorbing to the PPy nucleation points (Vernitskaya and Efimov 1997). The doping level, measured as

a percentage of anions to monomer units, varies depending on the concentration of anions in solution, but typical values range between 25-30% (Diaz and Kanazawa 1983; Kang 1997). The details of electrochemical synthesis are covered in other papers (Vernitskaya and Efimov 1997; Sadki, Schottland et al. 2000).

Previous studies have also shown that solvent, pH, substrate, and temperature during synthesis affect the final properties of PPy (Kaynak 1997; Sadki, Schottland et al. 2000; Carquigny, Segut et al. 2008). Because pyrrole monomers are soluble in a wide range of solvents, PPy may be synthesized in both aqueous and organic solvents, but comparisons across solvents are difficult because of changes in dopant solubility and pH. Since temperature is usually room temperature and pH is dictated by the solvent, this study focuses on the effects of dopant and substrate – the two synthesis parameters that are most easily manipulated and that have the greatest variability in the literature. Film thickness and roughness were assessed for three dopants, two substrates, and multiple polymerization times, and biocompatibility, conductivity, contact angle, and stability of the created PPy films were compared for the different dopants. All polymerizations were performed at room temperature using constant voltage in aqueous solvent (distilled, de-ionized water) with neutral pH and 0.1 M concentrations of pyrrole and dopant – conditions that may be easily repeated in other laboratories.

Motivation for Polypyrrole as a Biomaterial

The material properties measured in this study were chosen for their relevance to biomedical implants. The roughness of implant surfaces (measured at the nanometer to micrometer scale) affects cell adhesion by changing the surface area perceived by the cell. Contact angle is a relative measure of surface energy, which also strongly affects

cell adhesion (Hallab, Bundy et al. 2001). Conductivity and the stability of dopant/PPy interactions are important for the previously-mentioned applications of neural probes and nerve guidance channels, as well as any device using electricity for therapeutic or diagnostic purposes. Characterizing these parameters is a contribution to the field within itself, and material properties such as contact angle measurements may be compared to computational simulations as well. Conductivity would require a very involved quantum mechanics study, which is out of the scope of this thesis, and the micron scale roughness, though very relevant when interpreting cellular response, is too large to capture in atomistic simulations.

3.2 Materials and Methods

Materials

Pyrrole, reagent grade, 98%, and the dopants, sodium p-toluene-sulfonate, 95% grade, poly(sodium4-styrene-sulfonate) (PSS), 70,000 Daltons average molecular weight, and sodium chloride, ACS reagent, were purchased from Sigma-Aldrich, St. Louis, MO. Platinum gauze for electrochemical deposition was purchased from Aldrich, Milwaukee, WI. Indium tin oxide (ITO)-coated unpolished float glass slides (25 × 75 × 0.5 mm, 30-60 Ω) were purchased from Delta Technologies, Stillwater, MN, and frosted pre-cleaned microscope slides were purchased from Stuart Scientific, Greensburg, Pennsylvania. Isopropanol (1-Propanol), 99%, was purchased from Sigma-Aldrich. Fisher brand plates and Pasteur pipettes were used throughout the experiments. All other chemicals used were 98% reagent grade or better.

Polypyrrole Synthesis

To create gold-coated slides, an Edwards Auto 500 thermal evaporator located in the Nano Science and Technology (NST) user facility was used to deposit chromium and gold onto untreated, frosted, pre-cleaned microscope slides. The slides were further cleaned by sonication in distilled, deionized water for 10 minutes, followed by sonication in isopropanol, and were stored in isopropanol until use. Between 4-8 nm of chromium was first thermally deposited on the surface of the microscope slide, followed by thermal deposition of 40 nm of gold.

Next, pyrrole monomer was purified by passing it through an aluminum oxide column. Three dopant types (Cl, ToS, PSS) were used to synthesize three types of polypyrrole films on two different substrates (ITO and gold). For the synthesis, an aqueous solution of 0.1 M pyrrole and 0.1 M dopant anions was used in combination with a three electrode electrochemical setup. Since PSS is a poly-anionic molecule capable of doping PPy in many locations, the anion concentration (0.1 M) of PSS was used for comparison with the other two mono-anionic species (Cl, ToS) rather than the molecular concentration (~283 μM).

For the three-electrode setup, a gold-coated or ITO-coated slide with an accessible surface are of 7.5 cm^2 (25 mm slide width by 30 mm) was used as the working electrode. A platinum mesh (20 mm by 30 mm) served as the counter electrode, and a saturated calomel electrode was used as the reference electrode. An oxidizing potential of 720 mV supplied by a potentiostat (CH Instruments, electrochemical analyzer) was used for all PPy polymerization reactions. The passage of charge was recorded to test its correlation with thickness, as initially proposed by Diaz and Hall. (1983).

The macroscopic surface area of each film was measured using a ruler and the films were then rinsed extensively with deionized water for 10 minutes. Once properly rinsed, the films were kept under vacuum overnight to dry.

Physical Property Characterization of PPy Films

Film thickness and roughness measurements were performed using a Dektak 6M Stylus Profiler (Veeco) profilometer in the NST building clean room. Two parallel scratches were made on the PPy film approximately 2 mm apart, and the average step height was calculated between the scratches on the film. The roughness was calculated using Equation 1:

$$R_q = \frac{1}{L}\sqrt{\int_0^L y(x)^2\,dx} \qquad [1]$$

where L is the distance between the scratches and y(x) is the average height above or below the median line for any given position. For all of our profilometer scans, we maintained an in-plane sampling resolution of 0.5 μm as defined by the scan speed and data sampling rate. The thickness measurement accuracy of the profilometer is reported as +/- 0.1 nm. The films were then tested for surface energy using a goniometric setup, with a Navitar CV-M30 camera and Edmund Optics test stand. Five microliters of reagent grade water was placed on the surface of the film, and 5 images were acquired 15-30 seconds after the droplet touched the surface of the polypyrrole. The average contact angle from these images was calculated.

Electrical Conductivity Characterization of PPy Films

Electrical conductivities of the PPy films, ranging in thickness from 0.29 – 1.6 μm, were measured using a Jandel four-point probe (1.0 mm tip spacing) with a CH Instruments, electrochemical analyzer and a Lucas Labs resistivity test stand. The sheet resistivity was then calculated using Equation 2:

$$R_s = \frac{4.5324 * V}{I} \qquad [2]$$

where I [amperes] is the current passed between the two inner electrodes, V [volts] is the voltage across the two outer electrodes, and Rs [Ohms/square] is the sheet resistivity. To accurately measure electrical conductivity of PPy, it is essential to remove the conducting polymer films from the underlying conducting gold or ITO substrates. From our experience, the most effective method for removing the films from the conducting substrates is using double-sided tape and to place the exposed side of the tape onto the surface of a glass slide, a technique with some precedence in the literature (Mabrouk 2005). Other possible methods we have tested in the past include using a razor blade to peel the films off the conducting substrate or backing the film with poly-dimethylsiloxane (PDMS) to aid in removal. When using a razor blade the fragile films tend to roll up on themselves because of their high surface energy. In using PDMS, we found that PDMS can leach through the film and prevent good contact with the four-point probe. Removal with double-sided tape was a practical method to move the film to an insulating substrate without causing damage to the film. From our comparisons, the presence of the tape did not alter the conductivity of the film.

Using the thickness, t [cm], taken from previous profilometer measurements, the conductivity, σ [Siemens/cm], for a given film was then calculated using Equation 3:

$$\sigma = \frac{1}{R_s * t} \qquad [3]$$

Dopant Stability

X-ray photoelectron spectrographs (XPS) and conductance measurements were taken over a two week period for films submerged in either 1 X PBS (pH ~ 7.4) or DDI water (~ 18 MΩ) to determine the dopant stability of PPy films. PBS was chosen because it resembles physiological salt concentrations. For XPS, eight thick films (84 mC/cm2) were electrochemically synthesized for each of the three dopants used in this manuscript. Each film was then washed for five minutes in DDI water and dried in a vacuum desiccator overnight. Immediately after drying, small portions of each film were removed and measured using XPS to calculate a baseline doping level. The remainders of each of the films were placed in a Petri dish and submerged in either PBS or DDI water. Two, seven, and fourteen day time points were also taken by removing additional portions of the films at each time point. Core level X-ray emissions were measured for N(1s), S(2p), Cl(2p), and Na(1s) for each of the samples. The doping ratio was then calculated as a ratio between the dopant anion (S or Cl) and pyrrole ring nitrogen (N). In each sample, low sodium levels verified that proper washing of the films had taken place.

For conductance measurements, eight thick films (84 mC/cm^2) were electrochemically synthesized for each of the three dopants used in this manuscript. All films were allowed to dry in a vacuum desiccator overnight. Films were removed with double-sided tape, cut into equal halves, and put into a watertight well setup. The well setup was created by putting a polydimethylsiloxane (PDMS) layer on a glass slide and then stacking on top the PPy film, two silver wires along opposing edges of the PPy film,

a second layer of PDMS with a 1 x 1.5 cm square removed from the center, and finally a polycarbonate well. All layers were held together by wrapping the edges with electrical tape. This setup ensured a watertight seal to minimize leakage while allowing conductance measurements to be taken in situ. Initial conductance measurements were taken, the wells were filled with PBS or DDI water, and a second set of conductance measurements were obtained to account for changes in conductance due to the solution. Over a two week period of time, additional measurements were acquired to observe the conductance decay. All measurements were taken by passing a small DC current through the silver wires and measuring the resulting voltage. The direction of the current was then switched and the voltage measured again. The strength of the current used was always adjusted to produce a voltage between 10 and 100 mV. The conductance value was then determined by dividing the current by the average voltage.

Cell Culture and Cell Viability Characterization

Schwann cells and rat pheochromocytoma PC-12 cells were cultured on PPy to determine film property effects on cell viability. Both cell types were cultured on six films, thin (10.7 mC/cm^2) and thick (84 mC/cm^2) films for each dopant (Cl, ToS, PSS) on ITO slides. For the PC-12 cell experiment, sterile polycarbonate wells with inner dimensions of 1.0 x 1.5 cm^2 (made in-house) were secured onto the films with UV-sterilized high vacuum grease (Dow Corning, Midland, MI). For the Schwann cell experiments, wells with inner diameters of 9 mm were made from sterile Press-to-Seal Silicone Isolators (Grace Bio Labs, Bend, OR) and were secured onto films with UV-sterilized high vacuum grease. Before culturing cells, the wells attached to polypyrrole films on glass were sterilized for 30 minutes using UV exposure and washed for 10

minutes using 1 mL phosphate buffered saline (PBS) for the large wells and 100 μL PBS for the small wells.

Rat pheochromocytoma PC-12 cells from American Type Culture Collection were selected for this study because of their ability to differentiate into a neuronal phenotype after exposure to nerve growth factor (NGF). PC-12 cells were maintained in F12K medium with 10% horse serum and 5% fetal bovine serum on collagen-coated polystyrene tissue culture dishes (2.75 μg rat tail Collagen I per 10cm diameter dish, Sigma-Aldrich, St. Louis, MO). Cells were exposed to 50 ng/mL NGF (2.5S Murine, Promega, Madison, WI) for 5 days prior to seeding on PPy substrates, changing medium on the third day, and maintained in a humid 37°C, 5% CO2 incubator. Cells were detached using 0.25% Trypsin-EDTA, resuspended and triturated before seeding the cells at 20,000 cells per well (13,000 cells/cm^2). Cultures grown on PPy were maintained in 300 μL of medium containing serums, NGF, and 1% penicillin/streptomycin/amphotericin B (PSA) for 24 hours.

Schwann cells were also selected for this study because Schwann cell migration precedes axon regrowth at a neural injury site. Cells were isolated from P4 neonatal rat sciatic nerves using a modified Brockes method to obtain 95% cell purity as measured by S-100 immunostaining. Schwann cells were maintained in high glucose DMEM medium with 10% fetal bovine serum, 3 μg/mL of bovine pituitary extract (Invitrogen, Carlsbad, CA), and 2 μM forskolin (Sigma-Aldrich, St. Louis, MO) on 10 cm diameter poly-l-lysine (PLL) coated tissue culture dishes (2 μg/cm^2, Fisher Scientific, Pittsburgh, PA). Cells were cultured to 70-80% confluency, then detached using 0.25% Trypsin-EDTA and seeded at 6000 cells per well (9,500 cells/cm^2). Cultures grown on polypyrrole were maintained in 100 μL of medium containing serum, supplements, and 1% PSA for 24 hours.

Measurement of PC-12 and Schwann cell viability on polypyrrole was assessed using a luminescent ATP detection assay (CellTiter Glo, Promega, Madison, WI). The wells were aspirated and then incubated with 100 μL of fresh medium and 100 μL of detection reagent. After 30 minutes, the supernatant was pipetted into a 96-well plate and analyzed with a luminescent microplate reader (FLx800, BioTek Instruments, Inc., Winooski, VT). Calibration curves for luminescent values correlating to cell numbers were created for each experiment.

Leached products from thick PPy substrates were used to examine cytotoxic effects on Schwann cells. Sterile Silicon Isolator wells were secured onto thick PPy films and onto PLL-coated tissue culture dishes with UV-sterilized high vacuum grease. Wells on PPy films and Schwann cells seeded on PLL plates were both incubated 24 hours at 37°C with 100 μL of medium containing serum and supplements. Following the 24 hour incubation, media was aspirated from the Schwann cell cultures and replaced with media incubated on the thick PPy films. After cells were cultured for another 24 hours, cell viability was measured using an ATP assay.

Statistics and Error Propagation

In all calculations, the general relation of propagation of uncertainty was used. To determine statistical significance, sample sizes (given as the variable n) of three or greater were used for all characterization techniques. Standard error was reported for all relevant figures. Two-tailed Student t-tests were performed for each of the values of interest for cell studies, contact angle studies, and conductivity studies. Statistically significant groups in Figures 3.3, 3.5 and 3.8 are identified at the 0.05 level with different letters (A,

B, or C); groups with the same letter are not statistically significant. Only comparisons that had a p-value of 0.05 or less were considered statistically significant.

3.3 Results and Discussion

PPy Film Thickness

Film thickness is an important parameter to consider for cell studies either in vivo or in vitro. The electrochemical polymerization of PPy was reported to be a stoichiometric process (Diaz and Hall 1983), with between 2.2 and 2.4 electrons passed per monomer unit polymerized. The slight variability in the process depends on the doping level of the film (Diaz and Hall 1983). Unfortunately, subsequent studies suggest that other factors may affect the "yield" or efficiency of this reaction, such as oligomers that remain in solution and undesired side reactions (Vernitskaya and Efimov 1997). With these findings in mind, our goal was to assess how well film thickness may be predicted using standard electrochemical synthesis techniques.

Figure 3.1 illustrates the correlation between film thickness and charge passed per unit area in a log-log plot. A linear trend was fitted to the data with the y-axis intercept set to zero. The linear fits for ToS- and PSS-doped films have similar slopes for both substrates and R2 values greater than 0.83. Chloride-doped films produced the steepest slope (seen as a parallel line shifted upwards in a log-log plot) for both conductive substrates, demonstrating that Cl-doped films grow much thicker than PSS- or ToS-doped films. Chloride-doped film growth also had very low correlation with charge passed, yielding R2 values of 0.53 for gold and 0.77 for ITO substrates. This translates to an average error of 26%, 36%, and 183% between the calculated thickness and the actual thickness for PSS-, ToS-, and Cl-doped films, respectively. Perhaps more interesting,

however, is the observation that for the same amount of charge passed, Cl-doped films are over twice as thick as PSS- or ToS-doped films when polymerized on a gold substrate and roughly eight times as thick when polymerized on ITO.

Theoretical, stoichiometric calculations were performed based on the equation given by Stankovic, et al. (1994) to compare experimental thickness measurements to their predicted values. The slopes of the regression lines in Figure 3.1 along with theoretical values are shown in **Table 3.1**. Since electropolymerization of PPy requires the passage of two electrons per pyrrole ring plus an electron for each dopant ion incorporated, the thickness, Th, of the films per charge passed per unit area should be given by:

$$\frac{Th}{Q_0/A} = \frac{(M_m + yM_a)}{d(2/\gamma + y)F}\frac{p}{(p-1)} \qquad [4]$$

where Q_0 is the charge passed, A is the surface area of the working electrode, d is the density of doped PPy, y is the degree of polymerization, and M_m and M_a are the molecular weights of the pyrrole repeat unit and the dopant anion respectively. Gamma (γ) represents the efficiency of the applied current and p is the degree of polymerization. The slopes reported in Table 1 use the approximations that γ=1, that p is very large, that y=0.3, and that d=1.5 g/mol. Experimental observations for the film growth of ToS- and PSS-doped PPy are relatively near stoichiometric predictions, but Cl-doped PPy films were thicker than predicted, especially for higher charge passed per area values. Previous studies using ClO_4 as the dopant have also reported films thicker than theoretical predictions (Stankovic, Pavlovic et al. 1994), postulating decreases in density as the primary cause.

It is well known that synthesis current densities (charge passed per area per time) have significant effects on film morphology and conductivity (Maddison and Unsworth 1989; Schmeisser, Naarmann et al. 1993; Stankovic, Pavlovic et al. 1994). The main difference between the substrates used, ITO and gold, is conductivity. As a result of the higher conductivity of gold, electrochemical synthesis on gold substrates tends to occur faster than on ITO. **Figure 3.2** shows that the current density is indeed greater for those films synthesized on gold than those synthesized on ITO for all dopants. Furthermore, Figure 3.2 shows a tight distribution on both substrates for all dopants except chloride. Other studies (Schmeisser, Naarmann et al. 1993; Bufon, Vollmer et al. 2005) also report that current density during synthesis affects chain length and chain disorder, which may explain some of the variability observed when correlating thickness to charge passed for Cl-doped films. The optimal current density found by Stankovic for tosylate-doped films of 1 mA/cm^2 aligns well with the median value found for films synthesized on gold substrates.

Contact Angle Measurements

The water contact angle of smooth surfaces is a relative measure of the surface energy of the material (Yekta-Fard and Ponter 1992). Materials with higher surface energies (i.e., materials that are more hydrophilic) exhibit better cell adhesion (Hallab, Bundy et al. 2001). Water contact angles for relatively smooth films (less than 50 nm root mean squared roughness in our case) for each of the dopants were used to compare surface energy as a function of dopant type. These smooth samples were chosen since roughness is a source of error for contact angle measurements (Yekta-Fard and Ponter 1992). **Figure 3.3** shows that PPy films doped with PSS, a polyanionic molecule, have

more hydrophilic surfaces than those films doped with monoanionic dopants such as Cl and ToS. This result is expected and is likely explained by free charges in the longer strands of PSS in the PSS-doped films whereas no such free charges exist in the Cl- and ToS-doped films.

Surface Roughness

Surface roughness is an important consideration for cell adhesion; thus, changes in roughness as a result of different dopants and different thicknesses must be taken into account. We noticed that film growth on our two substrates, gold and ITO, were distinct, so comparisons between substrates were also expected to show differences. Also, since the roughness of an amorphous material inherently contains a high level of variance, this analysis is descriptive of general trends and cannot be used to reproducibly generate films with a specific roughness.

Figure 3.4 shows how roughness increases with thickness for the three dopants used; in addition, three typical thickness profiles of thick films obtained using profilometry are shown. PSS-doped PPy was by far the smoothest material, with roughness remaining almost constant for all thicknesses. Qualitatively, while observing the polymerization on the substrate, the PSS-doped PPy film grew evenly across the substrate. The fact that PSS-doped PPy adsorbs uniformly on the electrode (with more nucleation points) may be caused by the large PSS dopant polyanion adsorbing to the electrode and providing a favorable surface for further PPy adsorption (Vernitskaya and Efimov 1997). For thin samples, ToS-doped PPy also maintains essentially constant roughness, but samples thicker than a few hundred nanometers increase in roughness as they become thicker. Chloride-doped PPy films were much rougher than PSS- and ToS-

doped PPy, and roughness rapidly increased with thickness. Roughness values obtained are within the range of previously published values obtained by scanning tunneling microscopy (Chainet and Billon 1998). From observation, Cl-doped PPy films deposited unevenly during polymerization and usually started from only a few nucleation points. When comparing the roughness of samples between the gold and ITO substrates, no significant change in roughness was observed (data not shown). Although differences in the growth and macroscopic uniformity of the films were observed, this did not significantly affect the micrometer scale roughness. Mabrouk (2005) also report no correlation between substrate and surface morphology on the nanometer scale based on atomic force microscopy (AFM) data.

Conductivity Measurements

Figure 3.5 shows the conductivity of PPy films for the three dopants tested. ToS-doped PPy films have conductivities ten times higher than either PSS-doped or Cl-doped films. The conductivity measured for tosylate-doped films correlates well with the 60 Ω-1cm-1 value reported by Maddison and Unsworth (1989). Films that were doped with PSS had slightly higher conductivities than Cl-doped films. Since ToS is fundamentally a monomer unit of PSS, the observed difference in conductivities between PSS- and ToS-doped films is likely the result of lower doping levels in PSS-doped films. Because of steric hindrances, only a fraction of the charges on a strand of PSS will be able to effectively dope PPy aromatic rings. The remaining charges, although entrapped in the film, will not increase the conductivity of the film. For ToS ions, however, it is possible for every incorporated ion to dope the film. The difference in conductivity between Cl-doped and ToS-doped films is likely caused by multiple factors. Chloride has roughly a

sixth of the mass of ToS, and diffuses out of the films quickly, as supported by the XPS and conductivity measurements reported in Figure 3.8. The washing and drying protocol implemented likely reduced the conductivity of the Cl-doped films more than that of ToS-doped films. Our own experience and other previous studies (Kuhn, Child et al. 1995; Chehimi and Abdeljalil 2004) indicate that the conductivity of ToS-doped films is more stable than Cl-doped films. As reported by Vernitskaya and Efimov (1997), the size and nucleophilicity of the dopant anion itself affects the electrical conductivity as well, making ToS-doped PPy more conductive.

Dopant Stability

PPy owes its high conductivity to the dopant ions that serve as an electrical bridge between polymer molecules. Loss of stability in these doping interactions, therefore, leads to a loss in conductivity. For long-term, conductive implants, such as neural probes, stable doping is of paramount importance. Two techniques were employed to test PPy doping stability from an electrical perspective and a chemical composition perspective. In the first, PPy films were stored at room temperature in PBS and DDI water for 0-14 days and their conductance was measured daily. In the second technique, PPy films stored at room temperature in PBS and DDI water for zero, two, seven, and fourteen days were analyzed using XPS measurements for nitrogen, sodium, sulfur and chlorine. Since PPy contains one nitrogen atom per monomer unit, the doping ratio of PPy can be calculated by dividing the number of dopant ions (either sulfur or chloride in our case) by the number of nitrogen atoms. In the context of XPS measurements, the ratio of atomic concentration percentages was used to calculate the doping ratio.

Figure 3.6 shows XPS and conductance data for PPy films in water and PBS. For PSS-doped films, it should be noted that XPS measurements capture each anion in the molecule whether it is actually doping the film or just sterically bound to the surface. XPS data indicate that some PSS was lost over the first few days, but then stabilized. Conductance, however, continued to decrease over time, indicating that even though anions were entrapped within the film, they slowly lost their doping interactions. The continued degradation in conductance for PSS-doped films can likely be attributed to the reduction of the nitrogen in the PPy backbone. The conductance and XPS data show that both ToS- and PSS-doped films decayed faster in PBS than in DDI water. This is believed to be caused by ions in solution that may either displace dopant ions or extinguish the charge interactions between PPy and dopant. The Cl-doped PPy conductance decayed more rapidly in DDI water than in PBS because the diffusion gradient existing in water was greater than in PBS solution. Unfortunately, this was not verified by the XPS data, as the chloride atomic composition in the polymer effectively reached zero for both solutions within two days.

Cell Studies

PPy films of two thicknesses, thin (10.7 mC/cm^2 of charge passed, ~150 nm average thickness) and thick (84 mC/cm^2, ~650 nm average thickness), and with each of the three dopants were compared in terms of their ability to support cell growth. **Figure 3.7a** shows phase contrast images of PC-12 cells cultured on the three different PPy substrates. Qualitatively this figure shows that differences in cell spreading did occur for our different substrate conditions. PC-12 cells are able to clump together and survive through cell-cell interactions without attaching to the substrate, which can partially mask

differences in cell viability. As such Schwann cells were chosen as a comparative study. **Figure 3.7b** shows corresponding phase contrast images of Schwann cells. Different cell morphologies can qualitatively seen for each of the dopants used (inset). Schwann cells grown on PSS-doped PPy seem to prefer a thin, spindle-like morphology, whereas films doped with the other two dopants seem to prefer alternative more spread morphology. **Figures 3.8a and 3.8b** show that regardless of the cell type used, ToS- and PSS-doped thick films resulted in lower cell adhesion versus their corresponding thin film ($p < 0.05$). Leaching studies were performed with Schwann cells and revealed that medium incubated on thick ToS films resulted in significantly lower cell numbers, confirming that leached dopant molecules may contribute to this decrease (data not shown). Thick chloride films performed as well or better than thin films. As leaching of chloride is not cytotoxic in these quantities, surface roughness may help promote cell adhesion on thick Cl-doped films. Comparing across dopants with PC-12 cells, thick chloride films performed the best ($p < 0.05$). It is interesting to note that negative surface charges on PSS-doped films, which have been known to promote protein adsorption and subsequent cell adhesion (Cai, Frant et al. 2006; Khorasani, MoemenBellah et al. 2006; Wittmer, Phelps et al. 2007), do not exhibit a significant effect on cell viability of PC-12 cells. On the other hand, for Schwann cells thick PSS-doped PPy films are statistically better than thick ToS-doped films ($p < 0.05$). This is of particular importance as serum proteins such as fibronectin and laminin I and II are known to have significant effects on Schwann cell behavior, including migration (Bailey, Eichler et al. 1993; Einheber, Milner et al. 1993).

3.4 CONCLUSIONS

PPy is an extremely versatile and promising material for biomedical applications; however, to create a film with tightly controlled properties such as roughness, thickness, and conductivity, the synthesis process must be well refined and the dopants incorporated must be carefully chosen. This study demonstrated that different dopants yield vastly different materials properties, which could be important for different biomedical applications. For example, in situations requiring high conductivity, such as electrode coatings, ToS-doped PPy films are far more conductive than PSS- or Cl-doped PPy films. On the other hand, PSS-doped PPy maintains its composition over long periods of time and has a smoother, more hydrophilic surface, making it a good candidate for longer term implants such as neural probes. Chloride produces high surface roughness for thicker films, which enhances cell viability, but this material also de-dopes rapidly. With regard to electrochemically synthesizing films of a specified thickness, charge passed per unit area is a marginal indicator of thickness for PSS- and ToS-doped PPy films, but a poor indicator for Cl-doped films. Further investigation is required to explain this variability, but we conclude that the practice of reporting charge passed to infer film thickness has poor accuracy and is insufficient for applications requiring high precision. The cell viability studies showed the importance of both dopant and film thickness, with dopant leaching and film surface roughness playing dominant roles in the differences observed. As PPy becomes more widely used in a variety of settings with a variety of synthesis parameters used, the most important conclusion may be that careful control over the synthesis process is required to consistently produce films or coatings with desired characteristics.

Table 3.1 – Relationship Between PPy Film Thickness and Charge Passed per Area

Dopant	Film Growth Rate on ITO Substrates ($nm/mC/cm^2$)	Film Growth Rate on Gold Substrates ($nm/mC/cm^2$)	Theoretical Film Growth Rate ($nm/mC/cm^2$)*
Cl	34.5	8.72	2.27
ToS	4.91	3.47	3.50
PSS	3.72	3.47	3.61

*Calculated from Equation [4] (Stankovic, *et al*. 1994).

3.5 FIGURES

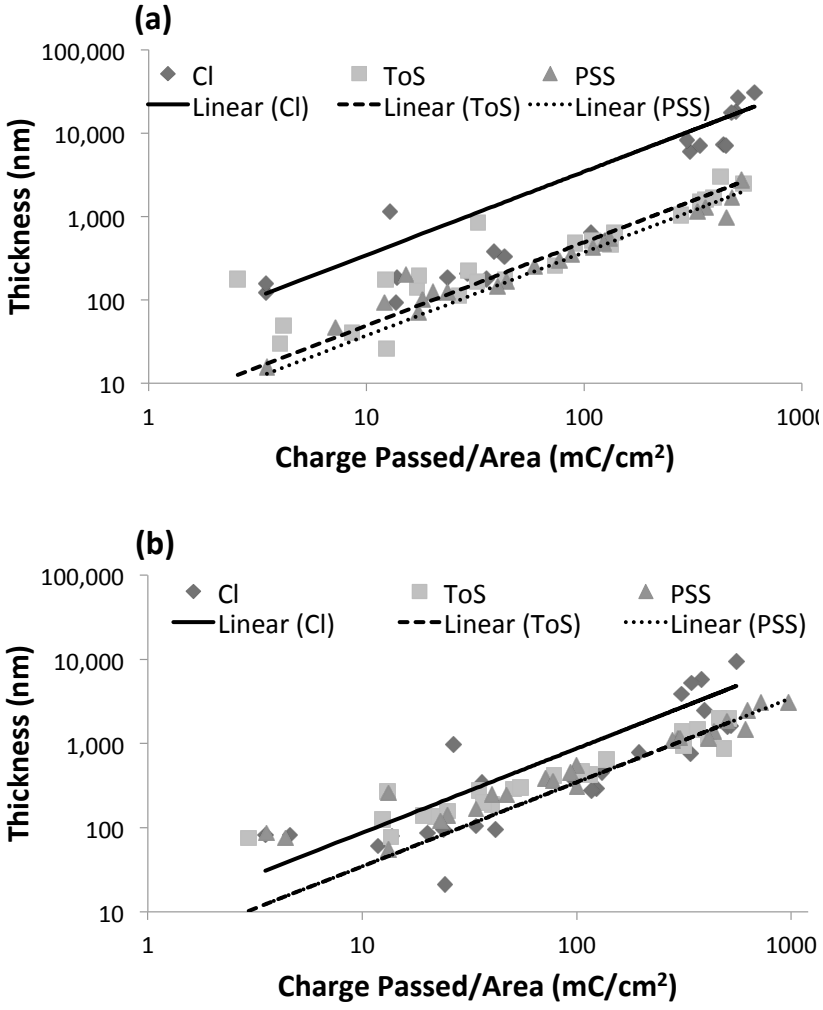

Figure 3.1 – Correlation Between PPy Film Thickness and Charge Passed per Area.

Thicknesses in nanometers versus charge passed per area are plotted in a log-log plot for all three dopants for both ITO (a) and gold (b) conductive substrates. A linear correlation was observed for all three dopants for each of the conductive substrates, but Cl-doped films exhibited high variability, demonstrating that charge passed is not a good indicator of thickness for Cl-doped films. ToS and PSS dopants yielded similar slopes, whereas Cl-doped films yielded slopes eight fold (ITO; a) and two fold (gold; b) higher, indicating that the relationship between thickness and charge passed is highly dependent on both dopant and substrate. For all dopants, films grown on ITO films were thicker than films grown on gold for equal quantities of charge passed per unit area. This change in yield may be related to deposition rate (also measured as current densities).

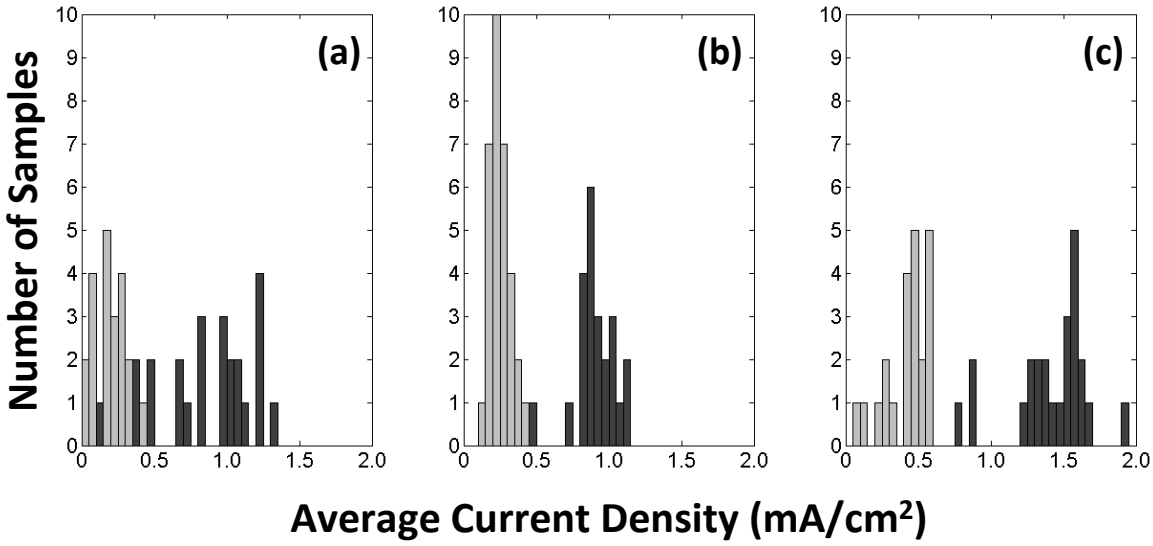

Figure 3.2 – Histograms of the Average Current Density (charge passed/(area*time)) in Electrochemical Syntheses.

Syntheses on ITO (light gray) and gold (dark gray) are shown for Cl-doped films (a), ToS-doped films (b), and PSS-doped films (c). Gold electrode substrates consistently resulted in higher current density and thus higher deposition rates, which may impact the yield or efficiency of the amount of material polymerized for a given charge passed. The higher variability in the current density during Cl-doped film synthesis may relate to high variability of film thicknesses observed. All syntheses were performed under the same conditions: 0.1 M concentration of pyrrole and dopant ions, room temperature, neutral pH, and aqueous solvent (distilled, de-ionized water).

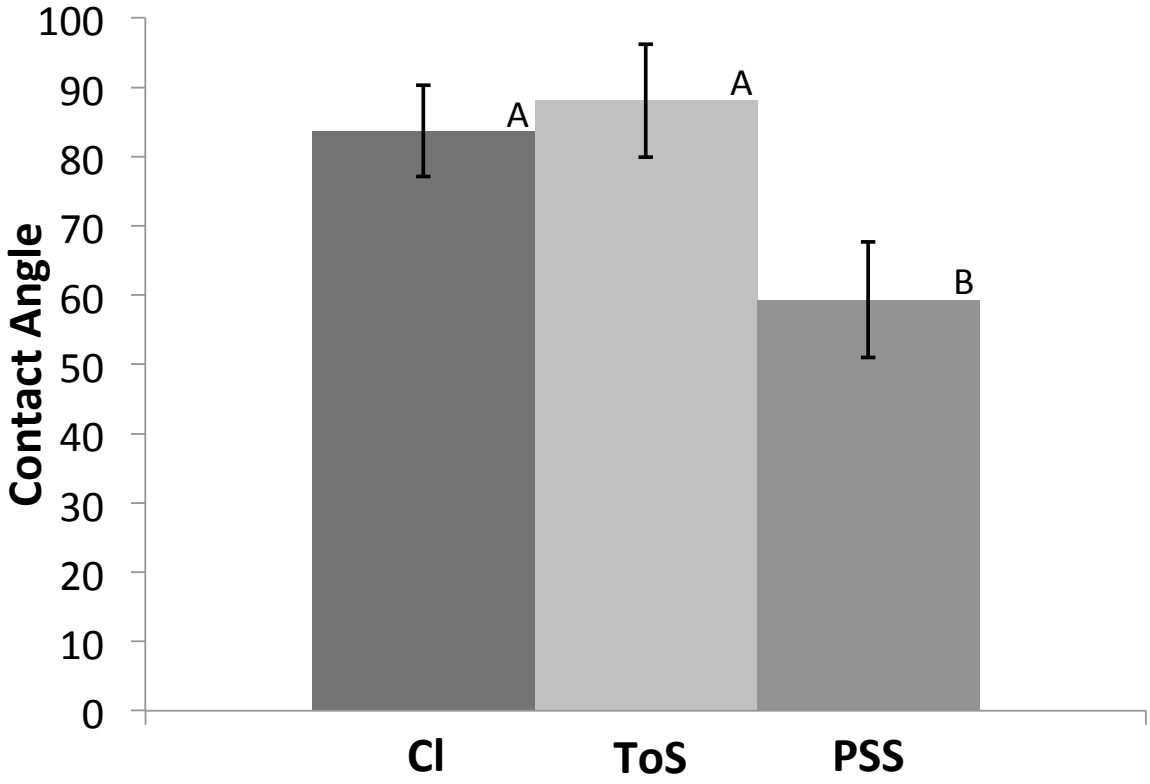

Figure 3.3 – Contact Angles for PPy Films.

The contact angle for PPy films with Cl and ToS dopants are statistically more hydrophobic than PSS-doped PPy films. This is likely a result of the free charges found on the longer PSS strands in PSS-doped films. Statistically significant groups are identified at the 0.05 level with different letters (A or B) above each bar graph. (For Cl and ToS, n=4. For PSS, n=7)

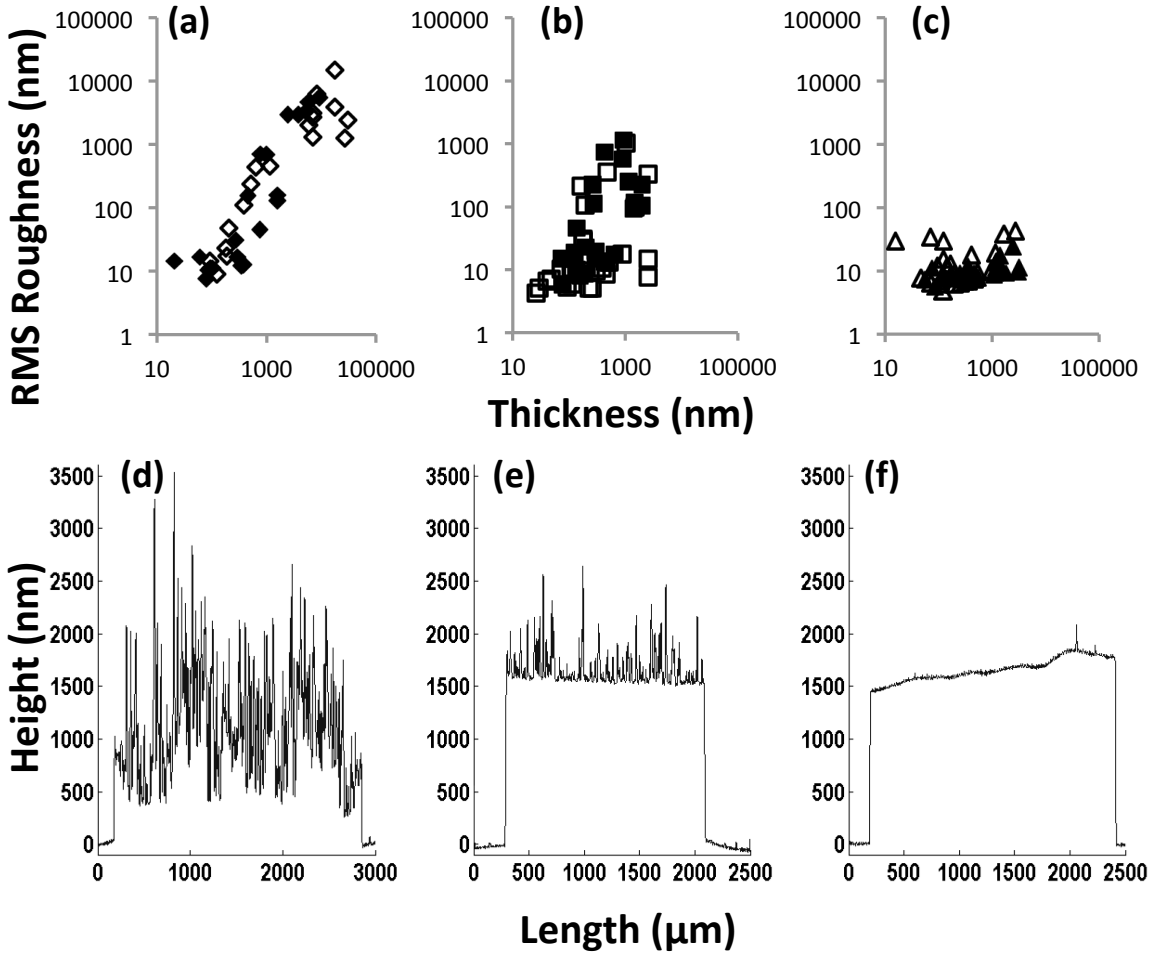

Figure 3.4 – PPy Film Roughness.

Roughness values at various thicknesses for the three dopants: Cl (a), ToS (b), and PSS (c). The roughness of Cl-doped films increases with thickness, whereas the roughness of PSS-doped films remains almost constant for all thicknesses measured. Films synthesized on ITO substrates are denoted as hollow symbols, and films on gold substrates are shown as solid symbols. No significant difference was observed between these groups. Typical profilometer measurements of Cl-doped PPy (d), ToS-doped PPy (e), and PSS-doped PPy (f) are shown as a qualitative example of the differences in topography.

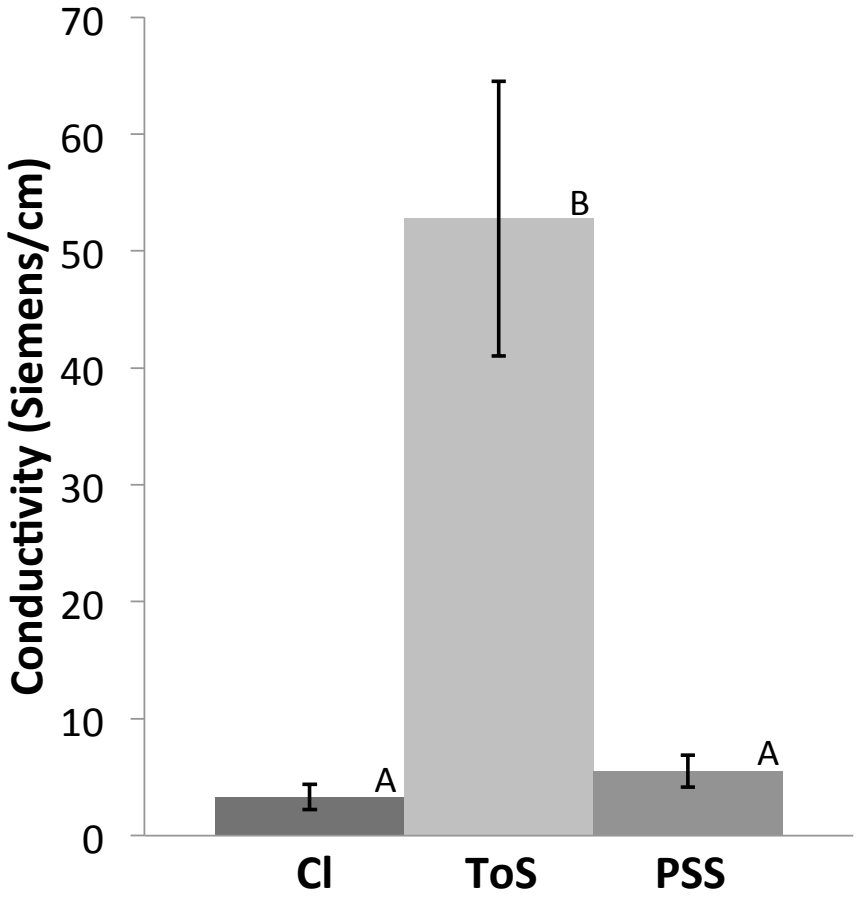

Figure 3.5 – Conductivity as a Function of Dopant.

Conductivity measurements of doped PPy films demonstrate that ToS-doped films are ten times more conductive than PSS- or Cl-doped films. PSS-doped films have a slightly higher conductivity than Cl-doped films. Since PSS is fundamentally a polymerized form of ToS, this difference in conductivity most likely relates to the entrapment of a proportion of PSS ions that do not actually dope PPy. For a PSS molecule in a PPy film, steric hindrances only allow a fraction of the anions on the molecule to contribute to the conductivity of the film. ToS ions, in contrast, are able to move more freely to allow stronger doping interactions with PPy. On the other hand, the small size and high solubility of chloride make it a less stable dopant, and the washing steps of our protocol may have disrupted the doping interactions, resulting in de-doping and thus less conductive Cl-doped films. Statistically significant groups are identified at the 0.05 level with different letters (A or B) above each bar graph. (n = 5)

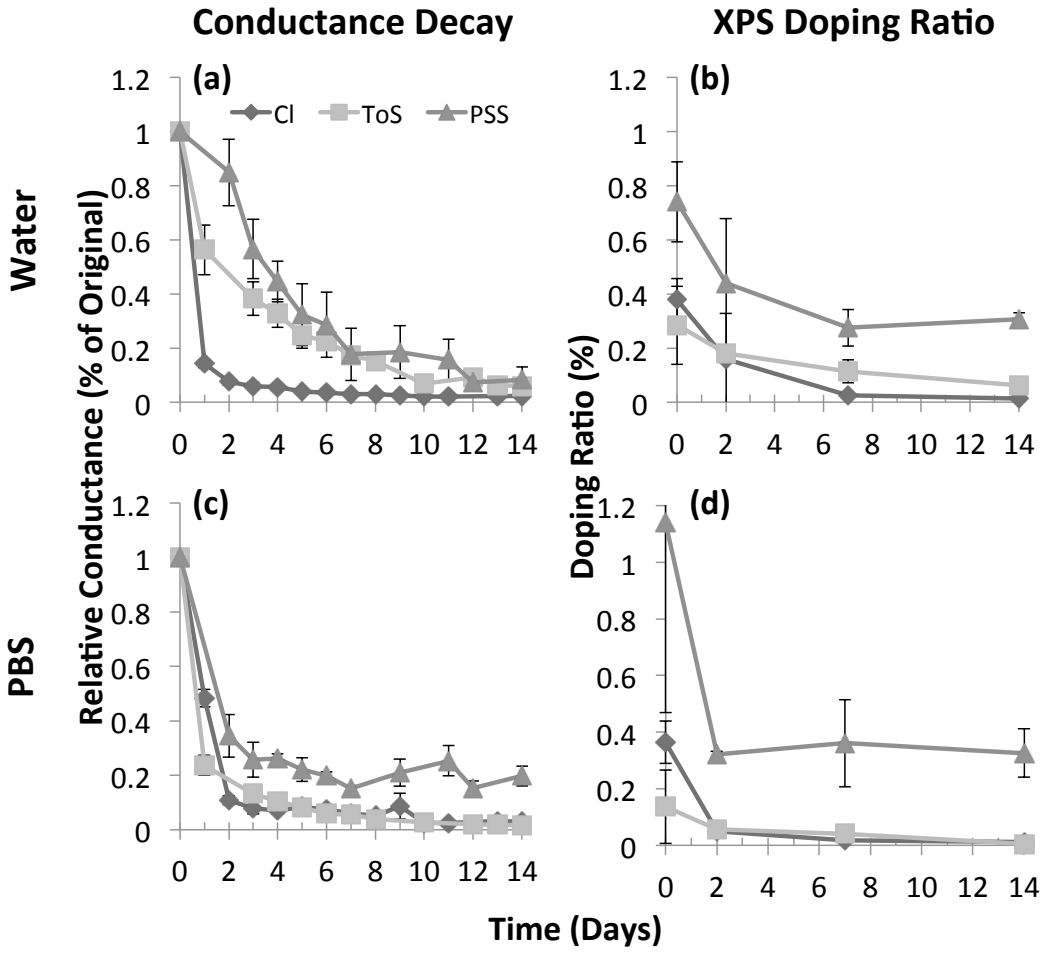

Figure 3.6 – Dopant Stability in Physiological Conditions.

Conductance measurements of thick PPy films (84 mC/cm^2) doped with each of the three dopants (Cl, ToS, and PSS) immersed in either DDI water (a) or PBS (c) are shown over a fourteen day time period. The doping ratios (ratio of dopant ions to pyrrole rings) calculated from X-ray photoelectron spectrographs show chemical composition data for films stored in water (b) or PBS (d). For PSS, both XPS and conductance data show a decrease over the first few days with conductance data continuing to decrease over the entire period even though the chemical composition stabilizes. This suggests that even though PSS molecules remain entrapped within the film they slowly lose their doping interactions. The conductance and XPS data show that both ToS- and PSS-doped films decay faster in PBS than in DDI water because of salt interactions. Because of the larger diffusion gradient, Cl-doped films degraded faster in DDI water than in PBS.

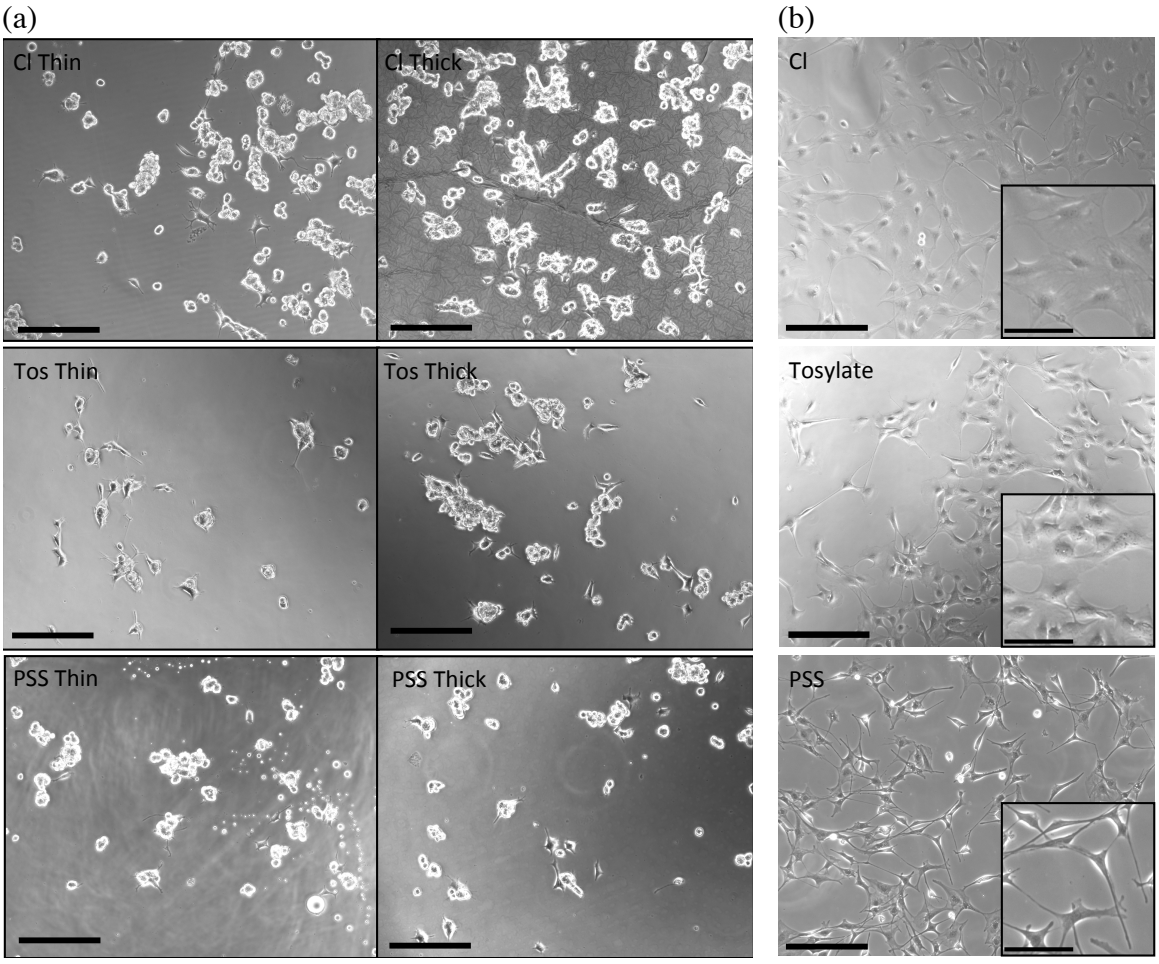

Figure 3.7 – Phase Contrast Images of Cell Cultures on PPy Films.

(a) PC-12 cells were cultured for 24 hours on sterilized films and phase contrast images were taken for both thin films (10.7 mC/cm^2 of charge passed) and thick films (84 mC/cm^2). Qualitatively this figure shows that differences in cell spreading did occur for our different substrate conditions. PC-12 cells tend to aggregate and survive as a result of cell-cell interactions without attaching to the substrate, which can partially mask differences in cell viability. Scale bar = 250 μm. (b) Schwann cells were cultured for 24 hours on sterilized films and phase contrast images were taken for thin films (10.7 mC/cm^2 of charge passed). Different cell morphologies are observed for each of the dopants used (inset). Schwann cells grown on PSS-doped PPy adopted a thin, elongated bipolar morphology whereas cells on Cl- and ToS-doped films exhibited a spread morphology. Scale bar = 250 μm. Inset Scale bar = 50 μm.

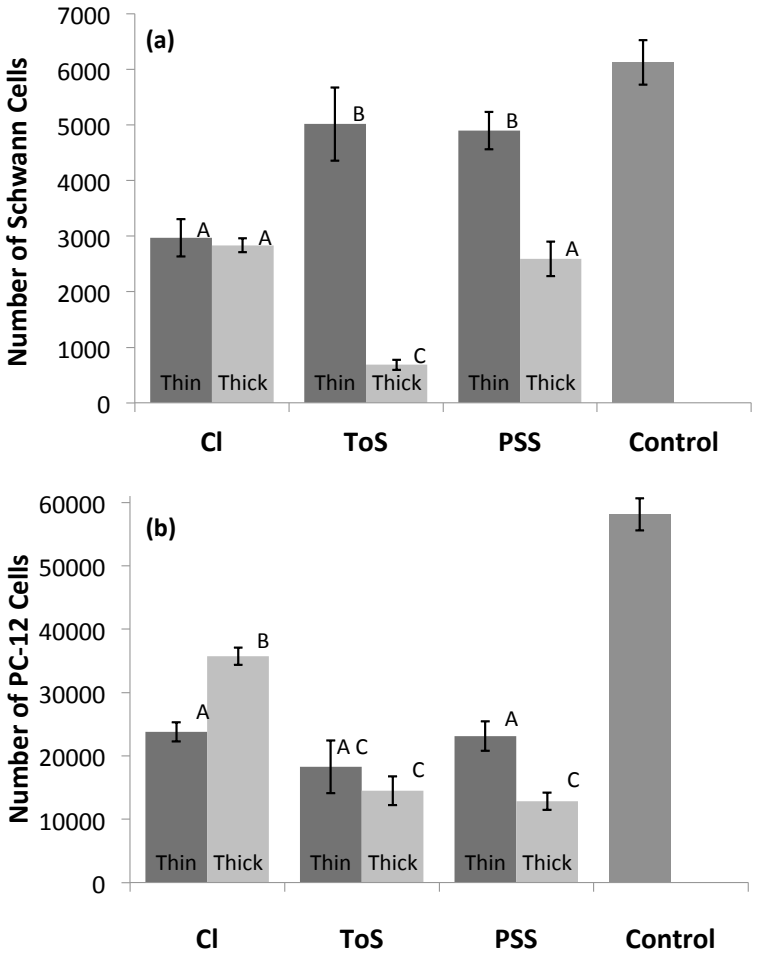

Figure 3.8 – Cell Viability on Thick and Thin PPy Films.

For all samples, Schwann (a) and PC-12 (b) cells were cultured for 24 hours on sterilized films. Viable cell numbers were calculated by luminescent ATP detection using a calibration curve. Regardless of the cell type used, ToS- and PSS-doped thick films (84 mC/cm^2) resulted in lower cell adhesion compared to their corresponding thin films (10.7 mC/cm^2 of charge passed). Thick chloride films performed as well or better than thin films, possibly because of changes in surface roughness. (a) Schwann cells cultured on thick and thin films of each dopant type (average ± standard error). A PLL-coated plate was used as the positive control. Statistically significant groups are identified at the 0.05 level with different letters (A, B, or C) above each bar graph. n = 16. (b) PC-12 Cells cultured on thick and thin films of each dopant type (average ± standard error). A collagen-coated plate served as the positive control. Statistically significant groups are identified at the 0.05 level with different letters (A, B, or C) above each bar graph. n = 9.

3.6 REFERENCES

Al-Majed, A. A., C. M. Neumann, et al. (2000). "Brief electrical stimulation promotes the speed and accuracy of motor axonal regeneration." The Journal of Neuroscience **20**(7): 2602.

Bailey, S., M. Eichler, et al. (1993). "The influence of fibronectin and laminin during Schwann cell migration and peripheral nerve regeneration through silicon chambers." Journal of neurocytology **22**(3): 176-184.

Bentley, D. and T. P. O'Connor (1994). "Cytoskeletal events in growth cone steering." Current opinion in neurobiology **4**(1): 43-48.

Bolto, B., R. McNeill, et al. (1963). "Electronic conduction in polymers. III. Electronic properties of polypyrrole." Australian Journal of Chemistry **16**(6): 1090-1103.

Bray, D. and P. Hollenbeck (1988). "Growth cone motility and guidance." Annual review of cell biology **4**(1): 43-61.

Bufon, C. C. B., J. Vollmer, et al. (2005). "Relationship between chain length, disorder, and resistivity in polypyrrole films." The Journal of Physical Chemistry B **109**(41): 19191-19199.

Cai, K., M. Frant, et al. (2006). "Surface functionalized titanium thin films: zeta-potential, protein adsorption and cell proliferation." Colloids and Surfaces B: Biointerfaces **50**(1): 1-8.

Carquigny, S., O. Segut, et al. (2008). "Effect of electrolyte solvent on the morphology of polypyrrole films: Application to the use of polypyrrole in pH sensors." Synthetic Metals **158**(11): 453-461.

Chainet, E. and M. Billon (1998). "In situ study of polypyrrole morphology by STM: effect of the doping state." Journal of Electroanalytical Chemistry **451**(1-2): 273-277.

Chehimi, M. M. and E. Abdeljalil (2004). "A study of the degradation and stability of polypyrrole by inverse gas chromatography, X-ray photoelectron spectroscopy, and conductivity measurements." Synthetic Metals **145**(1): 15-22.

Clark, P., P. Connolly, et al. (1990). "Topographical control of cell behaviour: II. Multiple grooved substrata." Development **108**(4): 635.

Cui, X., J. Wiler, et al. (2003). "In vivo studies of polypyrrole/peptide coated neural probes." Biomaterials **24**(5): 777-787.

Diaz, A. (1981). "Electrochemical Preparation and Characterization of Conducting Polymers." Chemica Scripta **17**: 145-148.

Diaz, A. and K. K. Kanazawa (1983). Polypyrrole: An Electrochemical Approach to Conducting Polymers. New York and London, Plenum Press.

Diaz, A. F. and B. Hall (1983). "Mechanical-Properties of Electrochemically Prepared Polypyrrole Films." Ibm Journal of Research and Development **27**(4): 342-347.

Dowell-Mesfin, N., M. Abdul-Karim, et al. (2004). "Topographically modified surfaces affect orientation and growth of hippocampal neurons." Journal of Neural Engineering **1**: 78.

Einheber, S., T. A. Milner, et al. (1993). "Axonal regulation of Schwann cell integrin expression suggests a role for alpha 6 beta 4 in myelination." The Journal of cell biology **123**(5): 1223.

Frostick, S. P., Q. Yin, et al. (1998). "Schwann cells, neurotrophic factors, and peripheral nerve regeneration." Microsurgery **18**(7): 397-405.

George, P. M., D. A. LaVan, et al. (2006). "Electrically Controlled Drug Delivery from Biotin Doped Conductive Polypyrrole." Advanced Materials **18**(5): 577-581.

George, P. M., A. W. Lyckman, et al. (2005). "Fabrication and biocompatibility of polypyrrole implants suitable for neural prosthetics." Biomaterials **26**(17): 3511-3519.

Guimard, N. K., N. Gomez, et al. (2007). "Conducting polymers in biomedical engineering." Progress in Polymer Science **32**(8-9): 876-921.

Hallab, N. J., K. J. Bundy, et al. (2001). "Evaluation of metallic and polymeric biomaterial surface energy and surface roughness characteristics for directed cell adhesion." Tissue Engineering **7**(1): 55-71.

Hodgson, A. J., M. John, et al. (1996). Integration of biocomponents with synthetic structures: use of conducting polymer polyelectrolyte composites. SPIE.

Kang, E. T., Neoh, K. G., Tan K. L. (1997). Photoelectron Spectroscopy of Conductive Polymers. New York, John Wiley & Sons.

Kaynak, A. (1997). "Effect of synthesis parameters on the surface morphology of conducting polypyrrole films." Materials research bulletin **32**(3): 271-285.

Khorasani, M., S. MoemenBellah, et al. (2006). "Effect of surface charge and hydrophobicity of polyurethanes and silicone rubbers on L929 cells response." Colloids and Surfaces B: Biointerfaces **51**(2): 112-119.

Kotwal, A. and C. E. Schmidt (2001). "Electrical stimulation alters protein adsorption and nerve cell interactions with electrically conducting biomaterials." Biomaterials **22**(10): 1055-1064.

Kuhn, H. H., A. D. Child, et al. (1995). "Toward real applications of conductive polymers." Synthetic Metals **71**(1-3): 2139-2142.

Mabrouk, P. A. (2005). "Oxidative electropolymerization of pyrrole from neat monomer solution." Synthetic Metals **150**(1): 101-105.

Maddison, D. and J. Unsworth (1989). "Optimization of synthesis conditions of polypyrrole from aqueous solutions." Synthetic Metals **30**(1): 47-55.

Miller, C., S. Jeftinija, et al. (2002). "Synergistic effects of physical and chemical guidance cues on neurite alignment and outgrowth on biodegradable polymer substrates." Tissue Engineering **8**(3): 367-378.

Ming, G., J. Henley, et al. (2001). "Electrical activity modulates growth cone guidance by diffusible factors." Neuron **29**(2): 441-452.

Pini, A. (1994). "Axon Guidance: Growth cones say no." Current Biology **4**(2): 131-133.

Sadki, S., P. Schottland, et al. (2000). "The mechanisms of pyrrole electropolymerization." Chem. Soc. Rev. **29**(5): 283-293.

Schmeisser, D., H. Naarmann, et al. (1993). "The two-dimensional structure of polypyrrole films." Synthetic Metals **59**(2): 211-221.

Schmidt, C. E., V. R. Shastri, et al. (1997). "Stimulation of neurite outgrowth using an electrically conducting polymer." Proceedings of the National Academy of Sciences of the United States of America **94**(17): 8948-8953.

Serra Moreno, J., S. Panero, et al. (2008). "Synthesis and characterization of new electroactive polypyrrole-chondroitin sulphate A substrates." Bioelectrochemistry **72**(1): 3-9.

Skotheim, T. A. and J. R. Reynolds (2007). Handbook of conducting polymers, CRC.

Stankovic, R., O. Pavlovic, et al. (1994). "The effects of preparation conditions on the properties of electrochemically synthesized thick films of polypyrrole." European polymer journal **30**(3): 385-393.

Suarez, M. F. and R. G. Compton (1999). "In situ atomic force microscopy study of polypyrrole synthesis and the volume changes induced by oxidation and reduction of the polymer." Journal of Electroanalytical Chemistry **462**(2): 211-221.

Vernitskaya, T. V. and O. N. Efimov (1997). "Polypyrrole: a conducting polymer; its synthesis, properties and applications." Russian chemical reviews **66**: 443.

Wang, X., X. Gu, et al. (2004). "Evaluation of biocompatibility of polypyrrole in vitro and in vivo." Journal of Biomedical Materials Research Part A **68**(3): 411-422.

Wittmer, C. R., J. A. Phelps, et al. (2007). "Fibronectin terminated multilayer films: protein adsorption and cell attachment studies." Biomaterials **28**(5): 851-860.

Wynne, K. J. and G. B. Street (1985). "Poly (pyrrol-2-ylium tosylate), electrochemical synthesis and physical and mechanical properties." Macromolecules **18**(12): 2361-2368.

Yekta-Fard, M. and A. Ponter (1992). "Factors affecting the wettability of polymer surfaces." Journal of adhesion science and technology **6**(2): 253-277.

Yuan, Y., S. Adeloju, et al. (1999). "In-situ electrochemical studies on the redox properties of polypyrrole in aqueous solutions." European polymer journal **35**(10): 1761-1772.

CHAPTER FOUR

Computational Modeling of Polypyrrole

4.1 INTRODUCTION

As discussed in Chapter 2, Polypyrrole (PPy) is made conductive by oxidizing some fraction of the pyrrole rings and conjugating them with anions, which greatly reduces the band gap in a process called doping. This phenomenon has been well described by several review papers (Waltman and Bargon 1986; Guimard, Gomez et al. 2007). Studies have shown that structural re-arrangement of PPy upon doping is not limited to the oxidized ring, but rather the charge spreads to neighboring rings (Ford, Duke et al. 1982). It has been shown that doped PPy performs well as a biomaterial or implant coating in the nervous system (Cui, Wiler et al. 2003). Its electrical conductivity makes it well suited to detect endogenous electrical signals from the nervous system or to deliver therapeutic electrical stimulation to the body. PPy's surface chemistry has also been modified to promote different biological responses by "tethering" relevant molecules or peptides to the material surface through covalent attachment (Lee, Lee et al. 2008), through inclusion as dopant ions (Cui, Lee et al. 2001), or through affinity binding (Sanghvi, Miller et al. 2005). Yet despite tremendous advances in the experimental characterization and synthesis of various types of doped PPy, much remains unknown about its nano-scale structure and surface properties.

A large number of experimental studies and several computational studies of PPy precede this work. The early computational work has mostly been performed with low-level *ab initio* methods. Ford et al. analyzed UV photoemission and optical absorption of polypyrrole using a semi-empirical CNDO/S3 method (Ford, Duke et al. 1982). It was suggested, based on the calculated density of valence states, that a photoexcited pyrrole

cation could span over 4-6 repeat units. Bredas et al. performed Hartree-Fock calculations of quaterpyrrole with and without Na+ dopants (n-type) using the STO-3G basis set (Bredas, Themans et al. 1983). Even though the small basis set was inadequate for accurate description of electronic structure, this work demonstrated an almost complete charge separation between the doping ions and pyrrole rings. It was also proposed that at high-doping levels, 33% and above, the bipolaron (two doping ions located adjacent to each other) was the dominant state (Bredas, Themans et al. 1983). The conformational energy of undoped pyrrole oligomers was previously investigated using Möller Plesset energy perturbation (MP2) and density functional theory (DFT) methods (Millefiori and Alparone 1998). That study found that the anti-gauche conformation was lowest in energy, and the rotational energy barrier of ca. 4 kcal/mol was reduced slightly from di- to tetrapyrrole. Thus undoped oligo or polypyrrole have non-planar structures and are likely to be rather flexible. Most recently, a quantum mechanics (QM) study of the equilibrium structures of oligomers up to 24 rings in length showed that higher doping ratios produce more planar chains (Dai and Blaisten-Barojas 2008). They also showed that explicitly including dopant ions in QM calculations with oxidized PPy chains increased the localization of positive charge near the doping sites. To ensure that this effect is captured in this study, all QM calculations of PPyCl explicitly included a dopant ion.

Molecular mechanical studies of PPy are scarce. An early molecular dynamics simulation of PPy in a crystalline formation was made using a generic polymer force field (Rabias, Hamerton et al. 1998). The OPLS-AA force field was reported for liquid pyrrole, but not the polymer form (McDonald and Jorgensen 1998). More recently Cascales and Otero performed dynamics simulations of Cl-doped films in an aqueous environment (Cascales, Fernandez et al. 2003; Cascales and Otero 2004; Cascales and

Otero 2005). However, the charges and the torsional parameters in the force field were not fully substantiated. The atomic charges from the results of CNDO quantum mechanical calculations were reduced by 50%, which made them very small in comparison to other studies. In addition, the exact approach used to generate the chain packing was unclear and the bulk properties were not fully validated. Finally, the fairly short simulations of 1-2 ns were likely insufficient. For efficient computation, a coarse-grain model of PPy was reported (Ruhle, Kirkpatrick et al. 2008). However, the fidelity of electrostatic representation is questionable in such a model. This coarse-grain study also reported QM results for the backbone conformational energy of oxidized and undoped PPy. The torsional energy barrier of oxidized PPy was estimated to be around 20 kcal/mol, but no attempt was made to fit a model to these results. No previously reported model of doped PPy has rigorously parameterized both the charge distribution and the conformational flexibility, which has limited the use of computational simulations to explore PPy based materials and their interactions with other molecules.

In this work, by using *ab initio* QM methods, we have investigated the charge distribution and backbone flexibility of PPy oligomers, with and without doping. On the basis of QM calculations, a new classical molecular mechanics potential has been developed and utilized in the molecular dynamics simulations of condensed-phase polypyrrole matrices. Both simulated annealing and potential scaling schemes were compared in producing representative PPy bulk structures. In addition to comparing the model's performance against gas phase QM structures and conformational energies, the bulk densities and atomic structures sampled from condensed-phase simulations using the force field have been directly compared to our experimental density and amorphous X-ray diffraction data. This potential was specifically developed to be compatible with the

OPLS-AA force field (Jorgensen, Maxwell et al. 1996; Kaminski, Friesner et al. 2001) for future study of protein interactions.

4.2 METHODS

Quantum mechanics calculations

QM geometry optimization calculations were performed on PPy trimers, pentamers, and septamers using the HF/6-31G* level basis set and the Gaussian03 software package (Frisch, Trucks et al. 2004). The final structures were used to define equilibrium bond lengths and angles. For doped PPy, a chloride ion was placed near an oxidized (polaron) polypyrrole oligomer. To ensure that the initial placement of the chloride ion was near the global minimum, we first performed twelve geometry optimizations of doped PPy trimers with the chloride ion in various positions around the chain. Eleven of the twelve simulations converged to the same location, whereas one stopped in a local minimum of much higher energy. After choosing the initial placement of the chloride ion, geometry optimization of trimers, pentamers, and septamers was performed as in the undoped case.

To quantify the backbone flexibility for both doped and undoped PPy, the backbone conformational energy profile was calculated by rotating and constraining the central bond of PPy quatermers in 15° increments from 0° to 360°. The geometry was optimized with the constraint in place using the HF/6-31G* basis set, and a single point calculation of the energy was performed using the MP2/6-311++G(2d,2p) basis set. Again, doped PPy quatermers were modeled with a single chloride doping ion.

Potential energy function and parameterization

Parameters for our molecular mechanics model were chosen to complement the OPLS-AA force field, which describes the potential energy with the following components:

$$E(r^N) = E_{bond} + E_{angle} + E_{dih} + E_{elec} + E_{VdW}$$

Equilibrium bond lengths and bond angles were computed by averaging the QM minimum energy structures of PPy trimers, pentamers, and septamers. The force constants for bond lengths and bond angles were transferred over from similar, existing aromatic parameters such as pyrrole in the OPLS-AA force field. Atomc partial charges for the electrostatic potential energy term were derived using the ChelpG method (Breneman and Wiberg 1990) on the HF/6-31G* QM minimum energy structures. The values were then rounded slightly up or down to ensure that the net charge of the model was exactly zero. Van der Waals parameters were also transferred from corresponding pyrrole atom types in the OPLS-AA force field. The dihedral angle energy contribution was calculated by comparing the QM conformational energy scan to equivalent MM structures using all energy terms except the dihedral angle term. The differences in energy between the QM and MM results were then fit to a Fourier series and an equivalent Ryckaert-Bellemans function (Ryckaert and Bellemans 1978) for the dihedral angle parameters. These two functional forms are used by TINKER (Ponder) and Gromacs (Hess, Kutzner et al. 2008), respectively.

Amorphous matrix formation

The developed force field has been incorporated into the TINKER (Ponder) and Gromacs (Hess, Kutzner et al. 2008) software packages. All molecular dynamics (MD) simulations were performed using Gromacs v4.0. Undoped, amorphous PPy matrices

were formed by placing 75 randomly-oriented PPy chains 4 nm apart in a 20 x 20 x 12 nm periodic box. The PPy chains were between 8 and 16 pyrrole rings in length to match experimental measurements (Bufon, Vollmer et al. 2005). The boxes were then slowly compressed under a pressure of 1000 bars using MD simulations with a constant number of atoms, controlled pressure, and controlled temperature (i.e., NPT ensemble) over approximately 40 ns. During the pressurization either simulated annealing or potential scaling was performed to sample the chain packing (see below). Once the box volume stabilized, the pressure was reduced to 1 bar and room temperature, and an additional 20 ns of NPT simulation data were recorded. The average density and radial distribution function for each of the matrices were measured from the last 15 ns of each simulation at increments of 10 ps.

A total of six *in silico* amorphous matrices were generated. For three matrices, thermal annealing up to 1000 K was performed during the high pressure phase of the simulation. For the other three matrices, a potential scaling approach was used in which van der Waals parameters were slowly turned on first, followed by electrostatic parameters. The scaling, or "turning on," of the parameters was done linearly at every step of a 10 ns simulation. For each matrix, the same initial, dilute structure was used, but velocities were assigned by using different seed values to ensure different trajectories. Doped PPy matrices were created by starting with a final undoped film structure, randomly placing chloride ions, and slowly mutating the force field parameters from undoped PPy to doped PPy over 10 ns. The van der Waals parameters of the chloride ions were initially turned off, which allowed the ions to move to energetically favorable locations as their van der Waals the charge parameters were slowly scaled up. We found this was most effective in distributing the ions across the matrix while promoting the "sharing" of ions between PPy chains.

Crystalline matrix formation

Two *in silico* crystalline matrices were created to examine how different chain packing affects bulk material properties. The first crystalline matrix was assembled by placing 75 chloride-doped PPy chains all parallel to each other in 5 rows of 15 pi-stacked chains. The chains were placed close together (i.e., pre-packed) in a 4.7 x 4.7 x 4.5 nm box. All the chains were 12 repeat units in length. The second crystalline matrix was also created from 5 rows of 15 pi-stacked chains, but the 2nd and 4th rows of chains were turned 90° so that they were perpendicular to their neighboring rows. After the initial structure was created, both matrices were pressurized as described in the amorphous matrix formation section and were thermally annealed at 800 K, although the backbone rearrangement from thermal annealing was limited by the already dense packing. As with the amorphous matrices, a 20 ns room temperature, atmospheric pressure simulation was performed, and data points were taken every 10 ps over the last 15 ns of the simulation.

When uniformly scaling the charge parameters up or down, additional 10 ns trajectories were simulated for each matrix starting from the final frame of the simulations described above. Data points were extracted every 10 ps for the last 5 ns of this trajectory. When testing previously published parameters, additional 20 ns trajectories were simulated, and data points were extracted every 10 ps for the last 15 ns.

Radial distribution functions

Radial distribution functions (RDFs) were created using the built-in "g_rdf" command in Gromacs 4. As in our density calculations, we used snapshots that were 10 ps apart over the last 15 ns of the simulation at room temperature and atmospheric

pressure. For the nitrogen-nitrogen RDF, all intramolecular nitrogen atoms were excluded so that only intermolecular distances are counted. Excluding intramolecular distances prevents the peaks associated with chain packing from being hidden by the peaks that are characteristic of single molecules.

X-ray diffraction experiment

A thick polypyrrole film was electrochemically synthesized onto indium tin oxide (ITO)-coated glass slides (Delta Technologies) from a solution of 0.1 M pyrrole (98%, Sigma-Aldrich) and 0.1 M NaCl (Sigma-Aldrich) in distilled, de-ionized (DDI) water. Pyrrole was purified using an aluminum oxide column before use. A 3-electrode configuration was used for electrochemical deposition with an oxidizing potential of 720 mV versus a saturated calomel electrode (SCE). The temperature of the solution was maintained near 273 K during synthesis by packing ice around the beaker. The surface area of the working electrode (the ITO slide) was controlled at 3 cm^2 and 6 Coulombs of charge were passed. The resulting film was gently rinsed with DDI water and dried overnight under vacuum. X-ray diffraction was performed on the dry film using a Phillips θ - 2θ Cu Kα powder diffractometer at the Texas Materials Institute on the University of Texas campus. The sample was scanned in increments of 0.02° with a dwell time of 10 seconds between 2θ angles of 3 and 40°, which corresponds to d spacing between 2.25 and 29.4 Angstroms using Bragg's law ($d=n\lambda/2\sin\theta$).

Flotation density

We performed flotation density experiments to determine the density of PPyCl based on methods previously published (Diaz 1981; Diaz and Hall 1983).

Dichloromethane (Sigma Aldrich) and chloroform (Sigma Aldrich) were used as the solvents. Using standard protocol, the composition of the solvents was adjusted until small PPyCl fragments remained suspended in solution. The 2 ml glass vials holding the samples were capped between adjustments to prevent evaporation, and the samples were allowed ample time to reach equilibrium. Density was calculated from the volumes of the solvents added and the known density values of the solvents provided by Sigma Aldrich. Most previously published values for the density of PPy were measured using the density of flotation method and range from 1.37 to 1.48 g/cm^3 (Diaz 1981; Diaz and Hall 1983); however, the closest dopant to chloride that was measured was perchlorate.

4.3 Results and Discussion

Gas phase properties from QM and MM calculations

As discussed in the introduction, several previous studies have examined the molecular and electronic structure of PPy oligomers using a range of *ab initio* theory (Ford, Duke et al. 1982; Bredas, Themans et al. 1983; Millefiori and Alparone 1998; Dai and Blaisten-Barojas 2008). Earlier works were limited by computational cost and used less accurate basis sets. More recent studies used high level, accurate basis sets to explore the equilibrium structure of polypyrrole at various chain lengths, but detailed information regarding electrostatics or backbone flexibility of the polymer is still lacking. In this study, we examined PPy oligomers up to septamers in both the undoped and chloride-doped (PPyCl) states. We have calculated the charge distribution of PPyCl to generate atomic charge parameters and have performed conformational energy scans of undoped and chloride-doped PPy quatermers to derive the torsion potentials. We have used these data to construct a new molecular mechanics force field for doped and undoped PPy.

From the minimum-energy structures of doped PPyCl pentamers and septamers, we found that at least 80% of the charge from oxidation is localized to the three PPy rings closest to the dopant ion. This finding, combined with the fact that many studies report PPy doping ratios (the ratio of dopant ions to PPy rings) around 33%, supports the approximation of confining charge spreading to the three rings closest to the dopant ion. Also, we found that averaging the charge equally across these three rings produced better fits to QM torsion data, simplified the number of parameters in the model, and probably more accurately reflects bulk environments where chloride ions are dispersed through the film, such as the lattice structures proposed by Veluri et al. (Veluri, Corish et al. 1995). As a practical matter, dividing the charge across three pyrrole rings required us to round the atomic charge of chloride from –1.000 to –0.999 to preserve charge neutrality in the system. The HF/6-31G* basis set, which we used for fitting partial charges, is known to overestimate the dipole moment (and thus the partial charges) for a molecule in gas phase. This overestimation, however, helps account for the increased polarization expected in condensed-phase simulations, since fixed-charge models do not explicitly include a polarization term (McDonald and Jorgensen 1998). The ChelpG charge fitting method was used largely for consistency with the OPLS-AA force field.

Bond lengths, bond angles, and partial charges obtained from QM calculations are shown graphically in **Figure 4.1** and also listed in **Table 4.1**. The alternating single bonds and double bonds within the ring structure are apparent, and the bond order switches across the PPy backbone upon doping. Bond lengths and angles for undoped PPy match closely with previously reported QM studies (Kofranek, Kovar et al. 1992). Atomic charges for undoped PPy have similar trends to *ab initio* QM charges reported for pyrrole (Andre, Vercauteren et al. 1984). The largest difference is the C¬α atom, which has a slightly negative atomic charge for pyrrole and has a positive atomic charge in

polypyrrole since the C-H bond is replaced with the backbone C-C bond. Previously reported atomic charges derived using the CNDO method (Cascales, Fernandez et al. 2003) are much smaller in magnitude. In the following section, we explore how scaling atomic charges to account for polarization affects the density of the bulk material.

The conformational energy profile of undoped PPy (**Figure 4.2a**) shows energy minima at the anti-gauche position around ±148°, with a relatively small torsional energy barrier of approximately 3 kcal/mol. A low energy barrier is consistent with the single carbon-carbon bond (i.e., longer bond length) that connects the pyrrole rings along the backbone of the polymer and again matches previously reported values for PPy (Kofranek, Kovar et al. 1992). Small energy wells in the *syn-gauche* configuration are also observed. The asymmetry in the conformational energy profile of PPy has not been reported before, since previous studies used bipyrrole rather than quaterpyrrole. From our observation, this asymmetry reflects the long-range electrostatic interaction between non-neighboring PPy rings such that they prefer to be out of plane from each other. Within the MM force field, the torsion energy parameter must be symmetrical, and asymmetry in the conformational energy profile must be captured in the other non-bonded energy terms. Since the torsion energy term also serves as an error function, using a PPy quatermer in the torsion energy scan allowed us to quantify how well we capture both torsional and non-bonded energy terms. Although using bipyrrole as the model system causes the conformational energy scan to always be symmetrical, it provides no information about the non-bonded contribution to conformational energy in a longer chain. For doped PPyCl (**Figure 4.2b**), QM results showed a much more rigid backbone, indicative of a double carbon-carbon bond across the backbone. One asymmetric high-energy data point at around -60° was observed in the QM results, which was the result of out-of-plane bending at one of the hydrogen atoms near the dopant ion. It is important to note that for

PPyCl QM calculations, we explicitly included a chloride dopant ion. The energy difference between the 0° and ±180° backbone conformations is primarily due to electrostatics. In bulk PPyCl, this bias is not present, since chloride ions would be present on both sides of the PPy chain.

Using the final force field parameters, we have minimized the energy of undoped and doped PPy quatermer structures and compared them to QM results. **Figure 4.3** shows the superimposed structures. The root-mean-square deviation (RMSD) between QM and MM structures (including hydrogen atoms) for undoped PPy was 0.145 Å, and for doped PPy was 0.043 Å, showing good agreement. As a note, the PPyCl quatermer shown in Figure 4.3b has a central backbone angle of 0° and is the lowest energy structure in Figure 4.2b. A torsion energy scan comparing QM results and the complete MM force field (Figure 4.2) also showed excellent agreement, with maximum error values less than 0.5 kcal/mol for undoped PPy. For PPyCl, a few data points had an error greater than 1 kcal/mol, but the shapes of the important energy wells were well reproduced. The 14.96 kcal/mol energy difference between the optimized structures at 0 and ±180° was captured by the MM force field within 0.4 kcal/mol without a torsion energy term (data not shown), which further demonstrates the adequacy of the electrostatic parameters to capture the non-bonded interactions.

Condensed-phase simulation of polypyrrole matrices

With the molecular mechanics model, we have performed condensed-phase simulations of PPyCl and undoped PPy in bulk environment. For PPy specifically, the average chain length for PPy electrochemically synthesized with low current density at lower temperatures is reported to be around 12 repeat units (Bufon, Vollmer et al. 2005),

which is short compared with other polymers. Experimental studies describing the chain packing of PPy are limited, but previous X-ray diffraction data show that PPy is mostly amorphous with small crystalline peaks detected under certain synthesis conditions (Dyreklev, Granstrom et al. 1996).

Amorphous polymer simulations pose challenges not present in most small molecule or biomolecule calculations. For polymers with flexible backbones, such as PPy, each chain has a large number of low-energy conformations. When expanded to a system of many chains, the result is a very large conformational space with a large number of structures that all represent the most probable structures. This is in contrast to protein folding problems, in which a single global minimum is expected (the native structure). To create the PPy polymer matrices, we sought to sufficiently sample the energy landscape to find representative low-energy structures that yielded consistent density values, torsion angle distributions, and radial distribution functions. Both molecular dynamics and Monte Carlo methods are suitable for this problem. We chose to use two molecular dynamics approaches: thermal annealing and potential scaling. Thermal annealing is a commonly used approach because of its simplicity and broad software support, but the potential scaling approach offered a greater level of control. As previous work has already mentioned (Tsujishita, Moriguchi et al. 1993), both approaches have mathematically equivalent effects on lowering the energy barrier to allow efficient sampling of the conformational space. The energy states of the system follow a Boltzmann distribution:

$$e^{-\frac{H}{k_B T}}$$

where H is the Hamiltonian of the system, k_B is the Boltzmann constant, and T is the temperature. Thermal annealing allows a molecular dynamics simulation to sample a broader ranger of states by "scaling up" the temperature. Potential scaling affects the

Boltzmann distribution very similarly by scaling down bonded and non-bonded interactions. Potential scaling offers the additional flexibility of scaling individual interaction separately. During PPy matrix formation, non-bonded electrostatic and van der Waals interactions caused PPy chains to quickly cluster. By turning off all non-bonded interactions and then slowly scaling up van der Waals energy terms followed by electrostatic parameters, the polymer had much more time to sample its conformational space. Neither potential scaling nor thermal annealing guarantees convergence to a global minimum, but they are helpful tools in overcoming local energy "traps." In the case of polymer formation, there is not a single global energy minimum, so the effectiveness of our sampling approach was measured by density, backbone angle distributions, and radial distribution functions rather than convergence to a specific native structure, as is usually the case in protein folding simulations.

For undoped PPy, we found that both thermal annealing and potential scaling produced PPy matrices of similar density, which suggests that both approaches are able to sufficiently sample the conformational space of the system. The final average density values, also shown in **Figure 4.4a**, were 1.230 g/cm^3 for thermally annealed, undoped PPy and 1.223 g/cm^3 for potential-scaled, undoped PPy. These density values are in good agreement with the reported density of undoped PPy of 1.25 g/cm^3 (Rabias, Hamerton et al. 1998). The probability distribution of the backbone torsion angles (Figure 4.2c) of the relaxed matrices were similar between the two approaches, with the annealing method resulting in a slightly higher percentage of torsion angles in the higher energy well around +/- 45°. In both cases, however, the backbone torsion angle probability distribution agrees with the conformational energy scan (Figure 4.2a), which suggests that the matrix was able to form a relaxed, condensed phase structure. As discussed in the Methods section, the conformational energy scan was created by constraining the

torsion angle of the central C–C bond in a pyrrole quatermer in 15° increments and calculating the system energy. The backbone torsion angle probability distribution describes the bulk, packed state of the matrix built using the molecular mechanics model. Agreement between the two, where low energy states in the quantum mechanics calculations are more highly represented in the molecular mechanics simulation, demonstrates that the molecular mechanics parameters accurately capture the quantum mechanics behavior.

When attempting to construct doped PPy matrices, thermal annealing did not effectively sample the energy landscape, because the intermolecular forces between PPyCl chains were too strong. Initially, we attempted to form matrices the same way we formed undoped PPy matrices: starting with the full system in gas phase and slowly condensing the system at high temperature and high pressure. In these simulations, the charged PPy chains quickly wrapped around chloride ions and then aggregated together, forming stable but non-physical structures. Even at 1000° Kelvin, the chains remained clustered and wrapped. Using the potential scaling method, we were able to initially turn off the electrostatic parameters for the system and slowly increase them over time. This solved the aggregation problem, but we found that the packing was still dominated by individual chains wrapped around their chloride ions. In the end, we found that by starting with the undoped PPy matrix, adding "ghost" chloride ions, and slowly scaling the parameters from undoped PPy to PPyCl, we were able to produce amorphous matrices with a proper backbone torsion angle distribution and chloride ions shared between chains. This approach is similar to free energy perturbation calculations, where a molecule is very slowly mutated to a slightly different molecule, and the system is given time to adapt and relax (Jorgensen and Ravimohan 1985). This approach, however, has the limitation that, when applied to a densely packed system, large scale backbone re-

arrangement is mostly prohibited. The torsion angle distribution for PPyCl (Figure 4.2d) agrees well with the conformational energy profile shown in Figure 4.2b when the electrostatic contributions are taken into account. As mentioned in the discussion of the gas phase QM results, the ~15 kcal/mol difference between 0 and ±180° in the conformational energy profile is the result of explicitly including a chloride ion on one side of the PPy chain. An equal probability of 0 and ±180° conformations was expected and observed in bulk, amorphous PPyCl.

Upon doping PPy, we found that the *in silico* matrix expanded slightly to give a lower average density value of 1.146 g/cm^3. Previous computational studies of PPy also report a swelling or decrease in density upon doping (Cascales and Otero 2005). These density results fall somewhat below experimental measurements. Previously report experimental density values for doped PPy films using the flotation method range from 1.37 to 1.48 g/cm^3 (Diaz 1981; Diaz and Hall 1983), but given the sensitivity of PPy's properties to synthesis conditions and dopant selection (Dyreklev, Granstrom et al. 1996; Fonner, Forciniti et al. 2008), relevant values may also fall outside this range. In the current study, we have performed our own density of flotation experiments on PPyCl and obtained a density of 1.46 g/cm^3. For *in silico* PPy matrices, low density values can be caused by partial charges that do not capture the polarization effects of the local environment or by non-optimal chain packing, so we have further examined the effects on bulk density of scaling atomic charges and different chain packing.

Partial charge calculations from gas phase QM calculations do not account for polarization of the molecules in the bulk phase. Other molecules in the OPLS force field use gas phase QM as a starting point (Jorgensen and Gao 1986) and uniformly scale the magnitude if necessary to match experimental data (McDonald and Jorgensen 1998) for liquid simulations. Although charge fitting using the HF/6-31G* basis set slightly

overestimates the dipole moment in pyrrole monomers, this overestimation is often a closer approximation for molecules in an aqueous environment (McDonald and Jorgensen 1998). Nevertheless, the lack of transferability of fixed-charge models across different environments makes it a challenge to calculate electrostatic parameters. To investigate the effect of atomic charges on density, we scaled the partial charges of doped PPy final structures to 80%, 90%, and 110% of the values reported in Figure 4.1. The results are shown in **Figure 4.4b**. The results show that scaling up the atomic charge leads to an increased density of PPyCl. This was not expected, since a previous theoretical study with PPyCl by Cascales et al. used very low partial charge values but reported final density values around 1.32 g/cm^3 (Cascales and Otero 2005). We have applied the charge and united-atom van der Waals parameters used by Cascales et al. in our protocol, but the resulting density values we calculated were only 1.12 g/cm^3 (also shown in Figure 4b). Switching from our all-atom van der Waals parameters to the united-atom parameters without changing the atomic charges led to a negligible increase in the PPyCl density of 0.03 g/cm^3. The doping ratio we used (~30% in this study vs. ~10% previously) could also attribute some to the difference. Another difference between this and the previous study may lie in chain packing. In the previous study, Cascales et al. placed PPy chains in a packed configuration and allowed the system to relax. In this work, we started with a very dilute system of PPy chains and performed molecular dynamics simulations to relax and sample the chain packing. The current approach is more rigorous, as the results are independent of the initial conditions, but there is no guarantee that the level of crystallinity matches the properties of experimentally-fabricated PPyCl. It is likely that PPyCl contains small crystalline regions at the microscopic level as a result of the rigid backbone. To test the effect of crystallinity on bulk density, we performed additional simulations with crystalline chain packing (shown

in **Figure 4.4c**) and observed a significant increase in the density of the matrix to over 1.3 g/cm^3. This shows that chain packing greatly affects density, and experimentally-measured densities for PPy may exhibit large variations because different synthesis conditions result in different levels of crystallinity (Dyreklev, Granstrom et al. 1996).

Simulations provide a wealth of information about atomic structure and molecular interactions that is not easily gathered experimentally. In addition to comparing the bulk density, we have also compared the radial distribution functions (RDF) of our *in silico* matrices to experimental x-ray diffraction data we gathered for PPyCl. Interchain radial distribution functions for PPyCl are shown in **Figure 4.5**. For the nitrogen-chloride RDF, the sharp peak at 0.32 nm in both amorphous and crystalline PPyCl shows a stable, well-defined electrostatic interaction between chloride and oxidized PPy. The nitrogen-nitrogen RDF, which does not include intramolecular nitrogen distances, has a shoulder around 0.4 nm and rounded peaks at 0.61 nm and 0.81 nm for amorphous PPyCl. In contrast, crystalline PPyCl has pronounced peaks at 0.35 nm and 0.506 nm. From the simulated structures, we observed that PPy chains in a π-stacked configuration were between 0.33 and 0.43 nm apart, which accounts for the shoulder observed at 0.4 nm in amorphous PPyCl and the peak at 0.35 in crystalline PPyCl. The distances between nitrogen atoms of different chains surrounding the same chloride ion are between 0.61 and 0.66, corresponding to the first rounded peak in the amorphous RDF.

We performed amorphous X-ray diffraction experiments on electrochemically synthesized thick PPyCl films to examine peaks associated with chain packing. As shown in **Figure 4.6**, the reflections associated with average chain packing distance are concentrated around a 2θ angle of 27°, which may correspond to the N-N separation of pi-stacked PPy chains observed in the simulated RDFs (Figure 4.5). Previous studies using perchlorate-doped PPy report chain packing 2θ angles of 22° (0.40 nm) for an

amorphous PPy film and 24° (0.37 nm) for a slightly more crystalline PPy film, as controlled by synthesis conditions (Dyreklev, Granstrom et al. 1996). These previously reported distances are in agreement with the N-N separation in our simulated amorphous PPyCl matrix (Figure 4.5a). In our X-ray diffractogram, we also observed peaks at 2θ angles of 29.5° and 32° and a small peak at 17.5°. The peak at 32° may indicate the presence of residual NaCl crystals on the surface of the film. Even after rinsing, we have occasionally observed some residual salt crystals on the surface of our PPyCl films. The peak at 29.5° corresponds to an interatomic distance of 0.30 nm and the small peak at 17.5° corresponds to 0.506 nm. Given that our simulated films had slightly lower densities, the experimentally observed peak at 0.30 nm may be related to the average N-Cl distance of 3.2 nm in our simulated films. The small X-ray diffraction peak at 0.506 nm matches perfectly with the second peak of the N-N RDF for our simulated crystal structure.

4.4 CONCLUSIONS

We analyzed polypyrrole's structure, charge distribution, and backbone flexibility in both the doped and undoped state using quantum mechanics calculations. We found that over 80% of the net positive charge of oxidized PPy stays within the three rings closest to the dopant ion. We also observed a dramatic increase in backbone stiffness upon doping. From these QM calculations, we have parameterized a fixed-charge force field suitable for studying the properties of bulk PPy. We examined the performance of this model by comparing the minimum energy structure with quantum mechanics results, by comparing the backbone torsion energy scan with quantum mechanics results, and by comparing bulk density measurements and RDFs to our own experimental data and

previously reported data from flotation density and X-ray diffraction. The force field performed well when compared to QM results. Our simulated density values were slightly below reported experimental values, but after attempting to repeat the work with a previously reported model, we conclude that the force field itself performs well and that there is room for improvement in chain packing approaches. We believe this work presents the most rigorously parameterized and accurate force field to date, especially with respect to the electrostatics and torsion potential. As future work, the parameterization and incorporation of bipolarons would strengthen the model and may also improve the re-creation of bulk material properties. Polypyrrole has many promising applications in biomedical and electronic fields, and an accurate computational model of this material creates opportunities for us and others to investigate its behavior and interactions with other molecules.

Table 4.1 – Parameters for undoped PPy and doped PPyCl.

Undoped Polypyrrole					Doped Polypyrrole				
Atom Type		**Charge (e-)**	**σ (Å)**	**ε(kcal/mol)**	**Atom Type**		**Charge (e-)**	**σ (Å)**	**ε(kcal/mol)**
NA	opls_542	-0.386	3.250	0.170	NA	opls_542	-0.486	3.250	0.170
CW	opls_543	0.107	3.550	0.070	CW	opls_543	0.269	3.550	0.070
CS	opls_544	-0.215	3.550	0.070	CS	opls_544	-0.195	3.550	0.070
H	opls_545	0.320	0.000	0.000	H	opls_545	0.363	0.000	0.000
HA	opls_547	0.141	2.420	0.030	HA	opls_547	0.154	2.420	0.030
					Cl-	opls_401	-0.999	4.417	0.118

Bonds	**b_o(Å)**	**k_b(kcal/mol/Å^2)**
NA-H	0.9937	434
NA-CW	1.3657	337
CW-CW	1.4567	469
CW-CS	1.3644	469
CS-CS	1.4223	469
CS-HA	1.0715	367

Bonds	**b_o(Å)**	**k_b(kcal/mol/Å^2)**
NA-H	1.0280	434
NA-CW	1.3526	337
CW-CW	1.4127	469
CW-CS	1.4197	469
CS-CS	1.3660	469
CS-HA	1.0700	367

Angles	**θ_0(degrees)**	**k_θ(kcal/mol/rad^2)**
H-NA-CW	124.42	38
NA-CW-CW	121.34	63
NA-CW-CS	107.49	63
NA-CW-HA	121.04	35
CW-NA-CW	110.12	63
CW-CW-CS	131.17	63
CW-CS-CS	107.44	63
CW-CS-HA	125.93	35
CS-CW-HA	130.85	35
CS-CS-HA	126.54	35

Angles	**θ_0(degrees)**	**k_θ(kcal/mol/rad^2)**
H-NA-CW	124.86	38
NA-CW-CW	124.09	63
NA-CW-CS	107.38	63
NA-CW-HA	121.04	35
CW-NA-CW	110.28	63
CW-CW-CS	128.54	63
CW-CS-CS	107.49	63
CW-CS-HA	125.82	35
CS-CW-HA	130.85	35
CS-CS-HA	126.68	35

N-C-C-N Torsion Parameter		**(kcal/mol)**	
Ryckaert-Bellemans function		Fourier series	
C0	2.797	V0	0.000
C1	-0.718	V1	1.093
C2	-4.557	V2	2.307
C3	0.228	V3	-0.114
C4	2.250	V4	-0.563

N-C-C-N Torsion Parameter		**(kcal/mol)**	
Ryckaert-Bellemans function		Fourier series	
C0	5.042	V0	0.000
C1	2.466	V1	-1.233
C2	15.57	V2	5.042
C3	-2.466	V3	1.233
C4	-20.612	V4	5.153

*Ryckaert-Bellemans (R-B) function is used in Gromacs (Hess, Kutzner et al. 2008) and Fourier series is used in TINKER (Ponder). All values are shown in units of kcal/mol. The R-B parameters listed use the Gromacs convention where 0° is the trans configuration (i.e., the "polymer convention"). The Fourier series parameters listed use the Tinker convention where 0° is the cis configuration.

4.5 FIGURES

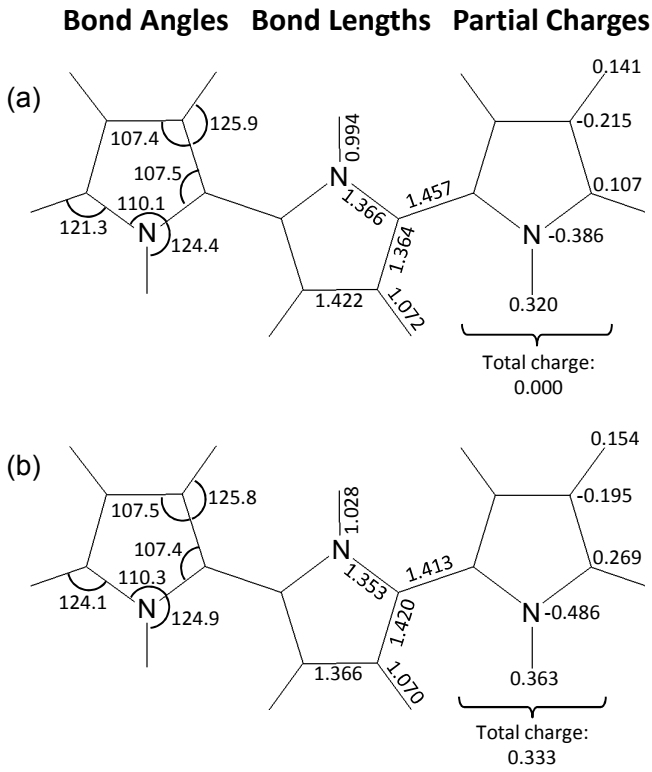

Figure 4.1 – Bond length, bond angle, and partial charges for (a) undoped and (b) doped PPy.

The minimized structure for (a) undoped and (b) doped PPy provides the equilibrium values for bond length and bond angles as well as the partial charges of the atoms. Although displayed across three PPy rings for clarity, all parameters are for a single PPy ring.

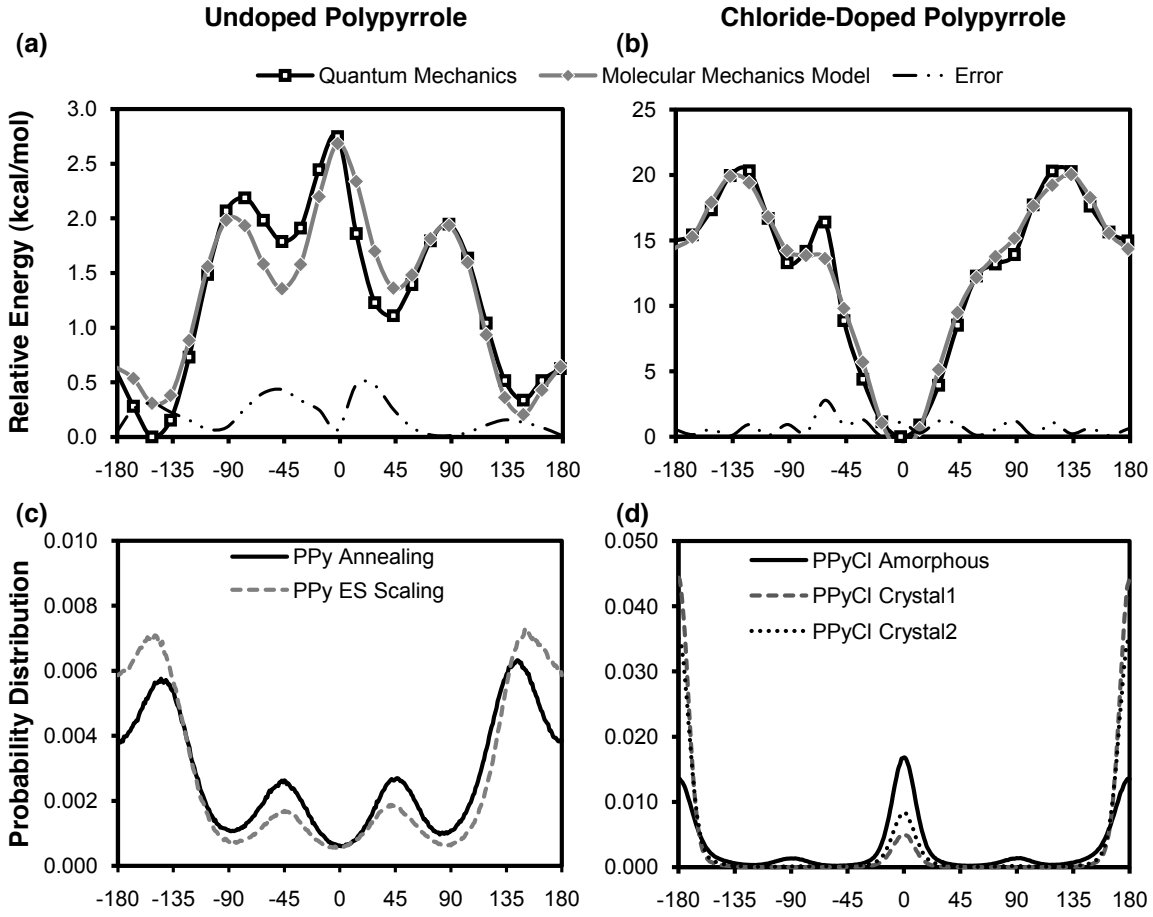

Figure 4.2 – Conformational energy profile and probability distribution for (a, c) undoped PPy and (b, d) doped PPyCl.

Torsion angle is defined such that zero is the *cis* configuration with the nitrogens on the same side. In a relaxed state, (a) undoped PPy does not adopt a planar backbone conformation, but rather an *anti* configuration at ±148°. (b) PPyCl, however, has a very rigid backbone with minima at 0° and 180°. Note that the 15 kcal/mol energy difference between 0° and 180° for PPyCl is from electrostatic interactions with the dopant, not from a torsion contribution. As shown in (d), bulk amorphous PPyCl adopts a roughly equal torsion angle distribution between *cis* and *trans* conformations. The torsional energy barrier of doped PPy is an order of magnitude greater than that of undoped PPy. For comparison, the condensed phase backbone distribution (c, d), which should be inversely proportional to the torsion energy, is also shown here. Potential scaling and thermal annealing approaches yielded similar backbone distributions for undoped PPy. For PPyCl, pre-packed crystals were mostly constrained to the *trans* configuration.

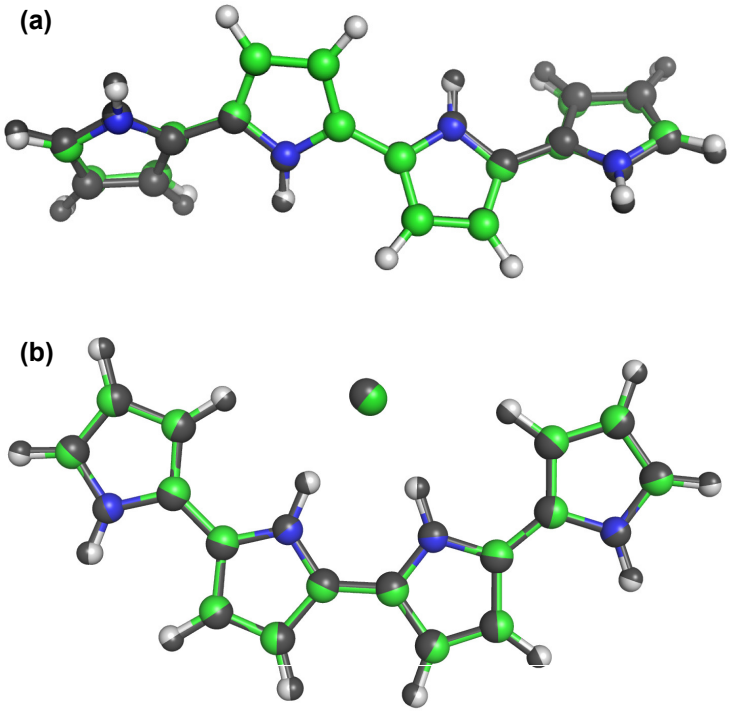

Figure 4.3 – Minimum energy structures of PPy quatermers.

Quantum mechanics (QM) minimum energy structures are shown in dark gray. Molecular mechanics (MM) structures are in color (available online). RMSD of undoped PPy structures is 0.145 Å, and RMSD of PPyCl is 0.043 Å. Tight agreement between QM and MM minimum energy structures serves as one validation of the MM model.

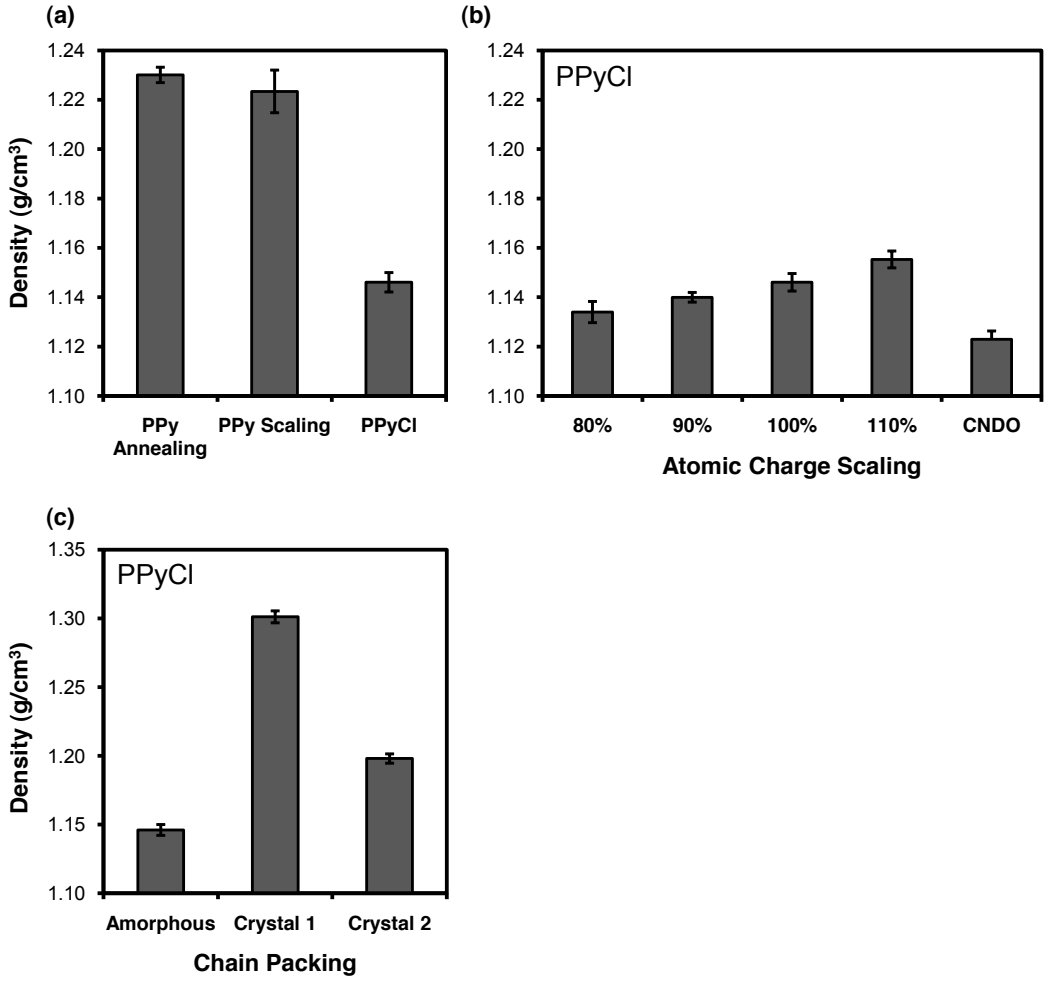

Figure 4.4 – Density measurements for undoped and doped PPy.

(a) Average density measurements (n=3 matrices, 1500 snapshots each) for undoped PPy matrices generated by thermal annealing, undoped PPy matrices generated by potential scaling, and PPyCl matrices made through a mutation process. Thermal annealing and potential scaling approaches consistently produced matrices of similar density. For PPyCl, we observed a swelling in the material that caused a slight decrease in density. (b) Average density measurements (n=3 matrices, 500 snapshots each) for PPyCl where electrostatic charge parameters have been scaled up or down. CNDO charges taken from Cascales *et al*. (Cascales, Fernandez et al. 2003) were used for comparison. For fixed charge models, scaling charge parameters is one way to account for polarization. We found that scaling the electrostatics of PPyCl has a non-trivial effect on polymer density, with larger charge parameters producing denser films. (c) Average density for crystalline PPyCl (n=1 matrix, 1500 snapshots) demonstrates that chain packing greatly affects bulk density.

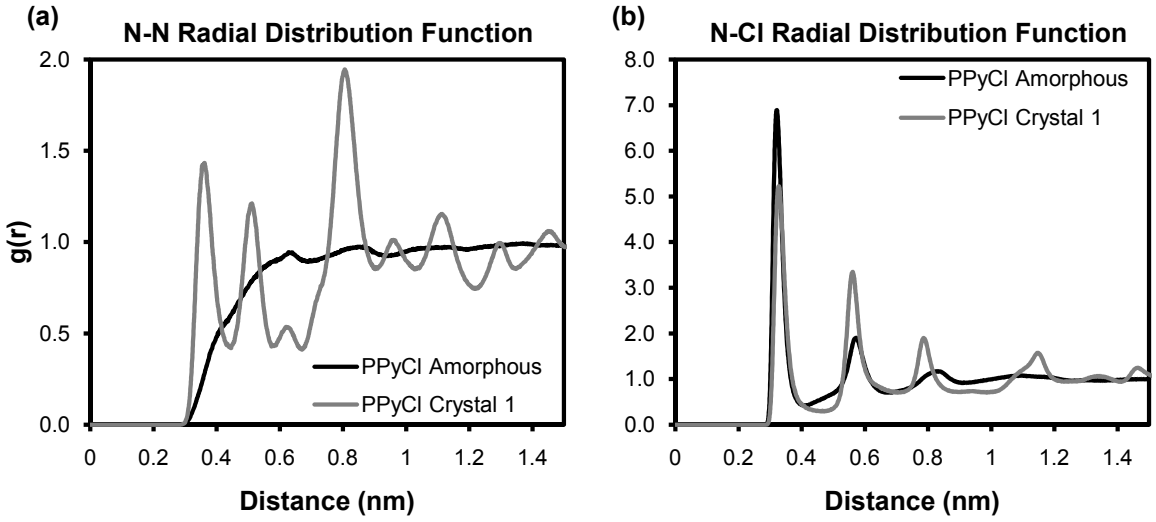

Figure 4.5 – Radial distribution functions for PPyCl.

Normalized radial distribution functions for (a) nitrogen-nitrogen and (b) nitrogen-chloride. Nitrogens within the same molecule were excluded. (a) The peak at 0.35 nm for crystalline PPyCl shows an increase in pi stacking versus amorphous PPyCl. (b) In both crystalline and amorphous PPyCl, dopant ions are consistently 0.32 nm from the nitrogen atom with which they interact.

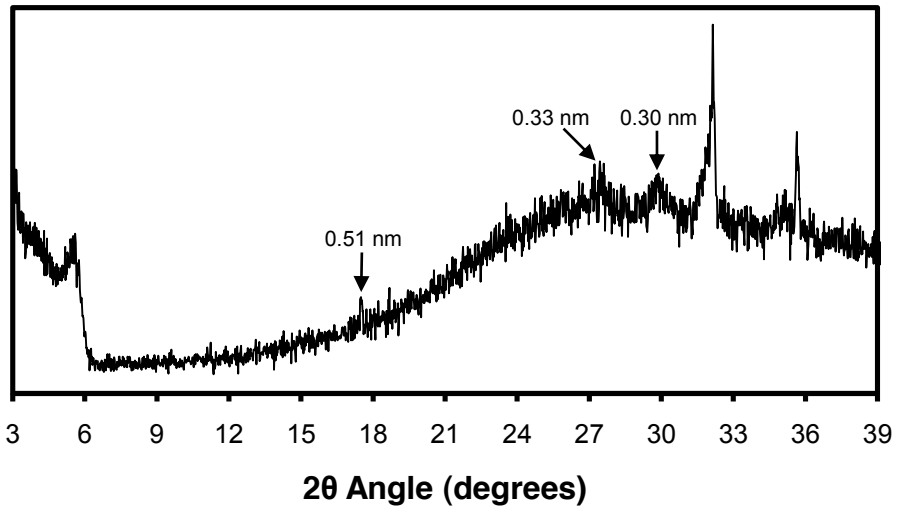

Figure 4.6 – X-ray diffractogram of electrochemically-synthesized PPyCl.

Experimentally-synthesized PPyCl films were analyzed for comparison with computationally-generated PPyCl matrices. The broad rounded peak associated with chain packing centered around a 2θ angle of 27°, which corresponds to a d-spacing of 0.33 nm. The sharp peak around 32° likely represents residual NaCl crystals on the surface of the film that were not fully removed from rinsing.

4.6 REFERENCES

Andre, J. M., D. P. Vercauteren, et al. (1984). "Electronic properties of polypyrrole: An ab initio Hartree–Fock study." The Journal of Chemical Physics **80**: 5643.

Bredas, J. L., B. Themans, et al. (1983). "Bipolarons in Polypyrrole Chains." Physical Review B **27**(12): 7827-7830.

Breneman, C. M. and K. B. Wiberg (1990). "Determining atom-centered monopoles from molecular electrostatic potentials. The need for high sampling density in formamide conformational analysis." Journal of Computational Chemistry **11**(3): 361-373.

Bufon, C. C. B., J. Vollmer, et al. (2005). "Relationship between chain length, disorder, and resistivity in polypyrrole films." J. Phys. Chem. B **109**(41): 19191-19199.

Cascales, J. J. L., A. J. Fernandez, et al. (2003). "Characterization of the reduced and oxidized polypyrrole/water interface: A molecular dynamics simulation study." Journal of Physical Chemistry B **107**(35): 9339-9343.

Cascales, J. J. L. and T. E. Otero (2005). "Molecular dynamics simulations of the orientation and reorientational dynamics of water and polypyrrole rings as a function of the oxidation state of the polymer." Macromolecular Theory and Simulations **14**(1): 40-48.

Cascales, J. J. L. and T. F. Otero (2004). "Molecular dynamic simulation of the hydration and diffusion of chloride ions from bulk water to polypyrrole matrix." Journal of Chemical Physics **120**(4): 1951-1957.

Cui, X., V. A. Lee, et al. (2001). "Surface modification of neural recording electrodes with conducting polymer/biomolecule blends." Journal of biomedical materials research **56**(2): 261-272.

Cui, X., J. Wiler, et al. (2003). "In vivo studies of polypyrrole/peptide coated neural probes." Biomaterials **24**(5): 777-787.

Dai, Y. and E. Blaisten-Barojas (2008). "Energetics, structure, and charge distribution of reduced and oxidized n-pyrrole oligomers: A density functional approach." Journal of Chemical Physics **129**(16): 8.

Diaz, A. (1981). "Electrochemical preparation and characterization of conducting polymers." Chemica Scripta **17**: 145-148.

Diaz, A. F. and B. Hall (1983). "Mechanical-Properties of Electrochemically Prepared Polypyrrole Films." Ibm Journal of Research and Development **27**(4): 342-347.

Dyreklev, P., M. Granstrom, et al. (1996). "The influence of polymerization rate on conductivity and crystallinity of electropolymerized polypyrrole." Polymer **37**(13): 2609-2613.

Fonner, J. M., L. Forciniti, et al. (2008). "Biocompatibility implications of polypyrrole synthesis techniques." Biomedical Materials **3**(3): -.

Ford, W. K., C. B. Duke, et al. (1982). "Electronic-Structure of Polypyrrole and Oligomers of Pyrrole." Journal of Chemical Physics **77**(10): 5030-5039.

Frisch, M. J., G. W. Trucks, et al. (2004). "Gaussian 03, Revision C. 02." Gaussian Inc., Wallingford, CT.

Guimard, N. K., N. Gomez, et al. (2007). "Conducting polymers in biomedical engineering." Progress in Polymer Science **32**(8-9): 876-921.

Hess, B., C. Kutzner, et al. (2008). "Gromacs 4: Algorithms for highly efficient, load-balanced, and scalable molecular simulation." J. Chem. Theory Comput **4**(3): 435-447.

Jorgensen, W. L. and J. Gao (1986). "Monte Carlo simulations of the hydration of ammonium and carboxylate ions." The Journal of Physical Chemistry **90**(10): 2174-2182.

Jorgensen, W. L., D. S. Maxwell, et al. (1996). "Development and testing of the OPLS all-atom force field on conformational energetics and properties of organic liquids." Journal of the American Chemical Society **118**(45): 11225-11236.

Jorgensen, W. L. and C. Ravimohan (1985). "Monte Carlo Simulation of Differences in Free Energies of Hydration." Journal of Chemical Physics **83**: 3050-3054.

Kaminski, G. A., R. A. Friesner, et al. (2001). "Evaluation and Reparametrization of the OPLS-AA Force Field for Proteins via Comparison with Accurate Quantum Chemical Calculations on Peptides†." J. Phys. Chem. B **105**(28): 6474-6487.

Kofranek, M., T. Kovar, et al. (1992). "Ab initio studies on heterocyclic conjugated polymers: Structure and vibrational spectra of pyrrole, oligopyrroles, and polypyrrole." The Journal of chemical physics **96**(6): 4464-4473.

Lee, J. Y., J. W. Lee, et al. (2008). "Neuroactive conducting scaffolds: nerve growth factor conjugation on active ester-functionalized polypyrrole." Journal of The Royal Society Interface.

McDonald, N. A. and W. L. Jorgensen (1998). "Development of an all-atom force field for heterocycles. Properties of liquid pyrrole, furan, diazoles, and oxazoles." J. Phys. Chem. B **102**(41): 8049-8059.

Millefiori, S. and A. Alparone (1998). "Theoretical study of the structure and torsional potential of pyrrole oligomers." Journal of the Chemical Society-Faraday Transactions **94**(1): 25-32.

Ponder, J. W. "TINKER molecular Modeling package." Washington University Medical School. Available at http://dasher.wustl.edu/tinker.

Rabias, I., I. Hamerton, et al. (1998). "Theoretical studies of conducting polymers based on substituted polypyrroles." Computational and Theoretical Polymer Science **8**(3-4): 265-271.

Ruhle, V., J. Kirkpatrick, et al. (2008). "Coarse-grained modelling of polypyrrole morphologies." Physica Status Solidi B-Basic Solid State Physics **245**(5): 844-848.

Ryckaert, J. P. and A. Bellemans (1978). "Molecular dynamics of liquid alkanes." Faraday Discussions of the Chemical Society **66**: 95-106.

Sanghvi, A. B., K. P. H. Miller, et al. (2005). "Biomaterials functionalization using a novel peptide that selectively binds to a conducting polymer." Nature Materials **4**(6): 496-502.

Tsujishita, H., I. Moriguchi, et al. (1993). "Potential-scaled molecular dynamics and potential annealing: effective conformational search techniques for biomolecules." Journal of physical chemistry(1952) **97**(17): 4416-4420.

Veluri, K., J. Corish, et al. (1995). "A lattice simulation investigation of the migration of chloride ions in doped polypyrrole and polythiophene." Journal of Molecular Structure: THEOCHEM **334**(2-3): 109-120.

Waltman, R. J. and J. Bargon (1986). "Electrically conducting polymers: a review of the electropolymerization reaction, of the effects of chemical structure on polymer film properties, and of applications towards technology." Canadian Journal of Chemistry **64**(1): 76-95.

CHAPTER FIVE

Polypyrrole Binding Interactions

5.1 INTRODUCTION

Characterizing binding interactions has long been a central component of drug development and refinement, and numerous experimental and computational methods have become standard within the field. The binding pocket is usually well defined, and the ligands whose binding strengths are to be measured are fairly small and generally have few degrees of freedom. Crystal structures or NMR data are able to elucidate the bound structure of the protein and ligand, and high throughput assays or computational calculations are able to estimate the binding free energy. The biomaterials field, however, has historically operated with less precision when analyzing surface interactions. For chronic implants, *in vivo* biocompatibility tests are performed to ensure that the body is able to encapsulate the implant without chronically triggering the immune system, but information about the surface interactions of specific biomolecules is usually not required. Consequently, tools and protocols deemed standard in the drug industry have not been adapted to the biomaterials world, and our understanding of how peptides interact and proteins denature on synthetic material surfaces has grown slowly.

For implant applications that require more controlled surface chemistry and better tissue integration, multiple groups have explored the design concept of incorporating peptide based "interfacial biomaterials" in recent years (Meyers, Khoo et al. 2009). The idea is to search for a peptide sequence that preferentially binds to the surface of a biomaterial that has good bulk properties put insufficient surface properties to serve in a specific implant application. For example, titanium's strength and chemical stability make it an exceptional bulk material for orthopedic applications, but its "bioinert" surface

properties cause the body to encapsulate the material in a mostly avascular fibrous capsule that can allow biofouling to occur (Liu, Chu et al. 2004). Within the context of our group's research, polypyrrole is conducting polymer with good conductivity and good surface topography that works well as a low impedance coating on electrodes or as a free-standing scaffold for neural applications, but it lacks the surface functional groups that can send chemical cues to the host tissue. Attempts to modify the chemistry of the polymer to covalently conjugate chemical cues to the surface lead to a dramatic decrease in the electrical conductivity of the material (Lee, Serna et al. 2006). An interfacial biomaterial such as a layer of surface-bound peptides has the potential to incorporate chemical cues on the surface of the material without altering its favorable bulk properties (Sanghvi, Miller et al. 2005). The interfacial biomaterial could serve to direct the host response toward regenerative behavior by incorporating biomolecules such as growth factors while at the same time inhibit the foreign body response of the immune system by masking the synthetic bulk material with naturally occurring biomolecules.

Before we can create better, more bioactive implants using interfacial biomaterials, we must invest in better methods, and more financially accessible methods, to quantify and refine affinity-binding molecules. Experimentally, phage display provides a reliable technique for generating lead peptide sequences. For sequences larger than 6 or 7 amino acids in length, however, phage display libraries cannot include all the vast number of possible combinations of peptide sequences possible. Thus, for longer peptide sequences, results from phage display are most likely not the best possible sequences, just as initial drug candidates are usually not the best binding molecules. Better computational methods to provide mechanistic insight into why a particular sequence binds and to predict variants that may bind more tightly would be of great

utility in making interfacial biomaterials more accessible and more transferrable to clinical implant applications.

Previous Work on Affinity Peptides for Polypyrrole

Sangvi, et. al. used phage display to screen a library of 12-mer peptides for affinity-binding peptides for chloride doped polypyrrole (Sanghvi, Miller et al. 2005). They found several sequences that adhered to polypyrrole, the strongest binder being the T59 peptide with a sequence of THRTSTLDTFVI. The phage library used had a diversity of 2.7×10^{9}, but given that a 12 amino acid peptide sequence has 20^{12} possibilities, the library contained less than a thousandth of one percent of all possible sequences. Therefore, although phage display is exceptionally effective at finding affinity binding peptide sequences, as has been demonstrated by others for materials such as polystyrene (Meyers, Khoo et al. 2009), titanium (Meyers, Hamilton et al. 2007), and polyglycolic acid (Huang, Zauscher et al. 2010), it is highly probable that there are other sequences with better binding affinity. In the drug industry, after a lead molecule is discovered, an extensive process of refining the compound to improve its binding begins. In the same way, we propose that binding peptides would be much more effective if there was a way to refine the sequence beyond the initial phage display result.

We have used computational simulations as the next step in refining peptide sequences. One of the weaknesses of the phage display technique is that, while it does identify binding peptide sequences, it gives no information on the bound structure or binding mechanism that drives the interaction. Experimentally, it is possible to look at the sequence, guess what could be happening, and then synthesize peptide variants and carefully use them in binding assays to gain more insight into the relative importance of different amino acids. This was done previously for the T59 peptide, in which five

different variants were explored (Sanghvi, Miller et al. 2005). From the different variants, the authors concluded that the aspartic acid residue was critical in the binding interaction, but moving forward in a refinement process with only that information would not be possible. Additionally, the expense of experimentally synthesizing specific peptide sequences limits most investigations to only a few sequences. To obtain more information on the mechanism of binding or to explore a broad set of variants, a different approach must be used. We propose that computational tools could be well suited to this task.

5.2 METHODS

All molecular dynamics simulations used the Gromacs 4.0 software package for the simulation engine. Calculations involving implicit solvent used Gromacs 4.5 and the generalized Born method (Still, Tempczyk et al. 1990) where Born radii were calculated using the OBC method (Onufriev, Bashford et al. 2004; Mongan, Simmerling et al. 2007). The OPLS-AA force field was used to represent amino acids (Kaminski, Friesner et al. 2001), and the TIP4P water model was used for all simulations containing explicit water molecules (Jorgensen, Chandrasekhar et al. 1983). The model parameters for polypyrrole come from previously published work within our lab (Fonner, Schmidt et al.). The time step for all simulations was 2 femtoseconds, with hydrogen bonds restrained using the LINCS algorithm.

Polypyrrole Matrix Formation

To model the surface of PPy, both amorphous and ordered PPy matrices were studied *in silico*. In general, our previously reported method was used to form these matrices with differences only in the box dimensions and the total number of PPy chains (Fonner, Schmidt et al.). Amorphous films were formed by placing randomly oriented

PPy chains in a dilute box. The number of chains and box size were chosen to create a matrix with a surface of roughly 7 nm × 7 nm and between 2.5 and 3 nm in depth. A minimum thickness of 2.5 nm was chosen based on previous work in the Latour lab that showed 25 Å of water sufficiently screened electrostatic interactions between ions in solution and a charged surface (Collier, Vellore et al. 2009). Controlled pressure, controlled temperature (NPT) simulations were performed on these dilute systems for 10ns at 1000 bars of pressure with a temperature of 1000K to allow the polymer chains to freely sample different conformations before condensing into a packed structure. An isotropic Berendsen barostat with a high time constant (τ_P = 200ps) was used to slowly decrease the box size and compress the matrix. As previously shown, these structures have consistent density, radial distribution functions, and torsion angle profiles, which indicate that the PPy matrices reach a converged, relaxed state. Ordered PPy chains were created by placing PPy chains into a pre-packed, aligned structure. Again, a high temperature, high pressure NPT simulation was used to give the packed structures the opportunity to sample within the local, packed frame. In all cases, after the high temperature, high pressure simulation, the matrices were slowly cooled to 298K over 10ns, and an additional 10ns of simulation at 1 atmosphere and 298K was performed to obtain statistics on the final, relaxed structure of the polymer matrices. In the final structures, the amorphous PPy matrix contained 144cd 3 PPy chains in a 7.46 nm × 7.46 nm × 2.79 nm box, and the ordered PPy matrix contained 144 PPy chains in a 8.71 nm × 6.77 nm × 2.90 nm box.

Construction of Polypyrrole/Peptide Systems

The final, relaxed structure of the bulk PPy matrices were used as starting structures for simulations incorporating peptides. First, the last snapshot of PPy was taken, and the smaller box dimension was expanded to 10 nm to create a surface. This was done outside of any simulation, and the result produced a packed, PPy matrix with vacuum above it. After expanding the box, 5 ns of constant volume (NVT), room temperature simulation was conducted for the amorphous PPy matrix to allow the matrix to respond to the new surface. Strong intermolecular interactions kept the PPy matrix packed, and the purpose of this sampling was to allow any PPy chains that were overly exposed to vacuum to lay back down against the PPy surface. The T59 peptide was then placed into the middle of the newly created vacuum region of the box, and the rest of the box was filled with TIP4P water. Five nanoseconds of 1000K NVT MD was used to allow the peptide to sample freely and to generate starting structures for the replica exchange molecular dynamics simulation described in the following section.

Replica Exchange Molecular Dynamics

Replica exchange molecular dynamics (REMD) simulates a number of non-interacting replicas of a system and, at predefined intervals, takes the instantaneous energy of each replica (Sugita and Okamoto 1999). Adjacent pairs of replicas are compared, and the lower energy snapshots are assigned the lower temperature of each pair following standard metropolis criteria. As an example, a set of one hundred replicas would produce fifty pairs during the initial exchange attempt (e.g. replicas 1 and 2 would be compared). At the next exchange attempt, the complementary set of replica pairs would be used for the exchange (e.g. replicas 2 and 3 would be compared). Taken

directly from Sugita and Okamoto's paper, the exchange probability, *w*, between two adjacent replicas, *X* and *X'*, is:

$$w(X \rightarrow X') = \begin{cases} 1, & for\ \Delta \leq 0 \\ \exp(-\Delta), & for\ \Delta > 0 \end{cases}$$

where Δ is given by the following equation:

$$\Delta = [B_n - B_m]\left(E\left(q^{[i]}\right) - E\left(q^{[j]}\right)\right)$$

The variable B is the inverse of $k_B T$, the subscripts *n* and *m* refer to the temperatures of the two replicas, and the superscripts *i* and *j* refer to the replica numbers. E(q) is the instantaneous potential energy in the system (kinetic energy is ignored). Upon a successful exchange, the velocities of all particles are scaled to match the new temperature. The exchange probability carefully uses the Boltzmann distribution to maintain the proper ensemble at a given temperature even though the trajectories are discontinuous. The affect is that replicas trapped in higher energy conformations will be moved to higher temperatures to increase their kinetic energy and hopefully allow them to transition into more energetically favorable conformations. Though the trajectory at a given temperature is discontinuous, it has been shown that at each temperature, the ensemble follows a Boltzmann distribution, which is required to draw meaningful statistical measurements.

For our simulations, we chose a temperature range between 300K and 650K. When choosing a temperature distribution, there is always a trade-off between the exchange probabilities between replicas and the total temperature range spanned by the simulation. High exchange probabilities allow replicas to traverse the temperature space more quickly, but they make it very computationally expensive to cover a wide range of temperatures. In addition, having a large number of replicas also makes it slower for

replicas to traverse the full temperature range, since each exchange attempt is only between neighbors.

To span temperatures between 300K and 650K, we chose to have an exchange probability of 0.15 or higher. Following previously published guidelines, we chose to attempt exchanges every 500 steps. To select temperatures, we generated an initial, exponential distribution of temperatures and ran small test runs of 100 exchanges to refine our temperatures and obtain a flat exchange probability across the temperature range. Our final temperatures, which resulted in 136 replicas, were the following: 300.00, 301.44, 302.90, 304.37, 305.84, 307.34, 308.84, 310.35, 311.88, 313.42, 314.97, 316.53, 318.10, 319.69, 321.29, 322.90, 324.52, 326.16, 327.81, 329.47, 331.15, 332.84, 334.54, 336.26, 337.98, 339.73, 341.48, 343.25, 345.04, 346.84, 348.65, 350.48, 352.32, 354.18, 356.05, 357.93, 359.83, 361.75, 363.68, 365.63, 367.59, 369.57, 371.56, 373.57, 375.60, 377.64, 379.70, 381.78, 383.87, 385.98, 388.10, 390.25, 392.41, 394.58, 396.78, 398.99, 401.22, 403.47, 405.74, 408.03, 410.33, 412.66, 415.00, 417.36, 419.74, 422.14, 424.56, 427.00, 429.46, 431.94, 434.45, 436.97, 439.51, 442.07, 444.66, 447.26, 449.89, 452.54, 455.21, 457.90, 460.62, 463.36, 466.12, 468.90, 471.71, 474.54, 477.39, 480.27, 483.18, 486.10, 489.05, 492.03, 495.03, 498.06, 501.11, 504.19, 507.29, 510.42, 513.58, 516.76, 519.97, 523.21, 526.47, 529.77, 533.09, 536.44, 539.81, 543.22, 546.66, 550.12, 553.62, 557.14, 560.70, 564.28, 567.90, 571.55, 575.23, 578.94, 582.68, 586.46, 590.27, 594.11, 597.98, 601.89, 605.83, 609.81, 613.82, 617.87, 621.95, 626.07, 630.22, 634.41, 638.64, 642.91, 647.21, 651.55. It was interesting to note that the commonly used online temperature generator did not yield good results for our system. That generator is tuned to the heat capacity of water and protein, and since polypyrrole comprised almost 20% of our system, it gave us skewed results. Selecting temperatures manually only required a

couple of revisions to obtain a flat exchange probability distribution, and produced satisfactory results in the production run.

For REMD simulations, the polypyrrole chains were restrained within the Z-axis to prevent chains from detaching from the surface at high temperatures. The chains were allowed to shift parallel to the surface to allow some flexibility in the binding interactions.

Computational Alanine Scanning

Alanine scanning is a popular technique to gauge the relative importance of individual amino acids in protein-protein binding interactions. The sampling methods utilized in alanine scanning vary from study to study, but the general concept is to compare the binding free energy of the native system to that of a system where one amino acid has been truncated at the beta carbon to become an alanine:

$$\Delta\Delta G_{bind} = \Delta G_{variant} - \Delta G_{native} \qquad (1)$$

In Equation 1, ΔG_{native} is the binding free energy of the T59 peptide and polypyrrole, which may in turn be described with the following equation:

$$\Delta G_{bind} = \Delta E_{MM} + \Delta G_{sol} - T\Delta S \qquad (2)$$

where ΔE_{MM} is the change in energy upon binding due to molecular mechanics bonded and non-bonded interactions. ΔG_{sol} is the change in solvation free energy, T is temperature, and ΔS is the change in entropy. From the REMD trajectory, we extracted one thousand snapshots of the room temperature trajectory at 10 ps increments, truncated a single amino acid at the beta carbon, and added hydrogen atoms back to form alanine. The explicit water was removed and replaced with an implicit representation so that re-equilibration of the water around the mutated amino acid would not be required. The

instantaneous energies of the variant systems were computed for each snapshot. Electrostatic interactions were represented with a relatively long cutoff distance of 2.0 nm, and the $E_{MM\ and}\ G_{sol}$ terms were computed directly for each snapshot. To capture the unbound state, the protein and polymer were separated into different systems, and their internal energy and free energy of solvation were calculated. As others have done before us, we make the approximation that the change in entropy is small between similar ligands and neglect the term. Estimating entropy to account for the last term of Equation 2 may be accomplished multiple ways, such as through normal mode analysis or by calculating the derivative of the free energy change over temperature, but all these methods have a significant computational expense. For determining the relative importance of different amino acids, we believe the approximation that entropy changes are small is acceptable.

Our REMD simulations used explicit water molecules, which is more accurate but more expensive to compute and slow to adapt to a truncated side chain. For mutating residues and computing instantaneous energies of an existing trajectory, the implicit GBSA representation was a natural choice for two reasons: 1) rearrangement of water molecules around the mutated peptide was not required, and 2) using a cutoff for electrostatics instead of the particle mesh Ewald (MPE) method made is easy to directly compute the energies and to separate the peptide and polymer into isolated systems. Explicit water is a more accurate representation, but GBSA is well suited for and frequently used in protein-protein binding studies (Yan, Kaoud et al. 2011). As we will discuss, there are some limitations in how the free energy of solvation is calculated.

One caveat of current implicit solvent implementations is that they do not incorporate periodic boundaries, so the peptide interacts with only one copy of the PPy matrix. This is not a limit on the theory, but rather the software's capability. Since our

original simulation used periodic boundaries, in a given snapshot, the peptide may be near the edge of the simulations box and interact strongly with one of the periodic images of PPy. To overcome that potential source of error, each of the one thousand extracted frames was first translated such that the peptide was centered in the box.

The ensemble of snapshots analyzed follows the behavior of the native peptide, and it is expected that mutating key residues to alanine would likely disrupt the peptide's behavior. A more rigorous analysis would involve running separate trajectories for the variant system or using a free energy perturbation approach to compare energies between variants in both the bound and unbound state, but the computational time required for such approaches is extensive, since additional sampling for each mutation is required. Single-step perturbation techniques have been demonstrated using only one ensemble, but they also require adequate sampling of the low energy states of all the perturbed systems as well as the native system (Liu, Mark et al. 1996). Achieving this sampling requirement over an amorphous material surface is still a challenge. A carefully constructed set of biasing potentials could be successful, and this approach may prove useful for exploring surface interactions in the future. Our goal was to use a less computationally expensive method in hopes to give precedent for screening a large number of variants. Within the context of identifying the relative contributions of different amino acids, using implicit solvent and capturing instantaneous energies is generally very useful, computationally inexpensive, and applicable to the study of a wide range of systems.

5.3 Results and Discussion

Polymer Properties

From earlier work, we have characterized the density, torsion angle distribution, and N-N and N-Cl radial distribution functions (RDF) of ordered and amorphous PPy matrices utilizing this model. **Figure 5.1** shows good agreement in the density values of our matrices compared to our previous work. Values of 1.263 g/cm^3 for ordered PPy and 1.137 g/cm^3 for amorphous PPy are below experimentally measured values, but that is likely a limitation of the model, either from the lack of polarization or the exclusion of bipolarons. **Figure 5.2** contains the torsion angle distributions for the amorphous and ordered matrices. The ordered matrix should contain very high peaks at +/– 180° since the chains are placed pre-packed with an initial 180° configuration. For the amorphous matrix, we expect the polymer to contain roughly equal peaks at 0° and 180°, which are the planar and energetically favorable torsion angles for PPy monomers near a doping site. For both matrices, a small peak around +/– 30° is from PPy monomers not next to a dopant ion. This slightly out-of-plane behavior is observed in previous quantum mechanics calculations. RDFs, shown in **Figure 5.3**, show peaks as expected. Chloride ions doping PPy are tightly held at 0.3 nm from the nitrogen atoms in pyrrole ring. N-N RDFs reveal extensive pi-pi stacking in the crystal structure (given by the peak at 0.3 nm) and less organized behavior for the amorphous matrices. All indicators showed that the matrices were formed as intended and were representative of converged, minimized PPy.

From the perspective of the surface, **Figure 5.4** illustrates the drastic difference in surface roughness between the amorphous and ordered polymer. We expect the actual roughness of PPy to fall somewhere in between these two sample matrices. As we will discuss later, the surface roughness presents a major challenge in allowing the peptide to sample across the surface of the polymer. Analysis of binding affinity normally

simplifies forces to a one-dimensional reaction coordinate. In systems that contain a defined binding pocket, it is usually not required to sample across the surface of the rest of the protein and collapsing the reaction to a single dimension perpendicular to the surface is straightforward. In the case of material interactions, it is important to sample across the surface of the material, adding an extra two dimensions to an already difficult sampling problem. Additionally, a peptide with strong binding affinity will not readily leave the surface to sample other locations once it is bound. It is incumbent on the biomedical research community to continue exploring new sampling methods to improve our ability to explore large, rugged energy landscapes.

REMD Statistics

Effective REMD simulations rely on consistent exchange probabilities between neighboring temperatures across the full range simulated. Exchange probabilities that are too low break the connection between hotter and colder temperatures. A similar exchange probability at every temperature allows each replica to perform a random walk up and down the temperature range. We targeted an exchange probability of 0.15 as a compromise between fast exchanges and a large temperature range. **Figure 5.5** shows exchange probabilities for each pair of neighboring temperatures and confirms that we were able to obtain consistent overlap between the potential energy distributions of adjacent replicas and a reasonably flat exchange rate across all temperatures.

Another way to test how well replicas are traversing the temperature space is to track individual replicas as they move. **Figure 5.6** shows the paths of five equally spaced replicas over 10,000 exchanges (5,000 even exchanges and 5,000 odd exchanges). The replicas are able to traverse the entire temperature space and show generally good trends.

Over the course of the simulation, it is ideal to see a replica able to travel the entire temperature space and back at least once. The movement in our simulation is not that fast due to the large number of temperatures, but the simulation may always be extended to gather further sampling.

Polymer/Peptide Binding Interactions

The flexibility and number of degrees of freedom of a 12-amino acid peptide make it very difficult to quantitatively calculate the binding free energy. The peptide is small enough that it lacks a well-defined secondary structure, but large enough to frustrate attempts to, for example, use the center of mass as a reaction coordinate. The other layer of complexity with a material such as PPy is that there is not a well-defined binding pocket. The peptide must be able to sample across the surface to find the best binding locations. The constant challenge in simulating binding interactions using molecular dynamics is always achieving good accuracy in the force field and sufficient sampling, but sampling becomes especially important for larger ligands like the T59 peptide. We chose REMD to enhance the sampling of the system without artificially limiting the movement of the peptide. The 136 replicas in our simulation provide 1.4 microseconds of simulation time, and the high temperature replicas increase the kinetic energy of the system enough to free the peptide from local energy traps.

We attempted to use two metrics to measure the relative binding contributions of different amino acids. The first was to measure the minimum distance between each amino acid and the nearest polypyrrole atom for every frame in the room temperature trajectory. By taking a histogram of these distances for each amino acid, we can observe how closely each amino acid binds to PPy and how frequently it is in contact with the

surface. This minimum distance histogram is a type of non-normalized radial distribution function in that it captures the likelihood of finding a specific amino acid within a certain distance of the polypyrrole surface. The histogram therefore also relates to the potential of mean force (PMF) of the system. Two aspects prevented us from going further to calculate the PMF. The first is that the PMF requires thorough sampling of all possible conformations at all measured distances. Given that multiple binding locations likely occur on the PPy surface, we have no guarantee that this requirement was met. Second, each amino acid is covalently bound to its neighbor, which means the distances between the amino acids and PPy are correlated with each other.

From the results of the minimum distance analysis, portrayed in **Figure 5.7**, the aspartic acid at position eight binds the closest to PPy for ordered PPy (Figure 5.7a), with a peak contact distance of 0.165 nm. From examining the snapshots of the trajectory qualitatively, the negatively charged aspartic acid appears to displace a dopant ion and interact with PPy exactly where we would normally see a chloride ion – near the N-H atoms of the PPy ring in the same plane as the ring structure. The aromatic amino acids tyrosine and phenylalanine also tended to lay flat against the PPy surface in a "pi-stacking" configuration in some snapshots. Toward the N-terminal of the peptide, we observed less defined interaction. These amino acids likely contribute to better solubility and may also help orient the peptide. At the same time, we observed some snapshots where the entire T59 peptide is laying unfolded against the PPy surface, so PPy does not necessarily repel the N-terminal side. The bound structure of T59 does not have a dominant secondary structure. The selectivity for PPy is more likely a combination of hydrophobic affects and the negatively charged aspartic acid near the aromatic rings of tyrosine and phenylalanine.

In the simulation containing amorphous PPy (Figure 5.7b), the hydrophobic amino acids surrounding the aspartic acid on the C-terminal side of the peptide (isoleucine, valine, tyrosine, phenylalanine, and leucine) also appear to have a strong role in stabilizing the peptide. Upon examining the trajectory, we observe that a concave pocket in the amorphous PPy created a very stable binding site for the hydrophobic T59 residues. Due to steric limitations, the aspartic acid was held away from the PPy surface, and we do not observe the expected binding peak for aspartic acid in Figure 5.6b. Multiple replicas converged to this location in the polymer, which prevented the simulation from sampling across the full PPy surface. This type of hydrophobic interaction likely contributes to the binding affinity T59 has for PPy, but it is undesirable for our simulation to spend so much time in that pocket. REMD replicas should sample a broad phase space, so having multiple replicas dwell in the same energy well damages the statistics we are able to extract from the simulation. This simulation also demonstrates the difficulty of characterizing the interaction between a peptide and an amorphous material.

We attempted to perform computational alanine scanning on the ordered PPy REMD trajectory. Both the trajectory and Figure 5.7b indicated that the peptide was unable to sample broadly over the amorphous PPy surface, so we focused our alanine scanning analysis on the ordered matrix. In **Figure 5.8**, the results of the computational alanine scanning appear to contain large errors from the generalized Born implementation. Two large approximations were made to prepare our system for alanine scanning: 1) explicit solvent was replaced with implicit solvent, and 2) the periodicity of the system was removed. For the two charged amino acids in our peptide, their removal resulted in a large penalty in the solvation free energy of around 500 kJ/mol relative to the other mutations. An energy penalty makes sense, since a charged residue is

hydrophilic, while alanine is slightly hydrophobic, but this energy should be offset by a penalty in the energy of the bound system, which no longer benefits from the electrostatic interactions with the charged residue. In the case of aspartic acid, the system energy does not rise proportionately, and $\Delta\Delta G$ is a negative number, signifying that aspartic acid was a favorable mutation. For arginine, which frequently interacts with the solvent, the system energy appears over-penalized and the $\Delta\Delta G$ indicates that arginine is a key residue in the binding interaction.

We suspect that one source of error from using implicit solvent in our calculation is how the algorithm treats PPy. Polypyrrole is a highly charged system, and some explicit water had penetrated the polymer, as it does experimentally. The over- or under-estimation of solvent in the polymer strongly affects the charge screening behavior, and can result in large errors. It may be possible to improve the performance of these calculations by carefully adjusting the effective Born radii of PPy, but the more likely conclusion is that this method applies too many approximations to be effective for alanine scanning with a periodic polymer system. The un-charged residues do slightly follow the anticipated trend, with the C-terminal side showing slightly larger energy changes upon mutation, but in light of the apparent errors for the charged residues, the other results are hardly trustworthy.

As future direction, there are alternatives to computational alanine scanning, but they are significantly more computationally expensive. They could serve as a diagnostic tool for a few mutations, but not in the predictive fashion that is needed. Free energy perturbation methods using explicit solvent require separate simulations for each mutation in both the bound and unbound states, but they can simulate a handful of mutations for a reasonably sized system. Some have used the Jarzynski equality to perform simulated pulling simulations to calculate binding affinity, but these simulations

require many binding events to be simulated, and the pulling velocity *in silico* is so much faster than experimental atomic force microscopy that this technique draws some skepticism. Implicit solvent models are under constant investigation, and improvements both in the representations and the implementation will likely make it worth revisiting in a few years.

5.4 CONCLUSIONS

Computational simulations to calculate binding affinities have contributed greatly to the drug design industry when drug molecules are small and the binding pocket is well defined. Designing implant material surfaces adds another layer of complexity to the problem with less defined binding sites, larger and more flexible ligands, and an increased sampling requirement to garner useful results. As computer power increases, however, these types of calculations are a natural extension to an already established field. For molecular mechanics models, it is easier and more accurate to make relative binding measurements, which, given the ability of phage display to discover binding candidates, complements experimental techniques in understanding and refining peptide binding mechanisms. In this study, the ability to visualize and qualitatively understand the binding mechanism of T59 to PPy was very valuable. We hoped that computational alanine scanning would provided a quantitative method of ranking the importance of the different amino acids, but the omission of the entropy term, the complications with implicit solvent, and the removal of periodicity overshadowed the utility of the results. The replica exchange sampling approach was very helpful because it did not require a known reaction coordinate and it scaled extremely well since each replica runs independently except for the exchange step; however, scaling temperature alone was

clearly not enough to allow the peptide to sample freely in the case of our amorphous simulation. More generalized implementations of REMD that do not use temperature as the variable are being explored, so this method may be more effective in future adaptations. As computer resources and sampling algorithms improve computational binding calculations will naturally be able to expand to larger systems with more complex ligands. In its current state, simulation still provides some insight not readily available experimentally, but it is limited in the quantitative data that it can produce.

5.5 FIGURES

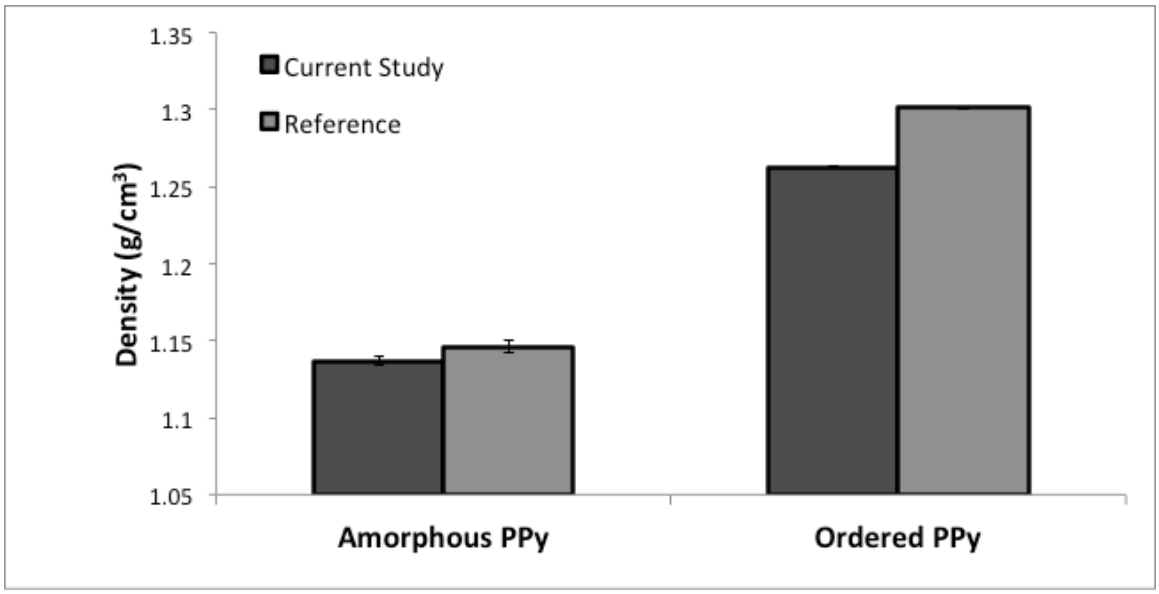

Figure 5.1. Density of amorphous and ordered PPy.

The current work matches previously published work closely and indicates a converged, relaxed matrix. The density for ordered PPy is slightly lower, most likely because the box size and configuration are slightly different. The current work uses a thinner, wider box.

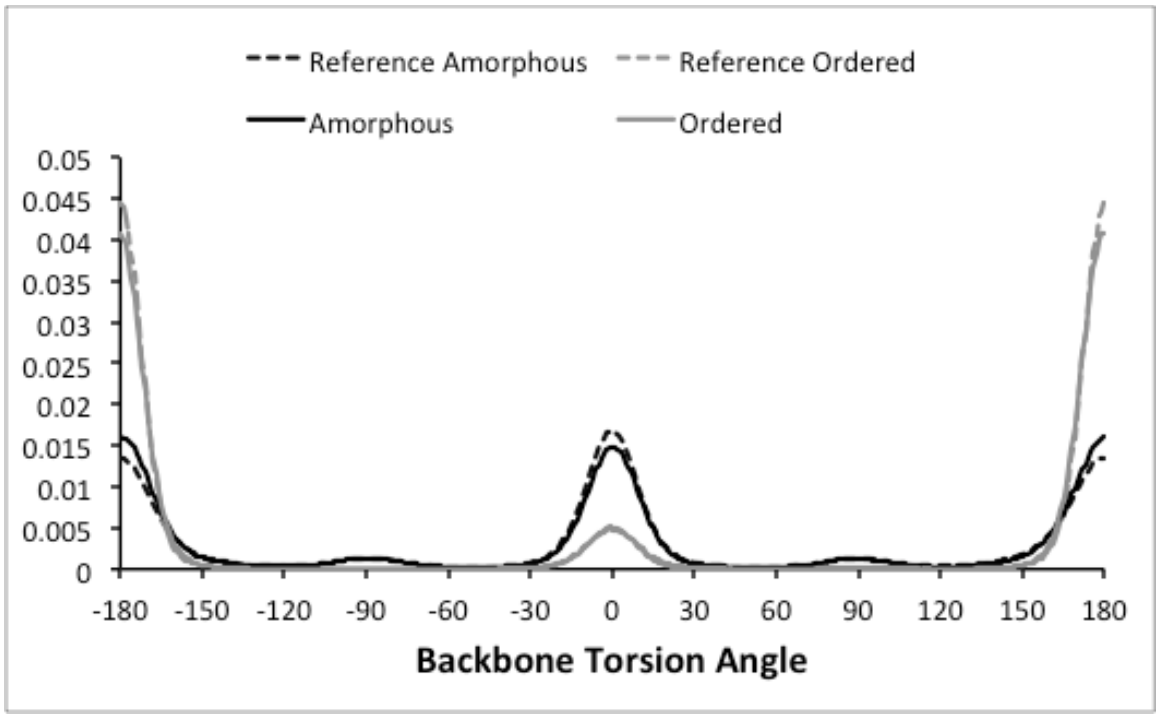

Figure 5.2. Torsion angle distribution for amorphous and ordered PPy.

From previous quantum mechanics data, we expect roughly equal occurrences of *cis* and *trans* backbone angles for an unconstrained, amorphous PPy matrix. There is good agreement between our amorphous results, previously published work, and expectations from quantum mechanics energetics. For ordered PPy, the polymer is packed in a *trans* configuration, and few monomers flip during the course of the simulation, so we see higher occurrences of backbone angles near 180°.

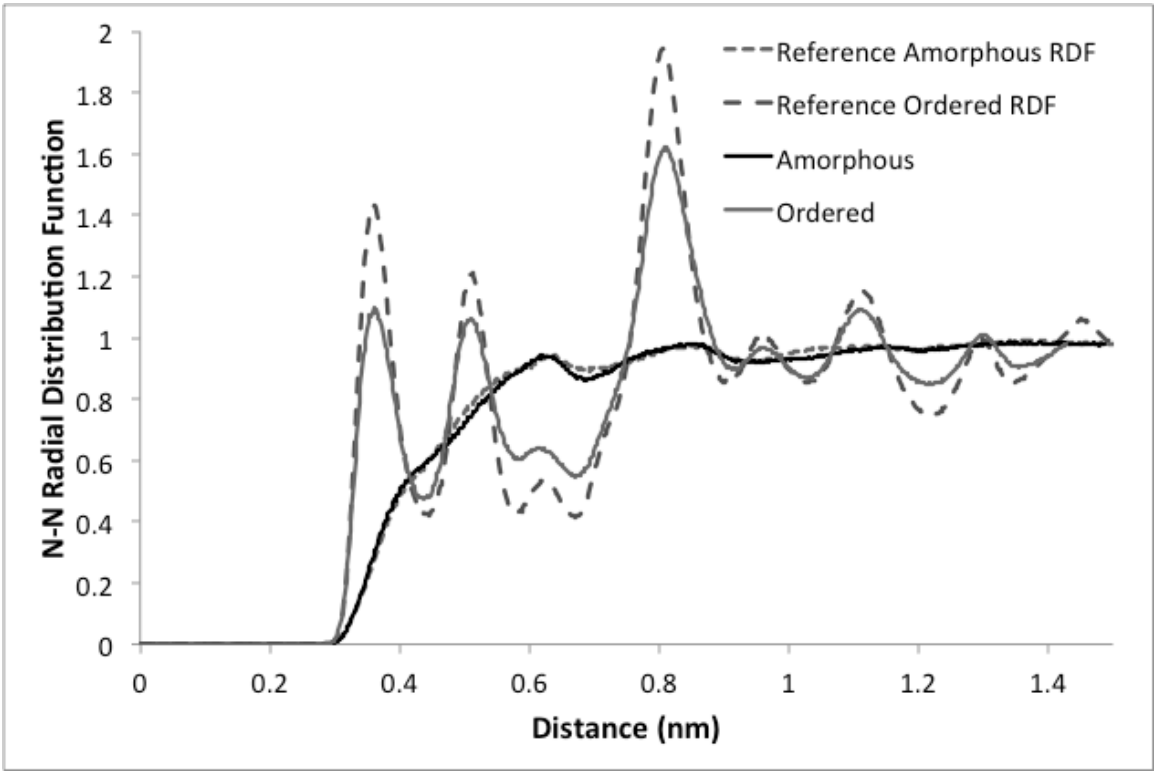

Figure 5.3 Radial distribution functions for amorphous and ordered PPy.

Radial distribution functions reveal that the chain packing in the current work matches expectations from previous work. The peaks for ordered PPy are less exaggerated than the reference results, indicating slightly less patterned packing. This agrees with the slightly lower density values obtained and is likely a result of chains sliding in the wide, thin box dimensions. Amorphous PPy appears to be packed almost exactly as previous work.

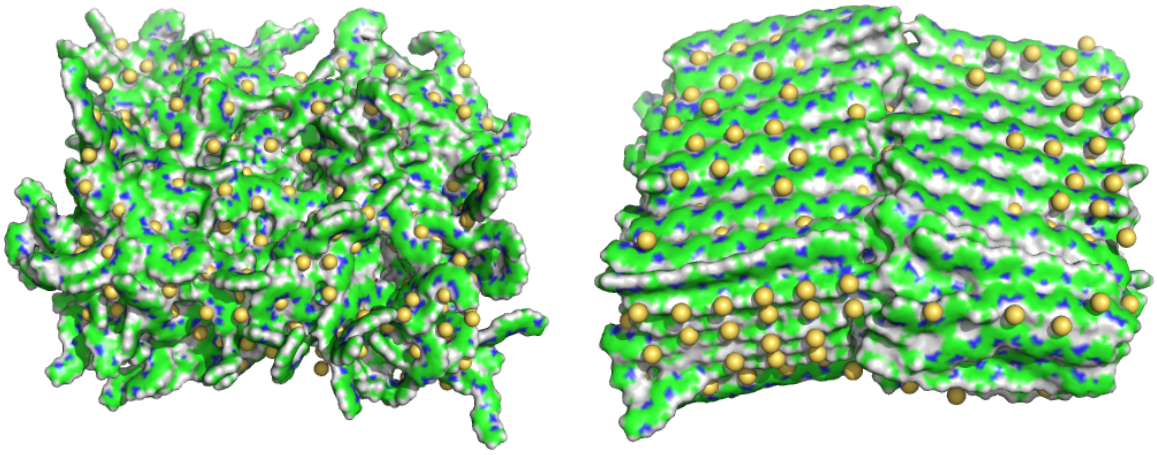

Figure 5.4 Snapshots of amorphous and ordered PPy.

Periodic boundary conditions exist on the sides of the polymer matrix, but the top is in contact with water and peptide. The rugged surface of amorphous PPy presents a real challenge to direct the peptide to sample over the surface

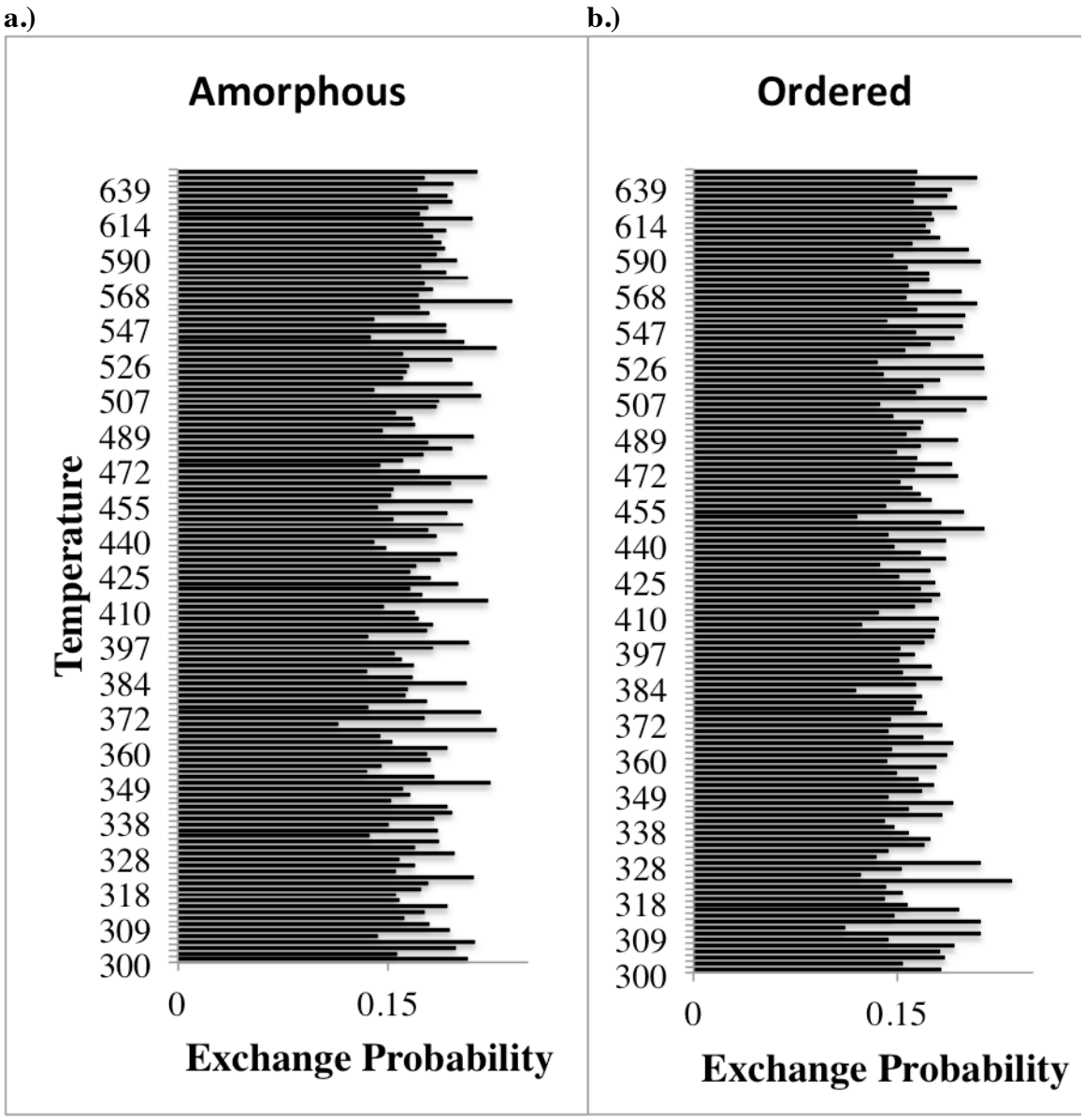

Figure 5.5. Exchange probabilities during REMD simulations for Amorphous and Ordered PPy.

Replica exchange temperatures were chosen to obtain approximately a 0.15 acceptance ratio for exchanges. Statistics over 10,000 exchange attempts confirm that exchange probabilities were consistent across the entire range of temperatures.

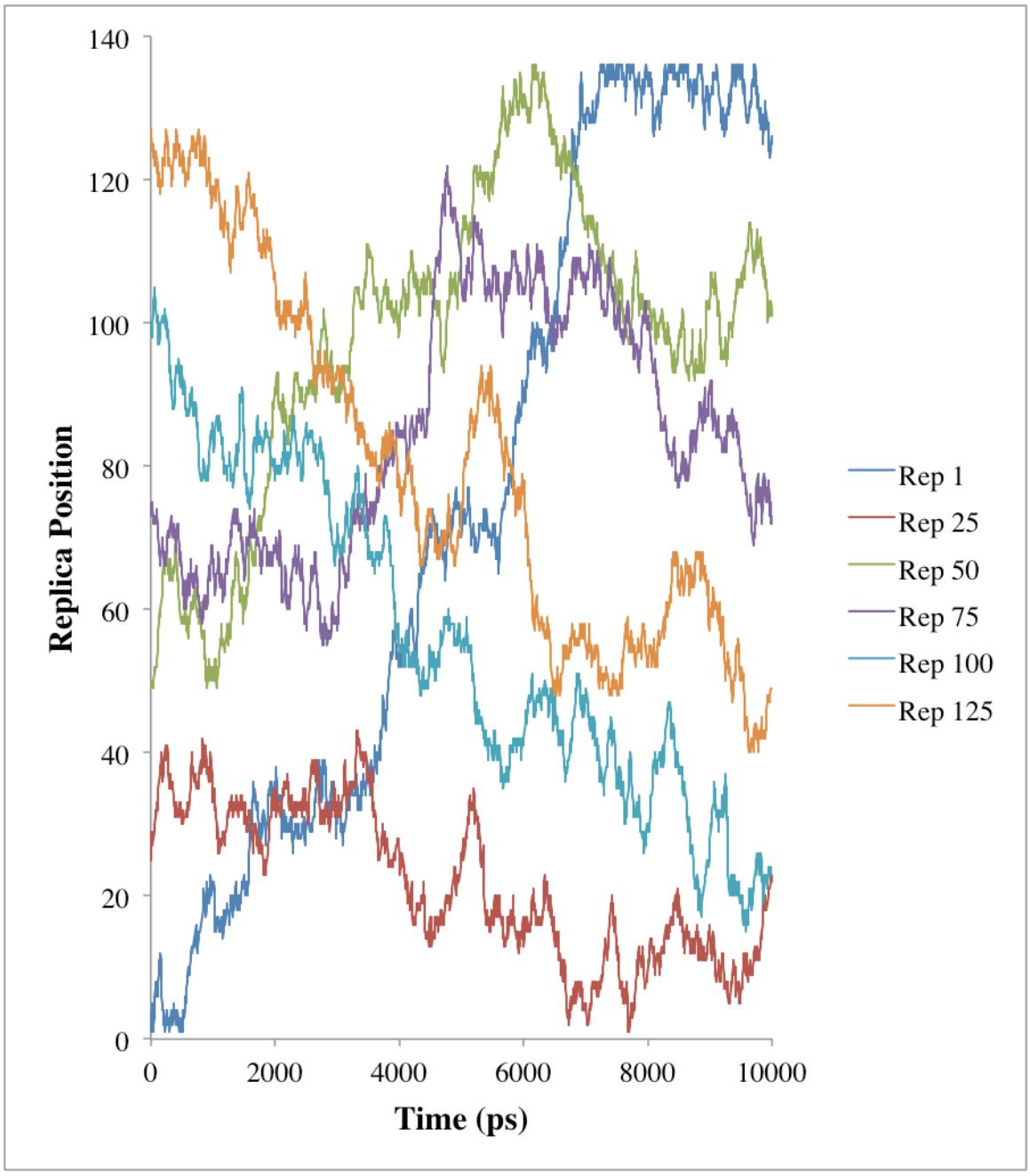

Figure 5.6. Example, continuous trajectories traversing temperature space.

Equal exchange probabilities over all temperatures allow replicas to perform a random walk up and down temperatures. Ideally, trajectories should be able to traverse the temperatures and return within the simulation time, but having a large number of replicas slows this movement.

a.)

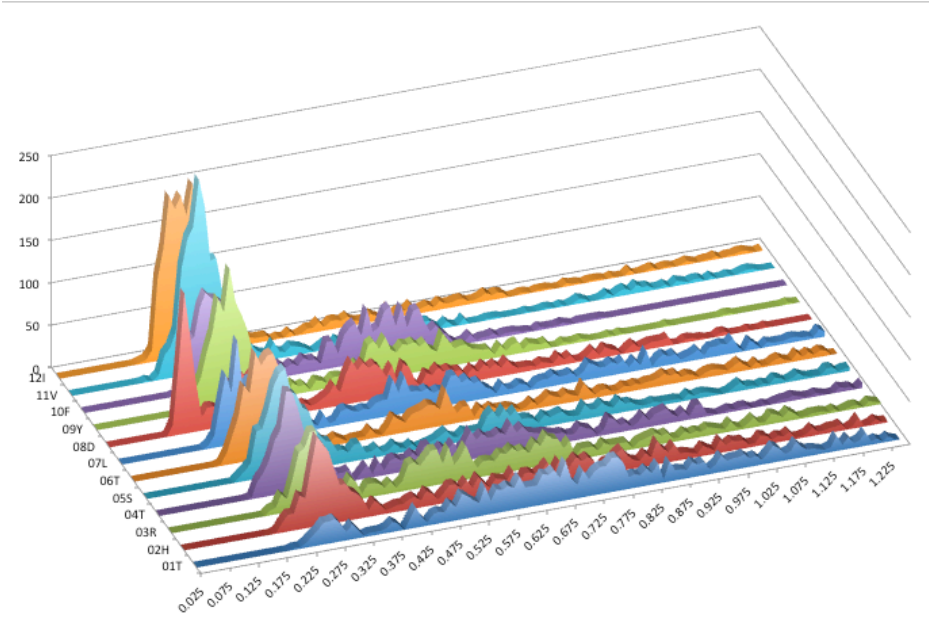

b.)

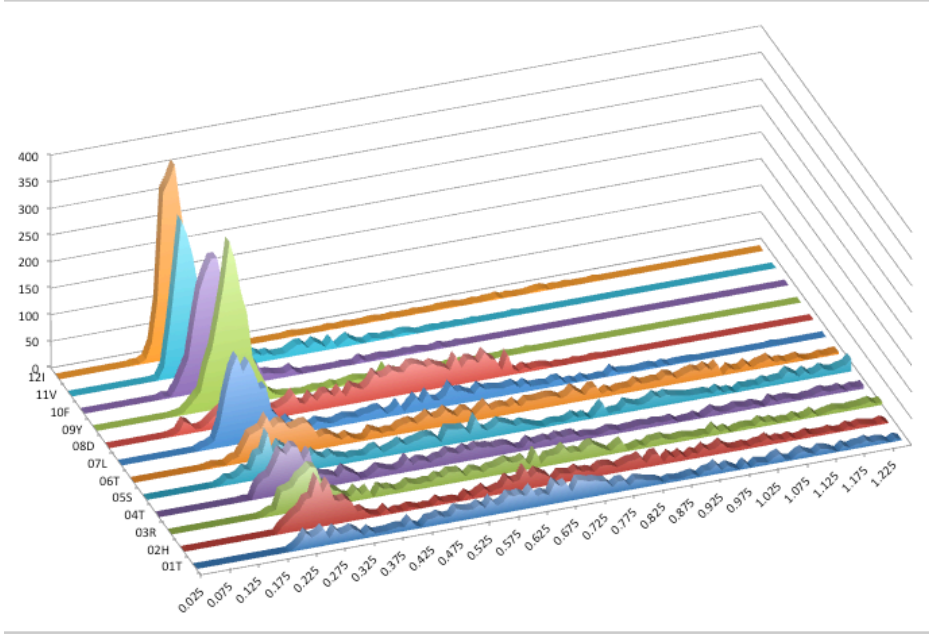

Figure 5.7. Histogram of the distance between PPy and the closest atom of each amino acid.

Since MD sampling follows a Boltzmann distribution for energetics throughout the simulation, the time that a molecule spends in a given state relates to the energy of that conformation. Though amino acids are correlated with one another, we can expect amino acids with greater binding affinities to dwell near the polymer surface ore frequently.

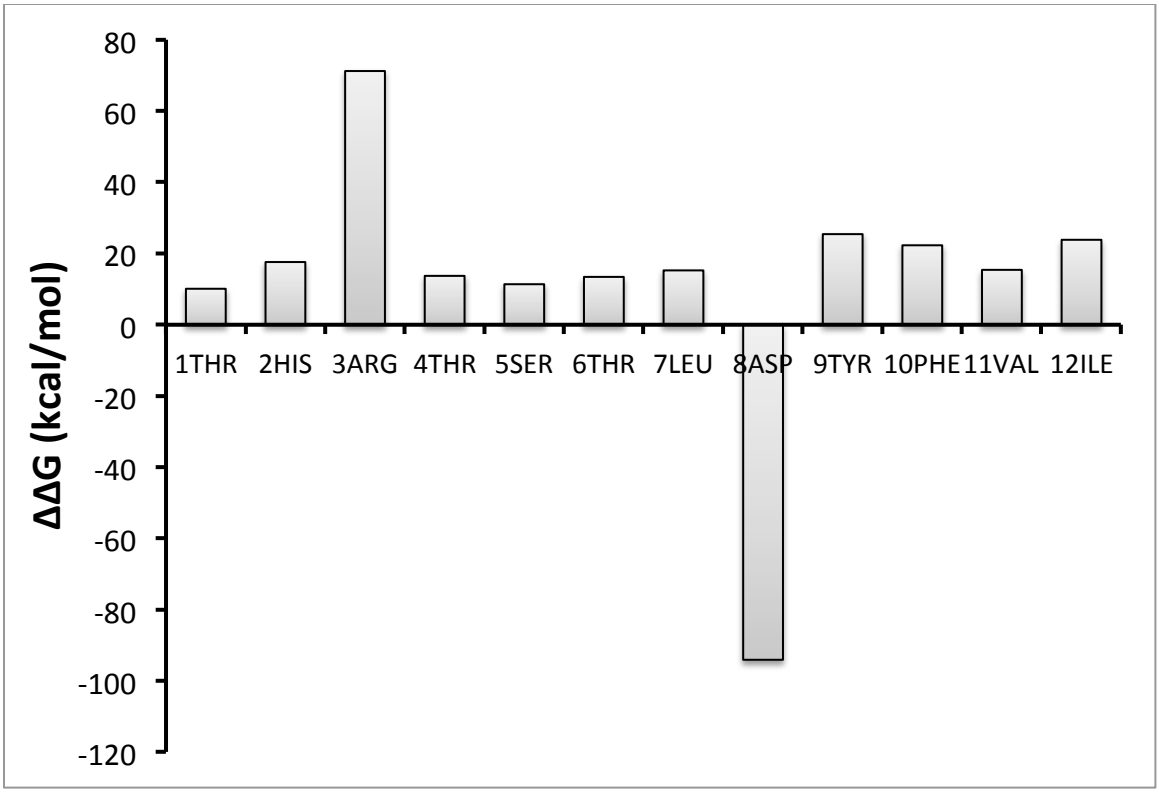

Figure 5.8. Computational Alanine Scan.

ΔΔG represents the change in binding free energy when mutating a residue to alanine. Positive values indicate an energy penalty upon mutation to alanine, meaning the native amino acid is better. Negative values indicate a favorable energy change for mutating to alanine. The charged residues, arginine and aspartic acid, yielded strange, non-physical results. We are led to believe that this alanine scanning method is better suited for protein interactions, where the solvent accessible surface approximation is clearer and where a non-periodic system makes sense.

5.6 REFERENCES

Collier, G., N. A. Vellore, et al. (2009). "Development of molecular simulation methods to accurately represent protein-surface interactions: Method assessment for the calculation of electrostatic effects." Biointerphases **4**: 57.

Fonner, J. M., C. E. Schmidt, et al. "A combined molecular dynamics and experimental study of doped polypyrrole." Polymer **In Press, Corrected Proof**.

Huang, X., S. Zauscher, et al. (2010). "Peptide interfacial biomaterials improve endothelial cell adhesion and spreading on synthetic polyglycolic acid materials." Annals of biomedical engineering **38**(6): 1965-1976.

Jorgensen, W. L., J. Chandrasekhar, et al. (1983). "Comparison of Simple Potential Functions for Simulating Liquid Water." Journal of Chemical Physics **79**: 926-935.

Kaminski, G. A., R. A. Friesner, et al. (2001). "Evaluation and Reparametrization of the OPLS-AA Force Field for Proteins via Comparison with Accurate Quantum Chemical Calculations on Peptides†." J. Phys. Chem. B **105**(28): 6474-6487.

Lee, J. W., F. Serna, et al. (2006). "Carboxylic acid-functionalized conductive polypyrrole as a bioactive platform for cell adhesion." Biomacromolecules **7**(6): 1692-1695.

Liu, H., A. E. Mark, et al. (1996). "Estimating the relative free energy of different molecular states with respect to a single reference state." The Journal of Physical Chemistry **100**(22): 9485-9494.

Liu, X., P. K. Chu, et al. (2004). "Surface modification of titanium, titanium alloys, and related materials for biomedical applications." Materials Science and Engineering: R: Reports **47**(3-4): 49-121.

Meyers, S. R., P. T. Hamilton, et al. (2007). "Endothelialization of titanium surfaces." Advan. Mater **19**: 2492-2498.

Meyers, S. R., X. Khoo, et al. (2009). "The development of peptide-based interfacial biomaterials for generating biological functionality on the surface of bioinert materials." Biomaterials **30**(3): 277-286.

Mongan, J., C. Simmerling, et al. (2007). "Generalized Born model with a simple, robust molecular volume correction." Journal of Chemical Theory and Computation **3**(1): 156-169.

Onufriev, A., D. Bashford, et al. (2004). "Exploring protein native states and large-scale conformational changes with a modified generalized born model." PROTEINS-NEW YORK- **55**(2): 383-394.

Sanghvi, A. B., K. P. H. Miller, et al. (2005). "Biomaterials functionalization using a novel peptide that selectively binds to a conducting polymer." Nature Materials **4**(6): 496-502.

Still, W. C., A. Tempczyk, et al. (1990). "Semianalytical Treatment of Solvation for Molecular Mechanics and Dynamics." Journal of the American Chemical Society **112**(16): 6127-6129.

Sugita, Y. and Y. Okamoto (1999). "Replica-exchange molecular dynamics method for protein folding." Chemical Physics Letters **314**(1-2): 141-151.

Yan, C., T. Kaoud, et al. (2011). "Understanding the Specificity of a Docking Interaction between JNK1 and the Scaffolding Protein JIP1." The Journal of Physical Chemistry B.

CHAPTER SIX

Conclusion

6.1 SUMMARY

The key to improving the performance of chronic implants in the nervous system is at the material/tissue interface, yet all of the most common, FDA approved implant materials used were chosen for their bulk properties. Designing material interfaces that elicit positive host and immune responses, avoiding the fibrous encapsulation that is currently standard in the field, will create opportunities for implant applications that are currently impossible. The goal of this work was to evaluate computational simulations as a complement to experiment for engineering affinity binding peptides. Through this process, several contributions were made to the field. In our experimental characterization of polypyrrole (PPy) discussed in Chapter 3, we focused on parameters important for biomaterials and carried the work through to cell studies examining cell survival and morphology. Though our contribution is preceded by a voluminous quantity of PPy studies, the vast majority of those studies are for applications outside of biomedical engineering, and few others have carried the analysis through to cell outcomes. Our model of polypyrrole reported in Chapter 4 offers an effective tool for researchers using PPy and a precedent for other groups seeking to model polymers. The quantum mechanics calculations used for parameterization and the molecular mechanics implementation itself are not designed for systems like doped polypyrrole where significant charge localization and polarization is caused by interactions with a second, mobile species. The parameterization is a contribution in itself, and the quantum mechanics description of the backbone torsion behavior is also valuable. The binding calculations in Chapter 5 are perhaps the most exciting and ambitious effort in this work.

Protein/surface interactions have been simulated before, but usually the conformation of the protein is somehow constrained and only the orientation of the protein in the main focus (Agashe, Raut et al. 2005; Ganazzoli and Raffaini 2005). With most interesting research topics, research begets more research, and this study is no exception. The closing paragraphs of this chapter will be devoted to the future projects and foci that seem the most promising and captivating.

6.2 Conclusion on Experimental Characterization of Polypyrrole

In Chapter 3, we characterized how polypyrrole synthesis parameters alter biomedically relevant properties. We electrochemically synthesized PPy in aqueous solvent on both gold and indium tin oxide substrates using three dopant ions of very different sizes: chloride, tosylate, and polystyrene sulfonate. Using numerous synthesis times, we created PPy films in a range of thicknesses spanning three orders of magnitude from tens of nanometers to over ten microns. We quantified the rate of film growth for all three dopants on both substrates to improve our ability to reproducibly create films of a specific thickness. Trends in roughness related to dopant choice and film thickness were recorded, dopant concentration and conductivity changes over time were monitored, and relative hydrophobicity was measured, all of which equip researchers to choose synthesis parameters to match their needs and specific applications. We took the study a step further, and cultured PC-12 cells and Schwann cells on thin and thick PPy films with each of the three dopants studied. In a dopant dependent manner, film thickness affected cell survivability, and we noted that Schwann cells tended toward different morphologies for each of the dopants.

The intense characterization required for PPy illustrates that its properties and the cell response it elicits is a complex combination of many factors. Effectively incorporating PPy into a larger implant design requires careful attention to detail. Our goal in this study was to make sense of some of the numerous variables involved in PPy synthesis and to thereby enable future researchers to make better choices based on our observations. Polypyrrole is a very promising material, especially for neural applications, and we hope to see effective therapies spring from the foundation of basic research to which we have contributed.

6.3 Conclusion on Computational Model of Polypyrrole

To derive the model reported in Chapter 4, we used quantum mechanics calculations extensively to carefully characterize undoped and chloride doped polypyrrole. Carefully assessing the charge spreading behavior and backbone rigidity for different lengths of doped and undoped PPy oligomers, we created parameters and building blocks suitable for use in molecular mechanics based simulations. We then tested the bulk behavior of our model and compared our results to experimental X-ray diffraction experiments, density measurements, and quantum mechanics behavior. Our tests indicated that we had effectively captured the energetics of the quantum mechanics calculations we performed. *In silico* density measurements were slightly below experimental values, but this difference is likely either a limitation of fixed charge models or a result of not using bipolarons in the model. When compared to previously reported models, our parameters produced better results.

6.4 Conclusion on Polypyrrole Binding Interactions

Building upon the results of our molecular mechanics model, we performed simulations of the binding interaction between the T59 peptide and both amorphous and ordered of polypyrrole. We applied sampling techniques and performed energy calculations that were developed for protein folding, and we reported which methods were most effective and which require further adaptation to work for biomaterial surfaces. Using distance calculations, we were able observe which amino acids adhere most strongly to the PPy surface. The simulations we performed gave some insight into the mechanism of T59's binding affinity for PPy, and they also pave the way for future simulations of similar systems.

6.5 Future Directions

The overall goal of this research was to advance the use of PPy based biomaterials for tissue engineering applications. Our physical characterization of the polymer provides biomedically relevant data to assist researchers in selecting synthesis parameters for their applications, and our own lab has made choices based on this data. Our computational research contributed to improving T59 functionalized PPy as a biomaterial.

Long term, there are several direction that this research may be extended from a computational perspective. First, the model for polypyrrole may be expanded to incorporate bipolarons. Bipolarons have very high charge density, and representing the local environment with fixed charges is challenging, but with very careful attention to how atom types are defines, it is possible. It would be interesting to see how the bulk and surface properties of the simulated polymer change with the inclusion of bipolarons. Also, given that doped polypyrrole contains both an aromatic ring and a chloride ion, it

would be interesting to model the material using a polarizable multipole force field. In such a model, polarization would be able to account for the different charge distributions in bulk PPy versus PPy in contact with water. The polarization component makes the model more transferrable to different environments, and the polarization term allows the model to represent the aromatic ring with greater fidelity. Polypyrrole is a very complex material to model, so in some ways it serves as a proving ground for different parameterization approaches and models.

Another exciting extension to this work would be to continue exploring biomolecule/biomaterial interactions. In some ways, the aforementioned complexity of modeling polypyrrole makes it a difficult material to use for binding calculations, but having experimental data on T59 and several variants makes it an attractive system to model. The software and tools available for molecular dynamics are improving rapidly, and notable improvements have been made even during the process of performing the research in this thesis. Computational chemistry is poised to make larger contributions to many biomedical fields. Based on current trends in the growth of computational resources, it will be very reasonable within five years to perform higher accuracy, explicit water calculations that were prohibitively expensive at the time of writing.

6.6 REFERENCES

Agashe, M., V. Raut, et al. (2005). "Molecular simulation to characterize the adsorption behavior of a fibrinogen -chain fragment." Langmuir **21**(3): 1103-1117.

Ganazzoli, F. and G. Raffaini (2005). "Computer simulation of polypeptide adsorption on model biomaterials." Physical Chemistry Chemical Physics **7**(21): 3651-3663.

BIBLIOGRAPHY

Agashe, M., V. Raut, et al. (2005). "Molecular simulation to characterize the adsorption behavior of a fibrinogen -chain fragment." Langmuir **21**(3): 1103-1117.

Al-Majed, A. A., C. M. Neumann, et al. (2000). "Brief electrical stimulation promotes the speed and accuracy of motor axonal regeneration." The Journal of Neuroscience **20**(7): 2602.

Anderson, J. M., A. Rodriguez, et al. (2008). Foreign body reaction to biomaterials, Elsevier.

Andre, J. M., D. P. Vercauteren, et al. (1984). "Electronic properties of polypyrrole: An ab initio Hartree–Fock study." The Journal of chemical physics **80**: 5643.

Bailey, S., M. Eichler, et al. (1993). "The influence of fibronectin and laminin during Schwann cell migration and peripheral nerve regeneration through silicon chambers." Journal of neurocytology **22**(3): 176-184.

Bentley, D. and T. P. O'Connor (1994). "Cytoskeletal events in growth cone steering." Current opinion in neurobiology **4**(1): 43-48.

Bettinger, C. J., J. P. Bruggeman, et al. (2009). "Biocompatibility of biodegradable semiconducting melanin films for nerve tissue engineering." Biomaterials **30**(17): 3050-3057.

Bolto, B., R. McNeill, et al. (1963). "Electronic conduction in polymers. III. Electronic properties of polypyrrole." Australian Journal of Chemistry **16**(6): 1090-1103.

Boyle, A., E. Genies, et al. (1990). "Electrochemical-Behavior of Polypyrrole Films Doped with Atp Anions." Journal of Electroanalytical Chemistry **279**(1-2): 179-186.

Bray, D. and P. Hollenbeck (1988). "Growth cone motility and guidance." Annual review of cell biology **4**(1): 43-61.

Bredas, J. L., B. Themans, et al. (1983). "Bipolarons in Polypyrrole Chains." Physical Review B **27**(12): 7827-7830.

Breneman, C. M. and K. B. Wiberg (1990). "Determining atom-centered monopoles from molecular electrostatic potentials. The need for high sampling density in formamide conformational analysis." Journal of Computational Chemistry **11**(3): 361-373.

Bufon, C. C. B., J. Vollmer, et al. (2005). "Relationship between chain length, disorder, and resistivity in polypyrrole films." J. Phys. Chem. B **109**(41): 19191-19199.

Bufon, C. C. B., J. Vollmer, et al. (2005). "Relationship between chain length, disorder, and resistivity in polypyrrole films." The Journal of Physical Chemistry B **109**(41): 19191-19199.

Cai, K., M. Frant, et al. (2006). "Surface functionalized titanium thin films: zeta-potential, protein adsorption and cell proliferation." Colloids and Surfaces B: Biointerfaces **50**(1): 1-8.

Carquigny, S., O. Segut, et al. (2008). "Effect of electrolyte solvent on the morphology of polypyrrole films: Application to the use of polypyrrole in pH sensors." Synthetic Metals **158**(11): 453-461.

Cascales, J. J. L., A. J. Fernandez, et al. (2003). "Characterization of the reduced and oxidized polypyrrole/water interface: A molecular dynamics simulation study." Journal of Physical Chemistry B **107**(35): 9339-9343.

Cascales, J. J. L. and T. E. Otero (2005). "Molecular dynamics simulations of the orientation and reorientational dynamics of water and polypyrrole rings as a function of the oxidation state of the polymer." Macromolecular Theory and Simulations **14**(1): 40-48.

Cascales, J. J. L. and T. F. Otero (2004). "Molecular dynamic simulation of the hydration and diffusion of chloride ions from bulk water to polypyrrole matrix." Journal of Chemical Physics **120**(4): 1951-1957.

Chainet, E. and M. Billon (1998). "In situ study of polypyrrole morphology by STM: effect of the doping state." Journal of Electroanalytical Chemistry **451**(1-2): 273-277.

Chehimi, M. M. and E. Abdeljalil (2004). "A study of the degradation and stability of polypyrrole by inverse gas chromatography, X-ray photoelectron spectroscopy, and conductivity measurements." Synthetic Metals **145**(1): 15-22.

Clark, P., P. Connolly, et al. (1990). "Topographical control of cell behaviour: II. Multiple grooved substrata." Development **108**(4): 635.

Collier, G., N. A. Vellore, et al. (2009). "Development of molecular simulation methods to accurately represent protein-surface interactions: Method assessment for the calculation of electrostatic effects." Biointerphases **4**: 57.

Collier, J. H., J. P. Camp, et al. (2000). "Synthesis and characterization of polypyrrole-hyaluronic acid composite biomaterials for tissue engineering applications." Journal of biomedical materials research **50**(4): 574-584.

Cui, X., V. A. Lee, et al. (2001). "Surface modification of neural recording electrodes with conducting polymer/biomolecule blends." Journal of biomedical materials research **56**(2): 261-272.

Cui, X., J. Wiler, et al. (2003). "In vivo studies of polypyrrole/peptide coated neural probes." Biomaterials **24**(5): 777-787.

Dai, Y. and E. Blaisten-Barojas (2008). "Energetics, structure, and charge distribution of reduced and oxidized n-pyrrole oligomers: A density functional approach." Journal of Chemical Physics **129**(16): 8.

Diaz, A. (1981). "Electrochemical Preparation and Characterization of Conducting Polymers." Chemica Scripta **17**: 145-148.

Diaz, A. and K. K. Kanazawa (1983). Polypyrrole: An Electrochemical Approach to Conducting Polymers. New York and London, Plenum Press.

Diaz, A. F. and B. Hall (1983). "Mechanical-Properties of Electrochemically Prepared Polypyrrole Films." Ibm Journal of Research and Development **27**(4): 342-347.

Dowell-Mesfin, N., M. Abdul-Karim, et al. (2004). "Topographically modified surfaces affect orientation and growth of hippocampal neurons." Journal of Neural Engineering **1**: 78.

Dyreklev, P., M. Granstrom, et al. (1996). "The influence of polymerization rate on conductivity and crystallinity of electropolymerized polypyrrole." Polymer **37**(13): 2609-2613.

Einheber, S., T. A. Milner, et al. (1993). "Axonal regulation of Schwann cell integrin expression suggests a role for alpha 6 beta 4 in myelination." The Journal of cell biology **123**(5): 1223.

Fonner, J. M., L. Forciniti, et al. (2008). "Biocompatibility implications of polypyrrole synthesis techniques." Biomedical Materials **3**(3): -.

Fonner, J. M., C. E. Schmidt, et al. "A combined molecular dynamics and experimental study of doped polypyrrole." Polymer **In Press, Corrected Proof**.

Ford, W. K., C. B. Duke, et al. (1982). "Electronic-Structure of Polypyrrole and Oligomers of Pyrrole." Journal of Chemical Physics **77**(10): 5030-5039.

Frisch, M. J., G. W. Trucks, et al. (2004). "Gaussian 03, Revision C. 02." Gaussian Inc., Wallingford, CT.

Frostick, S. P., Q. Yin, et al. (1998). "Schwann cells, neurotrophic factors, and peripheral nerve regeneration." Microsurgery **18**(7): 397-405.

Ganazzoli, F. and G. Raffaini (2005). "Computer simulation of polypeptide adsorption on model biomaterials." Physical Chemistry Chemical Physics **7**(21): 3651-3663.

Garner, B., A. Georgevich, et al. (1999). "Polypyrrole-heparin composites as stimulus-responsive substrates for endothelial cell growth." Journal of biomedical materials research **44**(2): 121-129.

Genies, E. M., M. Marchesiello, et al. (1992). "Preparation and Properties of Polypyrrole Made in the Presence of Biological Buffers." Electrochimica Acta **37**(6): 1015-1020.

George, P. M., D. A. LaVan, et al. (2006). "Electrically Controlled Drug Delivery from Biotin Doped Conductive Polypyrrole." Advanced Materials **18**(5): 577-581.

George, P. M., A. W. Lyckman, et al. (2005). "Fabrication and biocompatibility of polypyrrole implants suitable for neural prosthetics." Biomaterials **26**(17): 3511-3519.

Guimard, N. K., N. Gomez, et al. (2007). "Conducting polymers in biomedical engineering." Progress in Polymer Science **32**(8-9): 876-921.

Hallab, N. J., K. J. Bundy, et al. (2001). "Evaluation of metallic and polymeric biomaterial surface energy and surface roughness characteristics for directed cell adhesion." Tissue Engineering **7**(1): 55-71.

Hess, B., C. Kutzner, et al. (2008). "Gromacs 4: Algorithms for highly efficient, load-balanced, and scalable molecular simulation." J. Chem. Theory Comput **4**(3): 435-447.

Hiberty, P. C. and S. Shaik (2007). "A survey of recent developments in ab initio valence bond theory." Journal of Computational Chemistry **28**(1): 137-151.

Hodgson, A. J., M. John, et al. (1996). Integration of biocomponents with synthetic structures: use of conducting polymer polyelectrolyte composites. SPIE.

Huang, X., S. Zauscher, et al. (2010). "Peptide interfacial biomaterials improve endothelial cell adhesion and spreading on synthetic polyglycolic acid materials." Annals of biomedical engineering **38**(6): 1965-1976.

Hudson, T. W., S. Y. Liu, et al. (2004). "Engineering an improved acellular nerve graft via optimized chemical processing." Tissue Engineering **10**(9-10): 1346-1358.

Hudson, T. W., S. Zawko, et al. (2004). "Optimized acellular nerve graft is immunologically tolerated and supports regeneration." Tissue Engineering **10**(11-12): 1641-1651.

Jorgensen, W. L., J. Chandrasekhar, et al. (1983). "Comparison of Simple Potential Functions for Simulating Liquid Water." Journal of Chemical Physics **79**: 926-935.

Jorgensen, W. L. and J. Gao (1986). "Monte Carlo simulations of the hydration of ammonium and carboxylate ions." The Journal of Physical Chemistry **90**(10): 2174-2182.

Jorgensen, W. L., D. S. Maxwell, et al. (1996). "Development and testing of the OPLS all-atom force field on conformational energetics and properties of organic liquids." Journal of the American Chemical Society **118**(45): 11225-11236.

Jorgensen, W. L. and C. Ravimohan (1985). "Monte Carlo Simulation of Differences in Free Energies of Hydration." Journal of Chemical Physics **83**: 3050-3054.

Kaminski, G. A., R. A. Friesner, et al. (2001). "Evaluation and Reparametrization of the OPLS-AA Force Field for Proteins via Comparison with Accurate Quantum Chemical Calculations on Peptides†." J. Phys. Chem. B **105**(28): 6474-6487.

Kang, E. T., Neoh, K. G., Tan K. L. (1997). Photoelectron Spectroscopy of Conductive Polymers. New York, John Wiley & Sons.

Karabekmez, F. E., A. Duymaz, et al. (2009). "Early clinical outcomes with the use of decellularized nerve allograft for repair of sensory defects within the hand." Hand **4**(3): 245-249.

Kaynak, A. (1997). "Effect of synthesis parameters on the surface morphology of conducting polypyrrole films." Materials research bulletin **32**(3): 271-285.

Kehoe, J. W. and B. K. Kay (2005). "Filamentous Phage Display in the New Millennium." Chemical Reviews **105**(11): 4056-4072.

Khorasani, M., S. MoemenBellah, et al. (2006). "Effect of surface charge and hydrophobicity of polyurethanes and silicone rubbers on L929 cells response." Colloids and Surfaces B: Biointerfaces **51**(2): 112-119.

Kim, J.-K., E. A. Scott, et al. (2005). "Proteomic analysis of protein adsorption: Serum amyloid P adsorbs to materials and promotes leukocyte adhesion." Journal of Biomedical Materials Research Part A **75A**(1): 199-209.

Kofranek, M., T. Kovar, et al. (1992). "Ab initio studies on heterocyclic conjugated polymers: Structure and vibrational spectra of pyrrole, oligopyrroles, and polypyrrole." The Journal of chemical physics **96**(6): 4464-4473.

Kotwal, A. and C. E. Schmidt (2001). "Electrical stimulation alters protein adsorption and nerve cell interactions with electrically conducting biomaterials." Biomaterials **22**(10): 1055-1064.

Kuhn, H. H., A. D. Child, et al. (1995). "Toward real applications of conductive polymers." Synthetic Metals **71**(1-3): 2139-2142.

Lee, J. W., F. Serna, et al. (2006). "Carboxylic acid-functionalized conductive polypyrrole as a bioactive platform for cell adhesion." Biomacromolecules **7**(6): 1692-1695.

Lee, J. Y., J. W. Lee, et al. (2008). "Neuroactive conducting scaffolds: nerve growth factor conjugation on active ester-functionalized polypyrrole." Journal of The Royal Society Interface.

Lewars, E. G. (2011). Computational chemistry: introduction to the theory and applications of molecular and quantum mechanics, Springer Verlag.

Li, H. C. and E. Khor (1995). "A Collagen-Polypyrrole Hybrid - Influence of 3-Butanesulfonate Substitution." Macromolecular Chemistry and Physics **196**(6): 1801-1812.

Liu, H., A. E. Mark, et al. (1996). "Estimating the relative free energy of different molecular states with respect to a single reference state." The Journal of Physical Chemistry **100**(22): 9485-9494.

Liu, X., P. K. Chu, et al. (2004). "Surface modification of titanium, titanium alloys, and related materials for biomedical applications." Materials Science and Engineering: R: Reports **47**(3-4): 49-121.

Lowman, H. B., S. H. Bass, et al. (1991). "Selecting high-affinity binding proteins by monovalent phage display." Biochemistry **30**(45): 10832-10838.

Lykissas, M. G., A. K. Batistatou, et al. (2007). "The role of neurotrophins in axonal growth, guidance, and regeneration." Current neurovascular research **4**(2): 143-151.

Mabrouk, P. A. (2005). "Oxidative electropolymerization of pyrrole from neat monomer solution." Synthetic Metals **150**(1): 101-105.

Mackinnon, S. E. and A. L. Dellon (1988). "Surgery of the peripheral nerve." New York.

Maddison, D. and J. Unsworth (1989). "Optimization of synthesis conditions of polypyrrole from aqueous solutions." Synthetic Metals **30**(1): 47-55.

Mahoney, M. W. and W. L. Jorgensen (2000). "A Five-Site Model for Liquid Water and the Reproduction of the Density Anomaly by Rigid, Nonpolarizable Potential Functions." Journal of Chemical Physics **112**(20): 8910-8922.

McConnell, G. C., H. D. Rees, et al. (2009). "Implanted neural electrodes cause chronic, local inflammation that is correlated with local neurodegeneration." Journal of Neural Engineering **6**: 056003.

McDonald, N. A. and W. L. Jorgensen (1998). "Development of an all-atom force field for heterocycles. Properties of liquid pyrrole, furan, diazoles, and oxazoles." J. Phys. Chem. B **102**(41): 8049-8059.

Meyers, S. R., P. T. Hamilton, et al. (2007). "Endothelialization of titanium surfaces." Advan. Mater **19**: 2492-2498.

Meyers, S. R., X. Khoo, et al. (2009). "The development of peptide-based interfacial biomaterials for generating biological functionality on the surface of bioinert materials." Biomaterials **30**(3): 277-286.

Millefiori, S. and A. Alparone (1998). "Theoretical study of the structure and torsional potential of pyrrole oligomers." Journal of the Chemical Society-Faraday Transactions **94**(1): 25-32.

Miller, C., S. Jeftinija, et al. (2002). "Synergistic effects of physical and chemical guidance cues on neurite alignment and outgrowth on biodegradable polymer substrates." Tissue Engineering **8**(3): 367-378.

Ming, G., J. Henley, et al. (2001). "Electrical activity modulates growth cone guidance by diffusible factors." Neuron **29**(2): 441-452.

Mongan, J., C. Simmerling, et al. (2007). "Generalized Born model with a simple, robust molecular volume correction." Journal of Chemical Theory and Computation **3**(1): 156-169.

Onufriev, A., D. Bashford, et al. (2004). "Exploring protein native states and large-scale conformational changes with a modified generalized born model." PROTEINS-NEW YORK- **55**(2): 383-394.

Pini, A. (1994). "Axon Guidance: Growth cones say no." Current Biology **4**(2): 131-133.

Polikov, V. S., P. A. Tresco, et al. (2005). "Response of brain tissue to chronically implanted neural electrodes." Journal of Neuroscience Methods **148**(1): 1-18.

Ponder, J. W. "TINKER molecular Modeling package." Washington University Medical School. Available at http://dasher.wustl.edu/tinker.

Ponder, J. W., C. Wu, et al. (2010). "Current Status of the AMOEBA Polarizable Force Field." The Journal of Physical Chemistry B **114**(8): 2549-2564.

Prezyna, L. A., Y. J. Qiu, et al. (1991). "Interaction of Cationic Polypeptides with Electroactive Polypyrrole Poly(Styrenesulfonate) and Poly(N-Methylpyrrole) Poly(Styrenesulfonate) Films." Macromolecules **24**(19): 5283-5287.

Rabias, I., I. Hamerton, et al. (1998). "Theoretical studies of conducting polymers based on substituted polypyrroles." Computational and Theoretical Polymer Science **8**(3-4): 265-271.

Ratner, B. D. and S. J. Bryant (2004). "Biomaterials: where we have been and where we are going." Annu. Rev. Biomed. Eng. **6**: 41-75.

Ren, P. and J. W. Ponder (2002). "Consistent treatment of inter and intramolecular polarization in molecular mechanics calculations." Journal of Computational Chemistry **23**(16): 1497-1506.

Rousche, P. J. and R. A. Normann (1998). "Chronic recording capability of the Utah Intracortical Electrode Array in cat sensory cortex." Journal of Neuroscience Methods **82**(1): 1-15.

Ruhle, V., J. Kirkpatrick, et al. (2008). "Coarse-grained modelling of polypyrrole morphologies." Physica Status Solidi B-Basic Solid State Physics **245**(5): 844-848.

Ryckaert, J. P. and A. Bellemans (1978). "Molecular dynamics of liquid alkanes." Faraday Discussions of the Chemical Society **66**: 95-106.

Sadki, S., P. Schottland, et al. (2000). "The mechanisms of pyrrole electropolymerization." Chem. Soc. Rev. **29**(5): 283-293.

Sanghvi, A. B., K. P. H. Miller, et al. (2005). "Biomaterials functionalization using a novel peptide that selectively binds to a conducting polymer." Nature Materials **4**(6): 496-502.

Schmeisser, D., H. Naarmann, et al. (1993). "The two-dimensional structure of polypyrrole films." Synthetic Metals **59**(2): 211-221.

Schmidt, C. E., V. R. Shastri, et al. (1997). "Stimulation of neurite outgrowth using an electrically conducting polymer." Proceedings of the National Academy of Sciences of the United States of America **94**(17): 8948-8953.

Schmitz, U., A. Versmold, et al. (2000). "Phage Display: A Molecular Tool for the Generation of Antibodies-- A Review." Placenta **21**(Supplement 1): S106-S112.

Serra Moreno, J., S. Panero, et al. (2008). "Synthesis and characterization of new electroactive polypyrrole-chondroitin sulphate A substrates." Bioelectrochemistry **72**(1): 3-9.

Seymour, J. P. and D. R. Kipke (2007). "Neural probe design for reduced tissue encapsulation in CNS." Biomaterials **28**(25): 3594-3607.

Shin, M. C. and H. S. Kim (1996). "Electrochemical characterization of polypyrrole glucose oxidase biosensor .1. Influence of enzyme concentration on the growth and properties of the film." Biosensors & Bioelectronics **11**(1-2): 161-169.

Skotheim, T. A. and J. R. Reynolds (2007). Handbook of conducting polymers, CRC.

Stankovic, R., O. Pavlovic, et al. (1994). "The effects of preparation conditions on the properties of electrochemically synthesized thick films of polypyrrole." European polymer journal **30**(3): 385-393.

Still, W. C., A. Tempczyk, et al. (1990). "Semianalytical Treatment of Solvation for Molecular Mechanics and Dynamics." Journal of the American Chemical Society **112**(16): 6127-6129.

Suarez, M. F. and R. G. Compton (1999). "In situ atomic force microscopy study of polypyrrole synthesis and the volume changes induced by oxidation and reduction of the polymer." Journal of Electroanalytical Chemistry **462**(2): 211-221.

Sugita, Y. and Y. Okamoto (1999). "Replica-exchange molecular dynamics method for protein folding." Chemical Physics Letters **314**(1-2): 141-151.

Tozzini, V. (2005). "Coarse-grained models for proteins." Current Opinion in Structural Biology **15**(2): 144-150.

Tsujishita, H., I. Moriguchi, et al. (1993). "Potential-scaled molecular dynamics and potential annealing: effective conformational search techniques for biomolecules." Journal of physical chemistry(1952) **97**(17): 4416-4420.

Veluri, K., J. Corish, et al. (1995). "A lattice simulation investigation of the migration of chloride ions in doped polypyrrole and polythiophene." Journal of Molecular Structure: THEOCHEM **334**(2-3): 109-120.

Vernitskaya, T. V. and O. N. Efimov (1997). "Polypyrrole: a conducting polymer; its synthesis, properties and applications." Russian chemical reviews **66**: 443.

Vork, F. T. A., B. C. A. M. Schuermans, et al. (1990). "Influence of Inserted Anions on the Properties of Polypyrrole." Electrochimica Acta **35**(2): 567-575.

Wadhwa, R., C. F. Lagenaur, et al. (2006). "Electrochemically controlled release of dexamethasone from conducting polymer polypyrrole coated electrode." Journal of Controlled Release **110**(3): 531-541.

Waltman, R. J. and J. Bargon (1986). "Electrically conducting polymers: a review of the electropolymerization reaction, of the effects of chemical structure on polymer film properties, and of applications towards technology." Canadian Journal of Chemistry **64**(1): 76-95.

Wang, X., X. Gu, et al. (2004). "Evaluation of biocompatibility of polypyrrole in vitro and in vivo." Journal of Biomedical Materials Research Part A **68**(3): 411-422.

Wittmer, C. R., J. A. Phelps, et al. (2007). "Fibronectin terminated multilayer films: protein adsorption and cell attachment studies." Biomaterials **28**(5): 851-860.

Wynne, K. J. and G. B. Street (1985). "Poly (pyrrol-2-ylium tosylate), electrochemical synthesis and physical and mechanical properties." Macromolecules **18**(12): 2361-2368.

Yan, C., T. Kaoud, et al. (2011). "Understanding the Specificity of a Docking Interaction between JNK1 and the Scaffolding Protein JIP1." The Journal of Physical Chemistry B.

Yekta-Fard, M. and A. Ponter (1992). "Factors affecting the wettability of polymer surfaces." Journal of adhesion science and technology **6**(2): 253-277.

Yuan, Y., S. Adeloju, et al. (1999). "In-situ electrochemical studies on the redox properties of polypyrrole in aqueous solutions." European polymer journal **35**(10): 1761-1772.

Zhao, Y. and D. G. Truhlar (2008). "Density functionals with broad applicability in chemistry." Accounts of Chemical Research **41**(2): 157-167.

Zotti, G. (1998). "Doping-level dependence of conductivity in polypyrroles and polythiophenes." Synthetic Metals **97**(3): 267-272.